Phase transitions of borides and phosphides for use in magnetic energy conversion

Phasenumwandlungen von Boriden und Phosphiden für die Anwendung in magnetischen Energiewandlern
Zur Erlangung des akademischen Grades Doktor-Ingenieur (Dr.-Ing.)
genehmigte Dissertation von Dipl.-Ing. Maximilian Fries aus Aschaffenburg
Tag der Einreichung: 10.05.2017, Tag der Prüfung: 17.07.2017
Darmstadt 2017 — D 17

1. Gutachten: Prof. Dr. Oliver Gutfleisch
2. Gutachten: Prof. Dr. Lesley Cohen

TECHNISCHE
UNIVERSITÄT
DARMSTADT

Fachbereich Material- und Geowissenschaften
Fachgebiet Funktionale Materialien

Phase transitions of borides and phosphides for use in magnetic energy conversion
Phasenumwandlungen von Boriden und Phosphiden für die Anwendung in magnetischen Energiewandlern

Genehmigte Dissertation von Dipl.-Ing. Maximilian Fries aus Aschaffenburg

1. Gutachten: Prof. Dr. Oliver Gutfleisch
2. Gutachten: Prof. Dr. Lesley Cohen

Tag der Einreichung: 10.05.2017
Tag der Prüfung: 17.07.2017

Darmstadt 2017 — D 17

Bitte zitieren Sie dieses Dokument als:
URN: urn:nbn:de:tuda-tuprints-67865
URL: http://tuprints.ulb.tu-darmstadt.de/6786

Dieses Dokument wird bereitgestellt von tuprints,
E-Publishing-Service der TU Darmstadt
http://tuprints.ulb.tu-darmstadt.de
tuprints@ulb.tu-darmstadt.de

Die Veröffentlichung steht unter folgender Creative Commons Lizenz:
Namensnennung – Keine kommerzielle Nutzung – Keine Bearbeitung 4.0 International
http://creativecommons.org/licenses/by-nc-nd/4.0/

Erklärung zur Dissertation

Hiermit versichere ich, die vorliegende Dissertation ohne Hilfe Dritter nur mit den angegebenen Quellen und Hilfsmitteln angefertigt zu haben. Alle Stellen, die aus Quellen entnommen wurden, sind als solche kenntlich gemacht. Diese Arbeit hat in gleicher oder ähnlicher Form noch keiner Prüfungsbehörde vorgelegen.

Darmstadt, den 10.05.2017

(Maximilian Fries)

"*Du musst kämpfen, es ist noch nichts verloren!*"
Jonathan Heimes

Acknowledgments

I thank **Prof. Dr. Oliver Gutfleisch** for supervising me in my Ph.D. and giving me the opportunity to work in his group but also for introducing me to many people in the community and giving me a lot of freedom in my research. Furthermore I would like to thank him for putting a lot of trust into my work not only on a scientific level. I really enjoyed the time here in Darmstadt and it was a very exiting experience to see the group form, grow and evolve. It was a hell of a ride!

Furthermore, I want to thank **Prof. Dr. Lesley Cohen**, who kindly agreed to referee my doctoral thesis.

I am very thankful for the help of **Dr. Konstantin P. Skokov**. He introduced me to many tricks in the lab and as I would call it the ”The Russian way“. He spent many hours explaining and discussing topics on magnetism and material science with me, which made it possible for me to finish this work. Thank you!

I want to thank all members the group "**Funktionale Materialien**" for the wonderful and memory worthy time in Darmstadt. It was a great pleasure not only to work together and but also to get to know you on a personal level.

My special thanks go out to **Dr. Tino Gottschall**, **Dr. Zsolt Gercsi**, **Prof. Victorino Franco** and **Prof. Oliver Clemens** who I collaborated with during my thesis and also spent some nice time together and **Lukas Pfeuffer** my bachelor student and HIWI with whom I did a lot of research on Fe_2P alloys.

A special thanks also goes out **Dr. Semih Ener** who has often supported me during my thesis on a scientific and motivational level and to **Franziska Scheibel** who both joined me on my measurements at large scale facilities.

I would also like to thank the **DRREAM** and **DPG - SPP1599** for funding my research. Both projects allowed me to travel to different places and meet and discuss with excellent researchers.

Many thanks also go out to **Mehrdad Baghaie Yazdi** and **Prof. Lambert Alff** who gave me the first chance to work in science and without whom I would have actually never started this journey leading to this work.

I want to thank my father **Hans Fries**, **Imants Dirba**, **Dimitri Benke**, **Bahar Fayyazzi**, **Tim Helbig** and **Andreas Taubel** for prove-reading my thesis.

A very special acknowledgement goes out to **Christoph Schwöbel** my office mate, partner in crime and friend! I think without our help the team **SV Darmstadt 98** would have never made it so far.

Last but not least, I want to thank my **family** and **friends** and especially **Tine** for always supporting me whatever I do.

Abstract

Thermomagnetic energy conversion promises to be an energy efficient way of converting sources of energy needed in our modern society. For this purpose three different magnetocaloric material classes namely iron and manganese base monoborides, Co_2B and Fe_2P based materials are discussed in terms of their structural, magnetic and thermomagnetic properties and evaluated for their viability in a thermomagnetic power conversion device.

The class of transition metal monoborides based on Fe and Mn is proposed for potential use in a thermomagnetic generator based on experimental and theoretical findings. Especially the system MnB exhibits a sharp, hysteresis-free, second-order magnetic phase transition resulting in a large isothermal entropy change ΔS_t in moderate magnetic fields. The second-order nature of the phase transition in MnB and FeB was validated by temperature dependent neutron diffraction. The tunability of the transition temperature T_t was demonstrated by gradual doping of Co and Fe in the system $Mn_{1-x}Fe/Co_xB$. The high magnetization change in a small temperature interval together with the hysteresis free second-order magnetic phase transition makes MnB a very interesting candidate for thermomagnetic power conversion.

The magnetic properties of Co_2B, including spin reorientation and magnetocrystalline anisotropy, are discussed based on measurements on high quality single crystals. Additionally, the negative impact of magnetocrystalline anisotropy is studied by means of calculations of ΔS_t and measurements of the adiabatic temperature change ΔT_{ad}; then a simple phenomenological model is proposed. The structural and magnetic properties of $Co_{2-x}Mn_xB$ are studied and it was found that both magnetization M_s and Curie temperature T_C rise with doping small amounts of Mn and eventually drop with increasing the Mn content above x=0.3 allowing for tuning of T_C to room temperature. The possible non-magnetic Mn-Mn interaction with increasing Mn content leads to a lowering of M_s rendering the system $Co_{2-x}Mn_xB$ impractical for magnetocaloric energy conversion both due to a low performance and the criticality and high price of Co.

Microstructural and thermomagnetic properties of Mn-Fe-P-Si, Fe_2P-type alloys, revealed that the cubic Heusler-like secondary phase occurring in the system has a large influence on the magnetic and thermomagnetic properties as it alters the composition of the main phase significantly. The origin of the secondary phase could be traced by EBSD measurements and is ascribed to a cubic high temperature Fe_2P-phase. Furthermore, the effect of the metal to non-metal (M/NM) ratio on the sharpness of the phase transition is discussed by comparing different single-phase samples with different M/NM ratios. It could also be shown that all samples are highly porous and brittle when prepared with the powder-metallurgical method commonly proposed in literature, making them unsuitable for a direct application in a magnetocaloric heat exchanger. Additionally, by temperature dependent light microscopy the embrittlement of the sample while passing through the virgin effect could directly be observed which is related to internal stresses accumulating in the material when being cooled down through the structural magnetic phase transition for the first time after preparation. This observation is supported by measure-

ments of single particles revealing that the virgin effect vanishes if particles are as small as the single grain size. By measuring ΔT_{ad} under different field application rates it could be shown that the phase transformation in these types of alloys is field-rate dependent, contrary to the literature, resulting in a growing field-hysteresis. Furthermore, it could be demonstrated that hydrostatic pressure only has little effect on the transition temperature due the anisotropic lattice change resulting in small volume change of the material.
Overall it could be shown that the Fe_2P-type alloys are comparable in thermomagnetic performance to La-Fe-Si-based magnetocaloric alloys and can be considered as one of the most commercially viable materials.

In summary MnB was proposed as a new and promising material for thermomagnetic power conversion. Additionally, a method of improving the efficiency of thermomagnetic materials by orienting them with their magnetic easy axis parallel to the applied field was demonstrated. Furthermore, a pathway for preparing Fe_2P alloys of highest quality was established.

Zusammenfassung

Magnetische Energieumwandlung is eine potentiell sehr effiziente Methode mit einem sehr hohen Wirkungsgrad. Im Rahmen dieser Arbeit wurden drei unterschiedliche Materialklassen, Monoboride basierend auf Eisen und Mangan, Co_2B und Fe_2P basierte Materialien hinsichtlich ihrer strukturellen, magnetischen und thermomagnetischen Eigenschaften untersucht im Hinblick auf ihre potentielle Anwendbarkeit in der thermomagnetischen Energieumwandlung.

Hierbei wurden FeB und MnB basierte Verbindungen als potentielle Kandiaten für die Anwendung in einem thermomagnetischen Generator vorgeschlagen und sowohl experimentel als auch theoretisch untersucht. Das System MnB zeigt einen sehr scharfen, Hysterese freien Phasenübergangs mit einer daraus resultierenden hohen isothermen Entropieänderung ΔS_t in moderaten, anwendungsrelevanten Magnetfeldern. Ein Phasenübergang zweiter Ordnung sowohl für MnB als auch FeB konnte mittels temperaturabhängiger Neutronenbeugung bestätigt werden. Es konnte gezeigt werden, dass sich der Phasenübergang durch legieren von Fe und Co im System $Mn_{1-x}Fe/Co_xB$ sehr präzise einstellen lässt. Es zeigte sich, dass sich das System MnB hierbei aufgrund seiner hohen Änderung der Magnetisierung in einem kleinen Temperaturintervall und des hysteresefreien magnetischen Phasenübergangs besonders gut für einen Einsatz in einem thermomagnetischen Energiewandler eignet.

Die magnetischen Eigenschaften von Co_2B wurden an Einkristallen untersucht, hierbei wurden die Spin-Umorientierung und die magnetokristalline Anisotropie bestimmt. Anhand von Messungen von ΔS_t und ΔT_{ad} entlang spezifischer Kristallachsen wurde der negative Einfluss magnetokristalliner Anisotropie auf den magnetokalorischen Effekt untersucht und ein phänomenologisches Modell aufgestellt. Zusätzlich wuden die magnetischen und strukturellen Eigenschaften von $Co_{2-x}Mn_xB$ untersucht und es konnte gezeigt werden, dass die Curie Temperatur T_C und die Sättigungsmagnetisierung M_s mit kleinen Konzentrationen von Mn erst ansteigt und dann anschließend ab $x=0.4$ wieder abfällt. Durch das Einstellen der Mn Konzentration lässt sich T_C hierbei zu Raumtemperatur einstellen. Das verstärkt nicht magnetische Verhalten bei erhöhter Mn Konzentration und das daraus resultierende niedrige M_s sowie die Kritikalität von Co und der damit verbundene hohe Preis machen das System jedoch nicht praktikabel für die thermomagnetische Energieumwandlung.

Die mikrostrukturellen und magnetischen Eigenschaften von Mn-Fe-P-Si Fe_2P basierten magnetokalorischen Materialien wurden analysiert. Mittels EBSD Messungen konnte der Ursprung der kubischen Heusler ähnlichen Zweitphase auf eine kubische Fe_2P Hochtemperaturphase zurückgeführt werden. Es konnte gezeigt werden, dass das Auftreten der Zweitphase einen sehr großen Einfluss auf die magnetokalorischen Eigenschaften der Hauptphase hat, da dadurch die Zusammensetzung dieser signifikant verändert wird. Anhand von einphasigen Proben wurde die Wichtigkeit des Metall zu Nichtmetall Verhältnisses M/NM für einen scharfen Phasenübergang erklärt. Eine erste direkte Beobachtun des “virgin Effects” der sich im Zerbersten der Probe äußert, konnte mittels temperaturabhängiger Lichtmikroskopie gemacht werden. Der Ursprung wurde auf interne Spannungen beim ersten Abkühlen zurückgeführt und

konnten auch mittels Messungen an kleinen Partikeln bestätigt werden. Hierbei wurde in Partikeln im Größenbereich der Korngröße das Auftreten dieses Effektes nicht beobachtet. Es konnte gezeigt werden das hydrostatischer Druck nur wenig Einfluss auf den Phasenübergang aufgrund der anisotropen Änderung der Gitterparameter und der daraus resultierenden kleinen Volumenänderung hat. Des Weiteren wurde mittels Messungen von ΔT_{ad} in verschiedenen magnetischen Feldraten gezeigt, dass sich eine Feldhysterese in Abhängigkeit der Feldrate ausbildet und der Phasenübergang erster Ordnung in Fe_2P Materialien feldratenabhängig ist, anders als in der Literatur angenommen wird.
Fe_2P basierte Materialien zeigen vergleichbare thermomagnetische Eigenschaften wie La-Fe-Si-basierte Materialien und eignen sich hierbei besonders für industrielle Anwendungen.

Zusammenfassend, wurde MnB als eine neues Material zur Verwendung in einem thermomagnetischen Energiewandler vorgeschlagen. Ein Weg zur Verbesserung der Effizienz thermomagnetischer Materialien wurde aufgezeigt, in dem Materialien entlang ihrer leichten magnetischen Achse parallel zum angelegten Magnetfeld magnetisiert werden. Desweiteren wurden Wege aufgeigt wie Fe_2P basierte Legierungen mit exzellenten thermomagnetischen Eigenschaften erreicht werden können.

Contents

List of Figures

Nomenclature

α	Seebeck coefficient
χ	Magnetic susceptibility
ΔH	Change of the magnetic field
ΔM	Magnetization change
ΔS_t	Isothermal entropy change
ΔS_{rot}	Rotational isothermal entropy change
ΔT_{ad}	Adiabatic temperature change
η_{abs}	Absolute thermodynamic efficiency
$\eta_{anisotropy}$	Anisotropy factor
η_{Carnot}	Carnot efficiency
η_{rel}	Relative thermodynamic efficiency
κ	Thermal conductivity
λ	Wavelength of incident beam in diffraction experiments
Φ	Magnetic flux
ρ	Electrical resistivity
σ_{tot}	Total scattering cross section
θ	Diffraction angle
ϑ_P	Paramagnetic Curie temperature
a, b, c	Lattice constants
C	Curie constant
C_p	Heat capacity at constant pressure

d_1, d_2	Shortest Mn-Mn distances in a crystal lattice
d_{hkl}	Interplanar lattice spacing
E_a	Anisotropy energy
E_f	Fermi energy
G	Gibbs free energy
H	Magnetic field
H_a	Anisotropy field
H_E	Enthalpy
I	Stoner exchange integral
L	Total path length of scattering experiment
M	Magnetization
M_s	Spontaneous magnetization
P	Pressure
Q_{in}	Heat flow needed to drive transition
S	Total entropy
S_{ele}	Total entropy of the electronic system
S_{lat}	Total entropy of the lattice
S_{mag}	Total entropy of the magnetic system
T	Temperature
T_C	Curie temperature
T_t	Transition temperature
T_{cold}	Temperature on cold end of a process
T_{hot}	Temperature on hot end of a process
T_{start}	Starting temperature of a process
U	Internal energy

V	Volume
W_{out}	Magnetic work output
ZT	Thermoelectric figure of merit
BSE	Backscatter electron mode
CFC	Chlorofluorocarbon
DFT	Density functional theory
DoS	Density of states
DSC	Differential scanning calorimetry
EDX	Energy dispersive electron spectroscopy
FC	Field cooling
FH	Field heating
FM	Ferromagnetic
GDP	Gross domestic product
GWP	Global warming potential
HRPD	High resolution powder diffractometer
IMF	International monetary found
M/NM	Metal to non-metal ratio
MCE	Magnetocaloric effect
NM	Non-magnetic
PDoS	Partial density of states
PM	Paramagnetic
SEM	Scanning electron microscopy
TMG	Thermomagnetic generator
XRD	X-ray diffraction

1 Introduction and motivation

Cooling is one of the basic needs for human civilization since the very beginning. Especially keeping goods cool and/or controlling the environmental temperature is a general need in our modern society. Not only food conservation or air conditioning which are by far the most important applications but also preserving medication is a basic building block of our modern society. In the early days human society relied on natural possibilities to keep cool, like storing ice from the winter (shown in Figure 1.1a)) or storing goods far below the ground. Since the invention of gas compression refrigeration in 1834 [1] this technology has far evolved and helped society strive. Early compression based refrigerators were large machines which were operated by steam engines with open drive compressors using dangerous and highly poisonous refrigerants. The sheer size of these devices as shown in Figure 1.1b) did not allow the use in private households but they were used to produce ice blocks for cooling at home mostly in wooden based refrigeration cabinets.

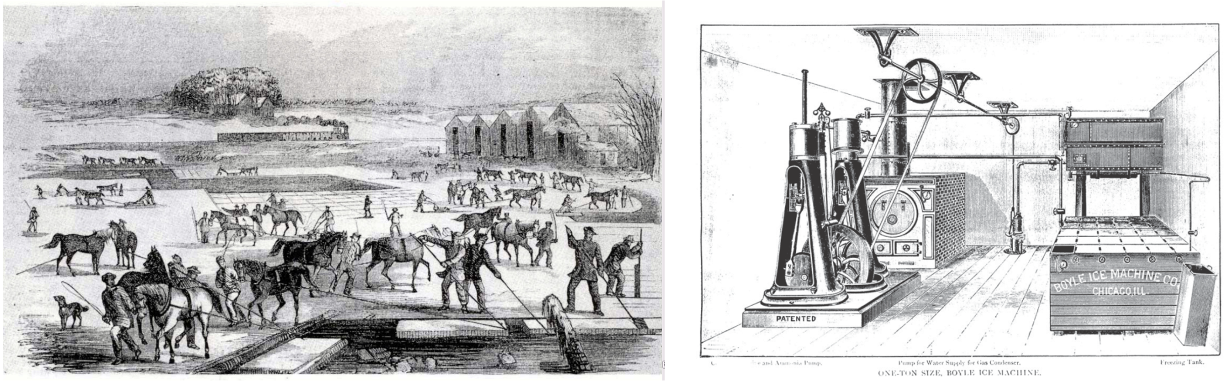

(a) (b)

Figure 1.1: a) Ice harvesting at Spy Pond, Arlington, Massachusetts, 1852, showing the railroad line in the background, used to transport the ice [2]. b) A can ice machine by Boyle Ice Machine Co., 1879. Image taken from [3]

Since the 1930s household-refrigerators based on chloroflourocarbons CFCs are available and have spread to nearly every home in the developed world. In large scale cooling devices it is still current practice to use ozone layer depleting chlorofluorocarbons, whereas small-scale conventional compressor based cooling technologies nowadays rely on non-ozone depleting, yet highly explosive hydrofluorocarbons which show an about thousand times higher global warming potential (GWP) than for example CO_2 [4, 5, 6, 7] as shown in Table 1.1.

Table 1.1: Common CFC free cooling media, their temperature range of usage and their GWP[8].

refrigerant	temperature range of usage	GWP
R134a	300 - 250 K	1430
R404a	270 - 230 K	3922
R410a	270 - 230 K	2088

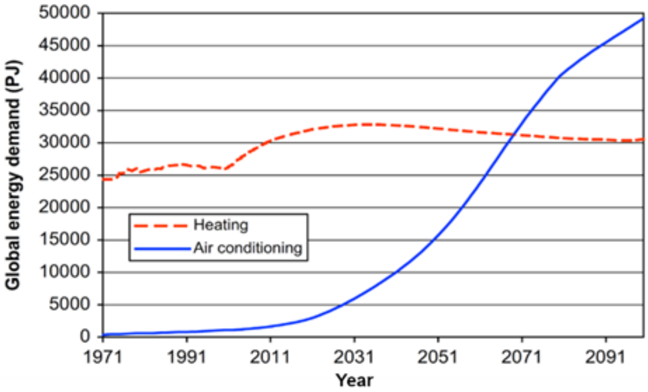

Figure 1.2: Prediction of the energy demand for cooling and heating, adopted from [9].

Keeping ourselves and our goods cool is not merely necessary for human society but also a sign of wealth for civilization. A nearly exponential increase in demand of cooling power is predicted for the next 50 years especially for air conditioning [9] as shown in Figure 1.2. This is also based on the fact that a large growth of the gross domestic product (GDP) is expected over the next century. The GDP is a monetary measure of all products produced within a country in a certain period and is used to determine the economic performance and wealth of a specific country. In Figure 1.3 the expected growth of the GDP in the year 2021 from the international monetary found (IMF) is shown. A large growth in wealth is expected especially in regions south of and close to the equator [10], where temperatures are usually higher than in other parts of the world and therefore the demand for cooling is rising. Furthermore, taking into account global warming it sounds rather strange that we still use a cooling concept based on a technology which promotes global warming. Additionally, most of the electricity produced worldwide is based on fossil fuels. In order to reduce their usage the focus should lie on an overall concept concerning the energy chain, from power generation to consumption. Even a small improvement in efficiency will have a large impact on the global energy landscape.

A solid state based technology like magnetocaloric energy conversion could help us to overcome these issues. The technology is based on the magnetocaloric effect (MCE), a physical phenomena occurring in magnetic materials under the influence of a varying magnetic field. The MCE can be exploited for magnetic refrigeration, magnetic power generation or magnetic heat pumping [11].

Magnetocaloric materials have a global warming potential and ozone layer depleting potential equal to zero, not taking mining and refining of the constituent elements into account. Magnetocaloric energy conversion offers a potential gain in efficiency due to its isentropic magnetization processes compared

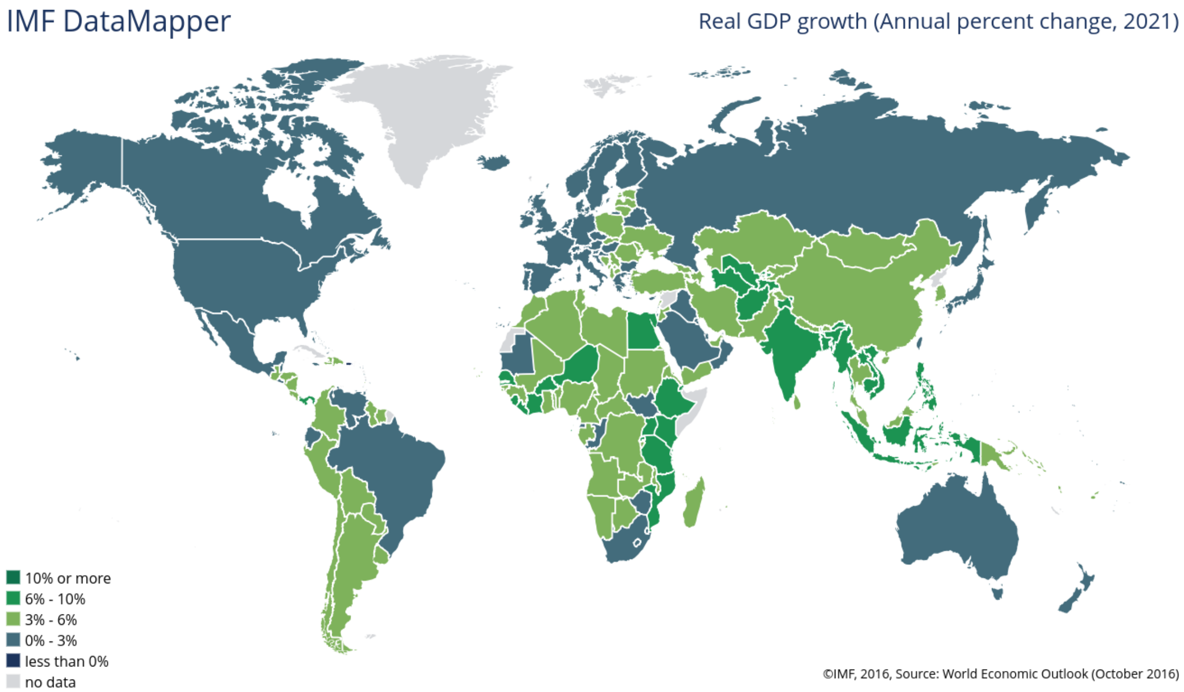

Figure 1.3: GDP growth forecast for the year 2021 with data taken from [10]

to gas-vapor refrigeration [12]. Besides numerous prototypes constructed in the past 30 and more years, commercial success of this technology is still in far future. The task of building an efficient energy conversion device based on the magnetocaloric effect needs to be a combined effort of material scientists and engineers. The thesis presents only a small contribution to this growing field and focuses mainly on finding new materials for magnetic energy conversion and/or the fundamental understanding and improvement of known materials.

This work is structured as follows:

The fundamental background about the magnetocaloric, effect followed by the basic working principles of magnetic cooling and energy conversion and the term magnetic anisotropy will be explained briefly in the second chapter. This will be followed by a short summary of the production and characterization methods used in this work.

In chapter 4 cubic monoborides based on iron and manganese are proposed as potential candidates for magnetic power conversion followed by a detailed characterization of their magnetic phase transitions.

In chapter 5 the magnetic properties of the system Co_2B doped with manganese will be discussed. The effect of magnetocrystalline anisotropy on the MCE will be explained by studying a single crystal of Co_2B.

In chapter 6 Mn-Fe-P-Si based Fe_2P-type alloys and effect of microstructure on the MCE will be discussed, followed by an analysis of the dynamic properties of field rate dependent magnetic phase transition.

In the last chapter the main findings of the work are summarized and a short outlook will be presented.

2 Fundamentals

2.1 Phase transitions

Thermodynamically a phase transition or phase transformation is the transition or conversion of one ore more phases of any substance from one thermodynamic state or phase to another. A graphical representation of the stability range of the phase as a function of the state variables such as pressure P, temperature T, chemical composition and/or magnetic field H are provided by phase diagrams. In these phase diagrams, the stability ranges are limited by phase boundaries at which the transitions occur. A phase transition can occur between solid, liquid and gaseous phases and can generally be classified by the Ehrenfest-classification named after Paul Ehrenfest, an Austrian physicist. For the classification thermodynamic variables such as volume V, entropy S or enthalpy are considered as a function of one or more variables, mostly the temperature [13, 14].

A thermodynamic system is described by the Gibbs Energy G or often referred to as free energy of a system. For a n^{th}-order phase transition, G is continuous as a function of T or p, including its first $n-1$ derivatives and the n^{th} derivative is discontinuous. A more detailed analysis of phase transitions is given by Landau, where the phases are characterized by symmetry breaks from ordered to disordered phases and accompanied by jumps of macroscopic quantities, such as the magnetization or deformation of a crystal lattice, considered as the order parameters of a system.

Of particular importance and interest for this work is the distinction in phase transitions of first and higher order (continuous phase transitions), especially second-order phase transitions. The most prominent example of a first-order phase transition is the transition of a liquid, like water, to a solid state known as the freezing point. In order to transfer from the solid to the liquid state, additional energy in form of latent heat has to be supplied without an actual temperature increase of the thermodynamic system. In the case of melting of ice a discontinuity in the entropy versus temperature curve can be observed. The entropy is given by the first derivative of the free energy G by the temperature. Likewise, the volume of the phase exhibits a jump at the phase transition leading to a density difference, which can be ascribed to a order parameter in Landau's theory of phase transition where a jump in the order parameter is characteristic for a first-order phase transition.

An important example of a second-order phase transition for this work is the transition of a magnetic material from the ferromagnetic to paramagnetic state at a specific temperature known as the Curie temperature T_C. The magnetization M in this case is considered as the order parameter, which steadily approaches zero at T_C, without additional latent heat occurring. However, a jump in the heat capacity C_p versus temperature can be observed. The heat capacity is given by the second derivative of G after T.

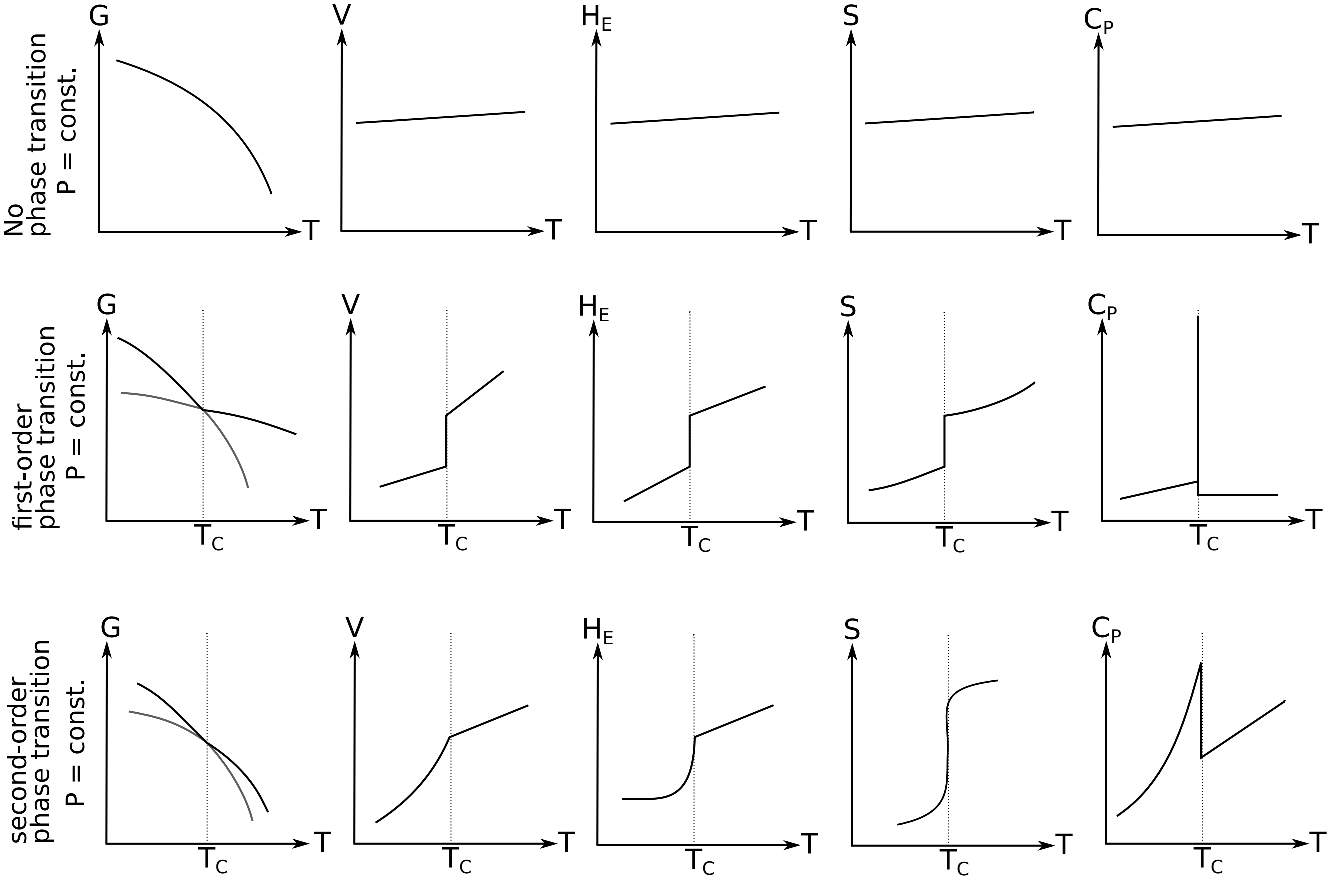

Figure 2.1: Classification of phase transitions after Ehrenfest depicting the differences of first- and second-order phase transition according to the temperature dependent behavior of the thermodynamic variables: free energy *G*, volume *V*, enthalpy H_E, entropy *S* and heat capacity C_p

This behavior is characteristic for a continuous or second-order phase transition. Here the transition of the order parameter after Landau is considered to be continuous.

In Figure 2.1 the classification of phase transitions after Ehrenfest is depicted. Schematics of first- and second-order phase transitions as well as no phase transitions are shown in terms of the free energy G, the volume V, the enthalpy H_E, the entropy S and the heat capacity C_p as a function of temperature T under constant pressure P. In the first row the temperature dependence of the thermodynamic variables are shown for no phase transition occurring, followed by a phase transition of first- and second-order. The phase transformation takes place at the transition temperature T_t which can be attributed to the Curie temperature T_C for a second-order phase transition as this work is dealing with magnetic materials.

2.2 The magnetocaloric effect

The magnetocaloric effect (MCE) manifests itself as a change of thermodynamic state of a magnetic material in an external alternating magnetic field H. Depending on the conditions (isothermal or adiabatic) under which the magnetic field H is applied, either the isothermal entropy change ΔS_t or the adiabatic temperature change ΔT_{ad} are commonly used as numerical parameters characterizing the magnitude of the magnetocaloric effect.

This effect was first theoretically postulated in the works of Langevin in 1905. He predicted that the temperature of a paramagnetic material should change as a function of magnetic field [15]. The later called magnetocaloric effect was first observed in experiment by Weiss and Picard in the year 1917 where they could measure a temperature change on Ni among application of a magnetic field [16]. For a detailed historic overview of the discovery of the MCE the reader is referred to an article by Smith [17]. In 1949 Giaque was honored with the Nobel price in chemistry for his contributions on the state of matter at low temperatures. He exploited the MCE on paramagnetic salts in order to reach sub-Kelvin temperatures [18]. In the 1970s it was realized that the magnetocaloric effect could be enhanced by using magnetic materials close to their transition temperature which resulted in a magnetocaloric cooling prototype operating at room temperature [19]. The demonstrator was operated by a superconducting magnet with a field strength of 7 T and Gd plates reaching a maximal temperature span of 49 K. The material hereby was used in a single stage regenerator of only Gd. A few years later the active magnetic regenerator (AMR) was introduced which is nowadays commonly used in prototypes in order to reach large temperature spans [12].

2.2.1 Working principle of a magnetocaloric refrigerator

The principle cooling cycle of a magnetocaloric fridge is illustrated in Figure 2.2. The magnetocaloric cycle is performed analogous to the refrigeration cycle by Carnot. In contrast to the conventional compressor-based Carnot cycle not the pressure but the magnetic field is increased and decreased. At the starting point in Figure 2.2(a) the magnetic material is in its paramagnetic state. In (b) the magnetocaloric material is placed in a thermally insulated (adiabatic) environment and the magnetic field is applied. The increasing field H causes the magnetic moments/spins of the magnetic material to align parallel to H decreasing the magnetic entropy S_{mag}. Due to the adiabatic conditions the total energy of the system stays constant and the material is heated by a temperature ΔT_{ad} with the net temperature of the material now being $T_{start} + \Delta T_{ad}$ due to an increase in the lattice entropy S_{lat}. In the next step shown in Figure 2.2c) the added heat Q is then extracted by fluid or gas heat exchange media. The magnetic field hereby is held constant. Once the material has cooled down to the temperature T_{start} it is brought back to adiabatic conditions and the magnetic field H is removed (see Figure 2.2d)). As the total entropy of the system is again constant and the spin entropy of the system increases and the lattice entropy decreases, the material has to expel energy in the form of heat, whereas the material is cooled to a temperature of $T_{start} - \Delta T_{ad}$. The material is then put in contact with a thermal transfer fluid which is in contact with the environment to be refrigerated. In an iterative process a cooling cycle can then be realized and can be used in a magnetic cooler for example a refrigerator or air conditioner.

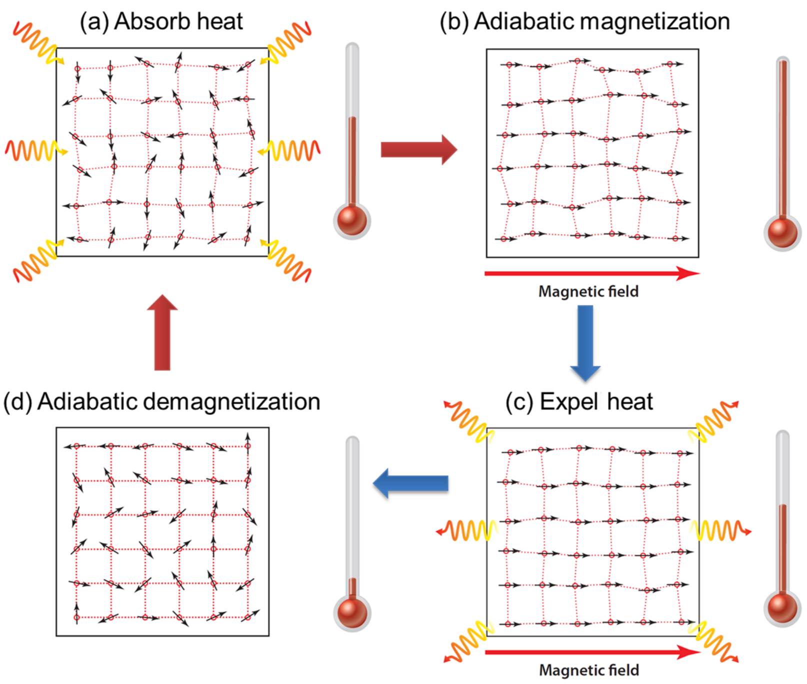

Figure 2.2: Schematic of the working principle of a magnetic refrigerator adapted from [20].

2.2.2 Physical background

In the following section the fundamental background for understanding the magnetocaloric effect for the materials shown in this thesis will be presented. Only materials exhibiting conventional magnetocaloric effects of first- and second-order will be discussed. In Figure 2.3a) the magnetization curves for a material exhibiting a second-order phase transition are shown for both in zero and applied field. The most well-known material exhibiting a second-order magnetic phase transition is Fe; the most prominent in the field of magnetic refrigeration is the prototypical material Gd which will be discussed shortly in a later section of this work. From Figure 2.3a) it can be seen that at $H = 0$ the material undergoes a continuous magnetic phase transition from its low temperature ferromagnetic state to its high temperature paramagnetic state.

The susceptibility of the material follows the Curie-Weiss law [21, 22]:

$$\chi = \frac{M}{H} = \frac{C}{T - T_C} \tag{2.1}$$

with χ being the susceptibility of a paramagnet defined as the ratio of magnetization M and magnetic field H. C is defined as the Curie constant and T_C as the Curie-temperature. The magnetization reaches zero when approaching T_C. The determination of T_C is not trivial, as shown when a magnetic field is applied, as the magnetic transition smears out due to the partial alignment of spins in the paramagnetic state. A measurement of magnetic properties in zero field is not possible due to formation of magnetic

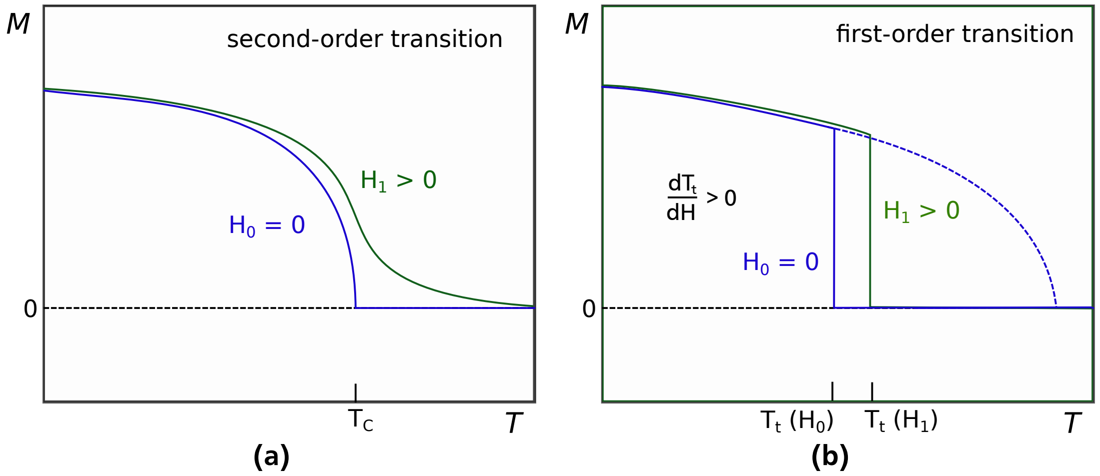

Figure 2.3: Magnetization versus temperature curves for materials exhibiting second-order magnetic transition in a) and a first-order magnetostructural/magnetoelastic phase transition in b). The difference for zero and applied field are shown for both cases.

domains [22], therefore the determination of T_C in this work was performed by Arrot-Belov plots [23, 24] and fitted to Kuz'min's equation [25].

The magnetization versus temperature curves for a first-order phase transformation are shown in Figure 2.3b). A discontinuity can be observed in M (the order parameter). This behavior is common for materials belonging to the La-Fe-Si- and Fe_2P-families. It occurs because a structural transformation takes place from a low temperature ferromagnetic to a high temperature paramagnetic phase. This can be either a real structural transformation where the crystal symmetry changes (for example in Heusler alloys) or an iso-structural transition where the crystal symmetry remains unchanged, but a jump in lattice parameters is present (for example Fe_2P alloys) [20]. The transition occurs at the transition temperature T_t in contrary to a second-order transition where the transition takes place at T_C. This is an important factor as the ferromagnetic phase also shows a T_C, which is indicated by the dotted line in Figure 2.3b), yet it is interrupted by the structural transition. In the case of field application the transition shifts to higher temperatures in conventional first-order materials, as the ferromagnetic phase is stabilized by the magnetic field and can be understood as the driving force of the magnetocaloric effect in first-order transition materials. A transition from a paramagnetic to a ferromagnetic state can be induced by a magnetic field.

The understanding of the temperature dependent total entropy is indispensable for magnetic cooling as it is the basic driving force of the effect. In Figure 2.4a) the total entropy for both zero and applied field case is shown for a second-order phase transition.

The total entropy is a combination of three terms, all of them are functions of temperature and applied field:

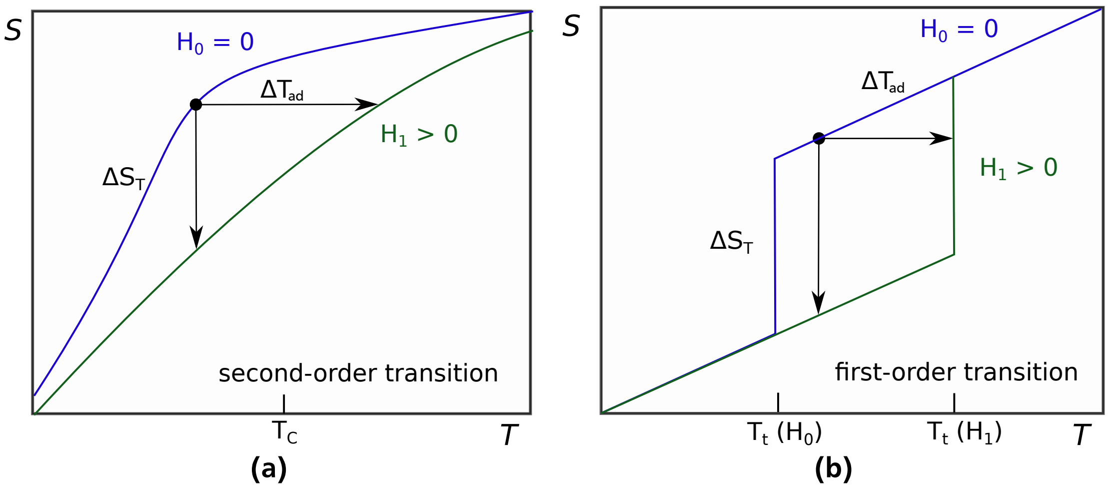

Figure 2.4: Total entropy versus temperature curves for materials exhibiting second-order magnetic transition in a) and a first-order magnetostructural/magnetoelastic phase transition in b). The differences for zero and applied field are shown for both cases.

$$S(T,H) = S_{lat}(T,H) + S_{mag}(T,H) + S_{ele}(T,H), \tag{2.2}$$

with the lattice contribution S_{lat}, S_{mag} the contribution of magnetic moments and S_{ele} the electronic contribution to the total entropy. The electronic contribution can be considered negligible in most materials [26].

The total entropy can be determined by measurements of the heat capacity C_p in a calorimeter as:

$$S(T) = \int_0^T \frac{C_p}{T} dT. \tag{2.3}$$

In case of an applied magnetic field, the magnetic moments align and the entropy of the magnetic system decreases, lowering the total entropy of this system according to 2.2. If the magnetic field is applied under adiabatic conditions the temperature of the system will rise by the temperature ΔT_{ad} as indicated by the horizontal arrow in Figure 2.4a). In case of isothermal field application the entropy of the system will be lowered by ΔS_t indicated by the vertical arrow.

In Figure 2.4b) the entropy change for materials with a first-order transition are shown. The entropy curves show a discontinuity, like the magnetization curves shown in Figure 2.3b) and the $S(T)$ diagram has the shape of a parallelogram because of the shift in transition temperatures. Like in second-order materials the entropy decreases under isothermal conditions and the sample heats in adiabatic conditions under field application.

Both, the adiabatic temperature change ΔT_{ad} and the isothermal entropy change ΔS_t are figures of merit for magnetic refrigeration and need to be maximized for an application. Both thermodynamical figures of merit can be quantified directly by calorimetry or direct measurements of the temperature change.

The calculation of both can be derived, based on the free energy G of a magnetic material:

$$G = -SdT - PdV - MdH \tag{2.4}$$

where S is the total entropy, P the pressure and V the volume. Equation 2.4 concludes that M and S are given by:

$$M = -\left(\frac{\partial G}{\partial H}\right)_{V,T}, \tag{2.5}$$

$$S = -\left(\frac{\partial G}{\partial T}\right)_{V,H}. \tag{2.6}$$

Under the assumption of constant V the Maxwell relation can be directly derived from 2.4:

$$\left(\frac{\partial S}{\partial H}\right)_T = \left(\frac{\partial M}{\partial T}\right)_H. \tag{2.7}$$

By integration of Equation 2.7 the entropy change ΔS can be directly calculated from magnetization measurements:

$$\Delta S_t(T, \Delta H) = \int_{H_0}^{H} \left(\frac{\partial M(T,H)}{\partial T}\right)_H dH. \tag{2.8}$$

In case of adiabatic conditions the adiabatic temperature change can be calculated from 2.8 and 2.3:

$$\Delta T_{ad}(T,\Delta H) = \int_{H_0}^{H} \frac{T}{C_p} \left(\frac{\partial M(T,H)}{\partial T} \right)_H dH. \tag{2.9}$$

Equations 2.8 and 2.9 only prove to be valid under the following assumptions:

- The sample is in thermodynamic equilibrium
- The derivative of M with respect to T is existent

The first condition directly results from the basic laws of thermodynamics and the derivation of the free Energy in Equation 2.4 which is only valid in the case of the initial and final state being in thermal equilibrium. In order for the second assumption to be valid, the magnetization should not show a discontinuity with respect to the temperature.

Both conditions are fulfilled in the case of second-order materials, whereas the second condition is not fulfilled for materials with first-order transitions as depicted in Figure 2.3b). Therefore, special care needs to be taken when analyzing first-order phase transitions based on the Maxwell equations [27, 28]. The details of the ΔS_t determination used in this work will be outlined in the experimental section of this work.

The temperature dependence of the entropy change ΔS_t in different applied fields is shown in Figure 2.5 for materials with first- and second-order transitions. From Figure 2.5a) one can see that the isothermal entropy change ΔS_t is negative and always has a maximum at the Curie temperature T_C and grows with increasing field. The transition is usually quite broad, allowing for a wide temperature use of this class of materials. $\Delta S_t(H)$ scales not linear, but in a more complex way described by Lyubina $et\ al.$ [29]. The temperature dependence of ΔS_t can also be properly described by scaling laws as shown by Franco $et\ al.$ [30].

In the case of a first-order transition, shown in Figure 2.5b) ΔS_t is also negative but the field dependent behavior is distinctly different. In low fields, the entropy change has a narrow peak which grows broader with increasing field. When the field is high enough to completely drive the ferromagnetic to paramagnetic transition, a plateau in ΔS_t can be be observed. With higher fields the entropy change just grows broader, as the transition is shifted to a higher temperature by the magnetic field. The left flank of the curve always stays constant at the transition temperature T_t as the material below T_t is always in the ferromagnetic phase where no transition can be induced. Both types of curves, or a combination of both will be discussed within the framework of this thesis, depending on the studied materials.

The occurrence of thermal hysteresis will be discussed in more detail in the following. In Figure 2.6a) the temperature dependent magnetization is shown for both heating and cooling in fields of $H=0$ and $H>0$. In both cases thermal hysteresis can be observed, meaning that the heating and cooling branch of

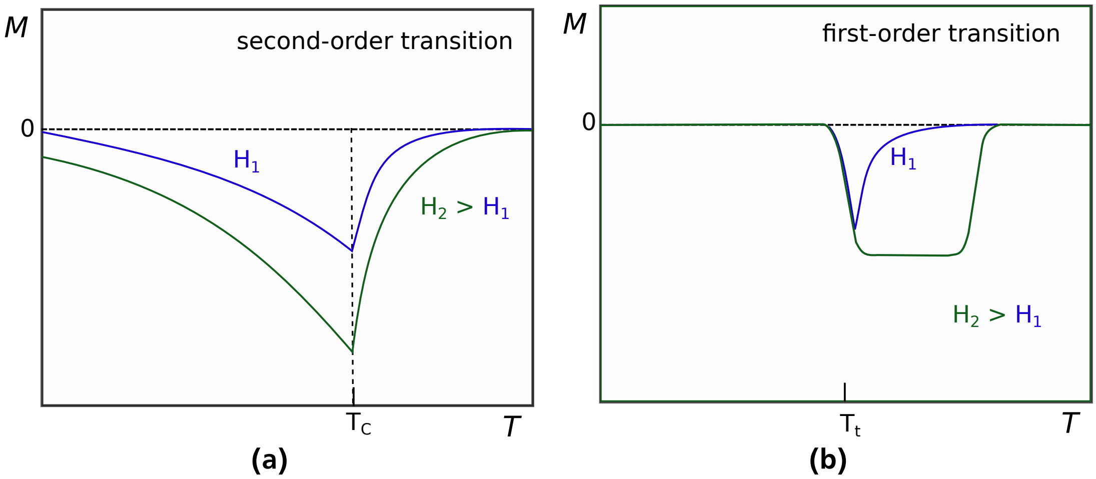

Figure 2.5: Entropy change versus temperature curves for materials exhibiting second-order magnetic transition in a) and a first-order magnetostructural/magnetoelastic phase transition in b). The differences for field changes of different magnitude are shown for both cases.

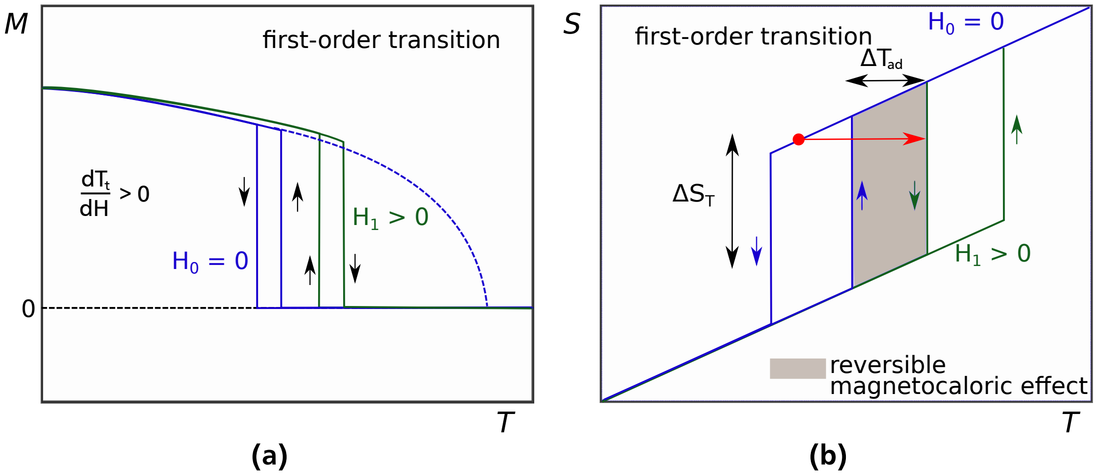

Figure 2.6: Influence of thermal hysteresis in first-order transitions schematically shown for the magnetization M in a) and b) the total entropy S, both in zero and applied magnetic field H.

magnetization do not overlap. In this case the transition of the cooling branch is at a considerably lower temperature than that of the heating branch. This behavior is typical for the Fe_2P-material class presented in this work, but also for other prominent magnetocaloric families like La-Fe-Si and $Gd_5Si_xGe_{4-x}$ [20, 31].

The effect of thermal hysteresis is inherent for materials with a first-order phase transition because of the occurrence of latent heat needed to drive the transition and has direct consequences on the application of magnetocaloric materials. This can be seen when looking at Figure 2.6b) where the total entropy curves are shown both for zero and an applied magnetic field. The entropy curves do not coincide due to thermal hysteresis and only a small part of the total entropy change (the hatched area) can be utilized for cooling. Thermal hysteresis directly leads to a lowered magnetocaloric performance when the material is cycled if compared to Figures 2.4a) and b). Therefore, one has to distinguish between the cyclic and the static magnetocaloric figures of merit in materials showing a first-order phase transition. The difference is highlighted by the double sided arrows in Figure 2.6b) showing the reversible part of the entropy change ΔS_t and ΔT_{ad}. Both the cyclic and static figures of merit for MCE can be assessed by utilizing different measurement protocols which will be discussed later in this work. In the results section of this work, it will be always mentioned if one is considering either the cyclic or the reversible values when discussing first-order phase transitions.

2.2.3 Magnetocaloric materials

Numerous magnetocaloric materials have been studied so far, ranging from single elements, to complex intermetallics and constantly new classes of materials are assessed in terms of their magnetocaloric properties. This section does not aim to give a complete picture of all the interesting materials and research but should give a short overview of the most studied and most evolved materials for magnetic cooling. For further details of the materials discussed within this work the reader is referred to the specific chapters (4,5 and 6) of the thesis where a short outline of the known properties and literature will be given.

The pure element Gd represents the gold-standard of magnetocalorics. Gd exhibits a second-order phase transition close to room temperature at 291 K with a ΔT_{ad} of 2.5 KT^{-1} with no hysteresis involved [32]. Gd is also the first material to be used in a room temperature magnetic cooling engine as mentioned before, and is still the most widely used material in prototypes or demonstrators today, due to its well defined characteristics being a single element and due to its excellent secondary engineering properties. For obvious reasons the transition temperature in a single element is not tunable, but it was shown that the addition of Y can effectively lower the T_C [33]. This allows for the possibility of utilizing Gd based compounds in stacked heat exchanger structures, giving an opportunity of achieving a wider temperature span than in the pure metal [34].

The discovery of the "giant" magnetocaloric effect in $\mathrm{Gd_5Si_xGe_{4-x}}$ by Pecharsky and Gschneidner [35] triggered substantial research efforts in the material science and physics community which are still growing [36]. In this compound a strong coupling between the magnetic and crystal lattice is observable and the material undergoes a first-order phase transition in a certain interval of x and T_t is precisely tunable. Yet, the fact that the intermetallic alloy contains costly and critical elements like Gd and Ge hinders a possible large-scale industrial implementation [37, 38]. Furthermore, the material tends to decrepitate due to the large volume change at the transition [39].

An industrially more favorable compound is the La-Fe-Si-family of alloys. Especially the fully hydrogenated compound $\mathrm{La(Fe,Si,Mn)_{13}H_x}$ is of special interest as it exhibits a tunable first-order transition around room temperature [40, 41, 42]. This compound is derived from the $\mathrm{LaFe_{11.8}Si_{1.2}}$ base compound. $\mathrm{LaFe_{11.8}Si_{1.2}}$ exhibits a first-order transition at around 200 K, which is too low for room temperature applications [43, 44, 45]. The Curie temperature can be increased by substituting Co on the Fe sites, shifting the transition to and above room temperature but with loss of magnetocaloric properties due to a shift from a first- to a second-order phase transition. Hydrogenating the base compound fully leads to a transition temperature above room temperature [46] and partial hydrogenation [47, 48] leads to unwanted aging effects in the material [49, 50]. The solution to these problems is the substitution of Mn on the Fe sites, lowering the transition of the base compound and then fully hydrogenating the sample leading to a tunable transition around room temperature. The material $La(Fe,Si,Mn)_{13}H_x$ has been commercialized by the company Vacuumschmelze under the brand name Calorivac-H [51]. Yet, the application of this material in a regenerator structure is not trivial, as the hydrogenation process is accompanied by a dercrepitation of the material into powders. A process of polymer binding the powdered material was studied in order to provide bulk-like heat exchanger plates [52].

An upcoming class of materials for magnetic refrigeration is the class of Heusler compounds. Especially, Ni-Mn-In based Heusler structures have attracted research interest [53, 54]. Heusler alloys, undergo a inverse magneto-structural phase transition, meaning a transformation from a low magnetization low temperature martensite phase, to a high temperature austenite phase. Large magnetocaloric effects can be achieved in Heusler alloys, however always accompanied by large thermal hysteresis hindering a possible application of the material at the moment. Static adiabatic temperature changes of −8 K [55] could be achieved with values of entropy change of up to 20 $\mathrm{Jkg^{-1}K^{-1}}$ in a field change of 2 T [26]. A possible way of applying this class of materials was recently described by Gottschall $et\ al.$ when using only minor loops of magnetization overcoming the problem of thermal hysteresis and showing sizable cyclic values of ΔT_{ad} 3 K in a field of 1.9 T [55].

Another industrially important class of materials is the class of Fe_2P-alloys crystallizing in the hexagonal $P\bar{6}2M$ crystal structure. Since the discovery of the giant magnetocaloric effect in $MnFeP_{0.4}As_{0.55}$ in 2002 [56], various studies have shown that the system is highly tunable in its magnetic and magnetocaloric properties by varying the Mn and Fe content and substitution of As, Ge, Si and P on the As side [57]. Most compounds have a structural phase transition together with a low change in total volume due to the anisotropic expansion of lattice parameters in the iso-structural first-order phase transition [58]. Recently, it was shown that the structure can also be stabilized with interstitial elements like B making the system structurally more durable for application purposes [59]. A more detailed description of the Fe_2P system will be given in chapter 6.

The development of new materials and the optimization of known materials is crucial for the success of magnetic refrigeration. However, not only the primary material parameters like ΔT_{ad}, ΔS_t should be taken into account but the materials transition temperatures, their hysteretic properties, thermal and electrical conductivities need to be precisely controllable in order to efficiently utilize them in a magnetocaloric cooling engine. Additionally, also the secondary engineering properties are of great importance when taking the step from material science to engineering. Materials need to be easily machinable, structurally integer and resistant to corrosion in order to implement them in a heat exchanger structure. Lastly, but very important, the materials used in a mass product need to be environmentally friendly, non-critical in terms of constituent elements and cheap. In order to make magnetocaloric cooling commercially viable and not only a nice playground for scientists, new materials with both excellent primary magnetocaloric properties like ΔS_t and ΔT_{ad} but also excellent secondary properties like mentioned above need to be discovered. Additionally, known materials need to be fully understood in order to exploit them efficiently. This is and will be not an easy task and requires the combined effort of the scientific and engineering community.

2.3 Thermomagnetic energy harvesting

2.3.1 Energy harvesting from industrial waste heat

Industrial waste heat refers to energy generated in an industrial process without being put to any practical use. Sources of waste heat include for example hot combustion gases which are discharged to the atmosphere, heated products exiting industrial processes or cooling media in order to remove heat from a product or process. It is estimated that as much as 20 to 50 % of industrial energy consumption is ultimately discharged as waste heat [60]. Oddly, the exact amount is poorly quantified when considering for example that the United States of America industrial sector accounts for almost one third of the energy used in the US. This results in approximately 1×10^{13} kWh per year and an emission of 1680 million metric tons of CO_2 into the atmosphere [61].

A valuable approach to improve the overall efficiency of an industrial process is to reuse, capture or convert the lost or waste heat intrinsic to all industrial processes. It is stated that in some cases the efficiency for example of an industrial furnace can be increased by 10 to 50 % [62]. Captured and reused or converted waste heat is an emission-free alternative green energy source. So far, many technologies are available for transferring waste heat to a productive end use, but almost none are applied, other than reusing the heat directly for another process.

Three essential components are necessary in order to recover waste heat [60]:

1. An accessible source of waste heat
2. Usage for the recovered energy
3. An efficient recovery technology.

In this work, the focus will lie on recovery technologies in order to efficiently convert waste heat directly into electricity. In order to be applied, waste heat recovery needs to be efficient and even more important it needs to be cheap and easy to implement for companies, despite the significant environmental benefits and energy savings.

The most prominent and most studied way to convert heat directly to electricity is by thermoelectric power conversion. The basis of this effect is that a pair of different metals exposed to different temperatures generates a voltage which was later called the Seebeck effect after the discoverer Thomas Seebeck. The Seebeck coefficient α is the degree to which extent a material can separate charge due to an applied thermal gradient. The figure of merit in thermoelectrics is the parameter ZT and the relative efficiency in terms of Carnot efficiency is given as [63]:

$$ZT = \frac{\alpha^2 T}{\kappa \rho} \tag{2.10}$$

$$\eta_{rel} = \frac{T_{hot} - T_{cold}}{T_{hot}} \cdot \frac{\sqrt{ZT+1} - 1}{\sqrt{ZT+1} + \frac{T_{cold}}{T_{hot}}}, \tag{2.11}$$

where ρ, κ and T are the electrical resistivity, thermal conductivity and mean temperature. Therefore ZT has a direct influence on the relative efficiency of a thermoelectric device. Generally, metals have a large thermal conductivity and a small Seebeck coefficient and thus a $ZT << 1$. The discovery of new semiconductor materials *e.g.* bismuth-telluride (BiTe) with a low thermal conductivity raised the ZT to about one [64]. Although this meant a significant improvement, a figure of merit $ZT = 4$ resulting in relative efficiency of about 40% is necessary in order to compete with other energy harvesting approaches [65]. Recent research in the development of super-lattice thermoelectric materials predict an improved efficiency of about $ZT \approx 4$, yet measurements show much lower values [65, 66]

The performance of a thermoelectric generator is currently limited by the availability of materials showing a large ZT and state-of-the-art devices perform at a relative efficiency of ≈ 10%, while operating at a temperature difference of 50 K [65]. In order to be more efficient with the current materials available, large temperature gradients are required and the technology is unsuitable in applications with small thermal gradients.

Waste energy can be graded into three categories [60]:

1. High (T > 950 K)
2. Medium (T = 500 - 950 K)
3. Low (T < 500 K).

Whereas, the use of high and medium grade waste heat is common by reusing the heat directly for preheating, steam generation or for conversion by the organic Rankine cycle, low grade waste heat is mostly discarded to the environment [67, 68].

Low grade waste heat for example are exhaust gases, process steam condensate, cooling water or hot processed liquids and solids and sums up to about 50% of all waste heat disregarded in industrial processes and so vastly available [68]. The main point hindering the use of this source of energy is the lack of efficient and cheap conversion technologies as mentioned before.

A recent study by Vuarnoz *et al.* shows that the efficiency of a thermomagnetic generator can exceed the efficiency of conventional technologies, namely organic Rankine cycle (ORC), Stirling power generators and thermoelectric power generators, especially in the low exergy regime [69] using low to medium grade waste heat where the above mentioned technologies cannot even operate. Whereas, exergy is defined as the usable available energy in a thermodynamic process. Additionally, magnetic power conversion works favorable with a temperature difference independent of the height of the temperature levels of heat sink and source.

Yet, it has to be noted that the overall thermodynamic efficiency of a device is limited by the Carnot efficiency which cannot be very high due to the low thermal spans achieved in low to medium grade heat in regard to the environment.

2.3.2 The thermomagnetic generator

A thermomagnetic regenerator (TMG) is a device which extracts electrical energy from a system that can convert thermal energy into magnetic energy. The idea behind a TMG involves a thermally oscillating switch inside a magnetic circuit. The switch hereby is a magnetic material that undergoes a magnetic phase transition, *i.e.* ferromagnetic to paramagnetic at its transition temperature and induces an electric flux into a wound coil around the magnetic material due to a change in magnetic field. Accordingly, a magnetocaloric material can also be used to directly convert heat to electricity [70, 58].

Nikola Tesla postulated the first type of thermomagnetic generator with his patent of a "Thermo Magnetic Motor" in 1889 [71] shown in Figure 2.7, also known as a Curie Wheel which was readopted by the company Swiss Blue Energy in 2012 [72].

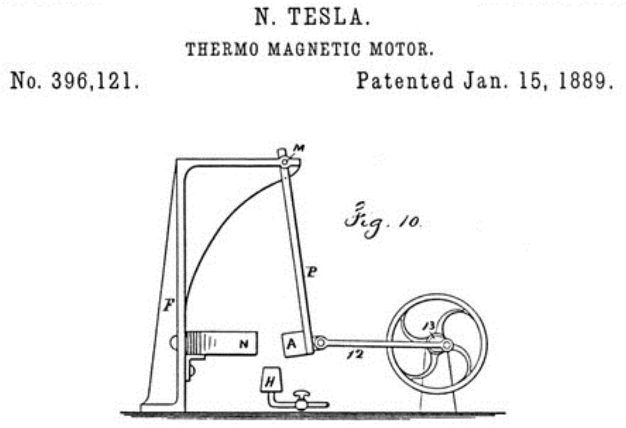

Figure 2.7: Thermomagnetic energy conversion engine as thought of by Tesla in 1889 [71].

Brillouin and Iskenkenderian firstly estimated the efficiency of a direct thermomagnetic generator to be as high as 55.5% of the Carnot efficiency [73] At this time, the element Gd was not thought of as a suitable material for this application but classical ferromagnets like Fe and Co with high Curie temperatures. The improvement of extraction and manufacturing techniques of rare-earth metals opened the opportunity for further investigations into thermomagnetic generation and Elliot was the first to investigate the role of the material properties on the efficiency of a thermomagnetic generator based on Gd. The analysis was based on Brillouin's ideas and used Gd as an active material and Alnico XII as a permanent magnet material estimating a Carnot efficiency of also 55.5% [74].

Improvements in efficiency were proposed by utilizing materials having high values of dM/dT which are arranged in series with decreasing Curie temperatures. Here, also regenerative cycle concept was proposed which reuses the rejected heat from one thermomagnetic generator cycle in order to reduce the amount of heat input for the next cycle and increase total efficiency, similar as proposed for magnetocaloric cooling. By numerical analysis an efficiency of 75% was predicted relative to a Carnot engine [75].

In 1991 Solomon designed a regenerative TMG device. The device was based on the concept of oscillating the thermomagnetic material (Gd) both thermally and magnetically in very large magnetic fields produced by a superconducting solenoid. Neglecting the energy use of the superconductor both for cooling and electricity usage a relative efficiency of 44% could be achieved [76].

Recently, based on first-order Fe_2P-type (Mn-Fe-P-As based) magnetocaloric materials, a proof of concept device was developed in order to experimentally demonstrate such a direct thermomagnetic energy conversion engine [77]. The device operated with a magnetic field of 0.24 T and a frequency of 0.1 Hz with a temperature difference between the hot and cold sink of 16 K and is based on the original idea of Tesla. The overall efficiency of the device was very low which was attributed to the fact that the material used in the experiments degraded during shaping of the regenerator.

In addition, a simple phenomenological model was developed that allows to predict material thermodynamic efficiencies of transformations based on magnetic and heat capacity measurements [78].

The absolute efficiency of a thermomagnetic material η_{abs} can be defined as:

$$\eta_{abs} = \frac{|W_{out}|}{Q_{in}}, \tag{2.12}$$

with W_{out} being the magnetic energy work output by the material and Q_{in} the heat needed in order to drive the material through the phase transition.

A schematic how to calculate W_{out} from measurement of magnetization versus field at different temperatures $M(H)_T$ and Q_{in} from measurements of heat capacity as a function of temperature $c_p(T)$ can be found in Figure 2.8.

The relative efficiency can be calculated by:

$$\eta_{abs} = \frac{\int_{H_0}^{H_1} M(T,H)dM}{\int_{T_{cold}}^{T_{hot}} c_p(T)dT}. \tag{2.13}$$

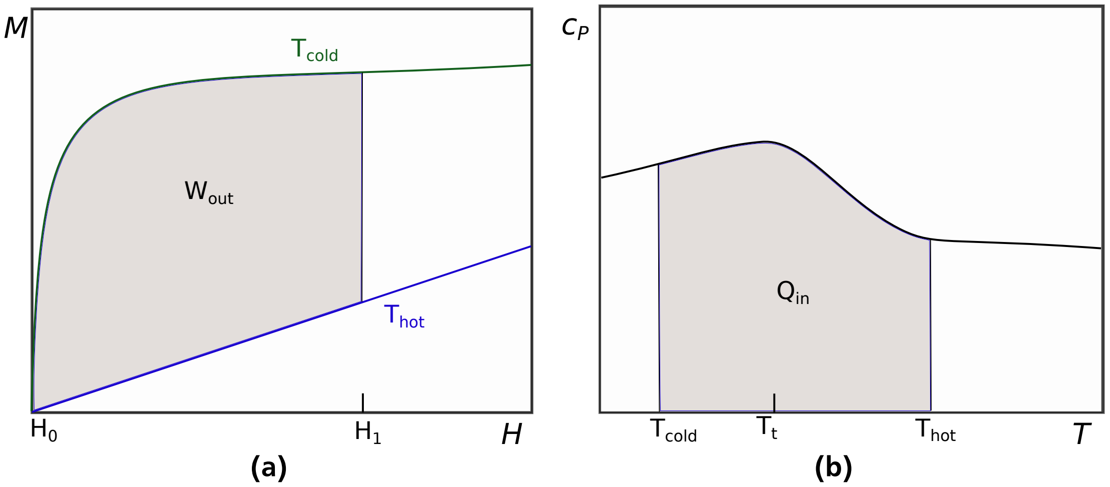

Figure 2.8: a) Calculation of W_{out} from $M(H)_T$ measurements. b) Calculation of Q_{in} from measurements of $c_p(T)$.

The relative Carnot efficiency of a material can be written as:

$$\eta_{rel} = \frac{\eta_{abs}}{\eta_{Carnot}} = \frac{\eta_{abs}}{1 - \frac{T_{cold}}{T_{hot}}} = \frac{\eta_{abs}}{\frac{\Delta T}{T_{hot}}}. \tag{2.14}$$

This type of analysis can only be regarded as a first estimate and has to be treated with care, as it neglects several aspects. The magnetic work output for example is only an estimate as it does not consider how the magnetic energy can be converted to electrical energy and all aspects of geometry of the sample and field generation are neglected. Additionally, the heat capacity of a material is field dependent and the transfer of heat to the sample and furthermore its heat exchange is neglected. Above all the comparison of different materials in terms of their relative Carnot efficiency η_{rel} is not suitable as the transition temperature of a materials governs this value due to the large impact of T_{hot} and not the actual magnetic properties of the sample.

2.3.3 Thermomagnetic energy conversion materials

The magnetocaloric and thermomagnetic generator research fields have in common that the change of magnetization with temperature needs to be maximized. With large dM/dT, large magnetic entropy change is expected when considering the Maxwell relation (for second-order transitions) [79].

Maximizing the derivative will also induce large voltages in a coil wound around the magnet according to Faraday's law thus generating thermomagnetic energy. Although, the magnetic entropy change is always present, magnetocaloric applications necessitate the transition to be also dependent on an external magnetic field, which is not a requirement for thermomagnetic energy conversion.

Table 2.1: List of elements and compositions studied for use in TMG taken from [78]

composition	T_C in K	η_{rel} in %
Ho	20	57
Er	20	29
Dy	89	23
Tb	220	12.5
Gd	293	20.5
Ni	531	2.5
Fe	1044	9.5
Co	1390	1

The use of first-order phase change materials may be detrimental to the efficiency of a thermomagnetic generator because the latent heat needed to drive a first-order phase transition will be absorbed by the material during the transformation, lowering the efficiency when compared to Equation 2.13. This in contradiction to searching for materials with a high entropy change as these mostly involve first-order phase transitions. Additionally, hysteresis effects which are usually observed in first-order type phase transitions will also lower the overall efficiency as overheating and undercooling of a material is necessary. One should therefore search for materials which are close to a tricritical point, combining both the good properties of first-order phase transitions (high change in magnetization in a small temperature interval) with the properties of second-order phase transitions (no thermal hysteresis) [80, 81].

However, heat exchangers made of cascaded stacks can increase the usable temperature range of the thermomagnetic generator and increasing device efficiency [69, 77] like in a magnetic refrigerator. In order to prepare cascaded material stacks with specific transition temperatures, the material has to allow for precise compositional tuning and has to be easily machinable. Additionally, proper heat exchange between the materials and with the exchange fluid is also necessary to ensure an efficient operation at optimal frequencies [82, 83, 31].

At the moment mostly pure ferromagnetic elements are considered to be used in a TMG. A list of elements studied so far using the above mentioned method are given in Table 2.1 together with their Curie temperature T_C, relative efficiencies η_{rel} and an operating temperature range ΔT of 5 K.

It should be mentioned that the values for single crystals were added to the table above, as they exhibit higher efficiencies than polycristalline samples, due to their lower losses during magnetization. It was also postulated that rather than using a conventional magnetic phase transition one could use for example the spin reorientation of a material in order to increase efficiency.

The applicability of first-order type Heusler alloys with sharp magnetic and structural phase transitions was recently shown both theoretically and experimentally [70, 84].

Summarizing, in order to make above mentioned technologies commercially viable, the high dM/dT must occur in compounds made of earth abundant elements with T_C in the range of 200-800 K. In order to harvest the low exergy waste heat development of new materials and/or improvement of the existing ones is necessary.

2.4 Magnetic anisotropy

The term magnetic anisotropy describes the directional dependence of a material's magnetic properties. In anisotropic materials the magnetization vector, the magnetic moment will always try to align along the thermodynamically favored ”easy axis” of spontaneous magnetization [21]. This is in contrast to a magnetically isotropic material which has no preferential direction where the magnetic moments align. This alignment of magnetization vectors can only be induced by applying a magnetic field, forcing the magnetic moments to rotate towards the direction of applied magnetic field in order to minimize their overall energy. One can easily see from this, that magnetic anisotropy is an important prerequisite for the application of permanent magnets and magnetic hysteresis in ferromagnets. Yet, magnetic anisotropy is not only important in the field of permanent magnets, but can influence magnetic properties in all different applications of magnetic materials and can often not be neglected [22]. There are various sources of magnetic anisotropy such as:

- Magnetocrystalline anisotropy: Induction of preferential orientation by the electronic structure of a crystal,
- Shape anisotropy: Occurring in imperfect spherical particles, like for example magnetic nanowires,
- Magnetoelastic anisotropy: Introduction of anisotropy through tensioning or compression of the material.

For the discussion of this work the magnetocrystalline anisotropy is of most importance and will be discussed in more detail. Magnetocrystalline anisotropy is the tendency of magnetization to align itself along a preferred crystallographic axes. The magnetocrystalline anisotropy energy E_a is defined as the energy difference per unit volume between a sample magnetized along the easy and the hard axis. In most materials the final value of saturation magnetization M_s is the same for every axis the magnetic field is applied along, provided the field is large enough. In anisotropic magnetic materials the field dependence along which M_s is reached can be different depending on the crystallographic axes. The field needed to reach M_s is called anisotropy field H_a.

Magnetocrystalline anisotropy energy is the energy required to rotate the spin system of a magnetic domain away from the easy direction of magnetization to the hard direction of magnetization. The energy needed to rotate the spin system is the energy needed to overcome the spin-orbit coupling of the system. When applying a magnetic field the direction of the electron spin follows and the orbitals need to be reoriented, because of the coupling of the spin and the orbital moments [85].

In most magnetic materials spin-orbit coupling is rather weak and E_a is small. However, as mentioned above large magnetocrystalline anisotropy is a prerequisite in order to make permanent magnets. Usually large spin-orbit coupling is found in heavy rare-earth elements. Once such a material is magnetized a large energy is needed in order to reverse the magnetization to overcome anisotropy. For this reason, rare-earth alloys are often used in permanent magnet applications where a large coercive field is needed. The intrinsic magnetocrystalline anisotropy is only one prerequisite which has to be transferred to an extrinsic coercivity by microstructural engineering [22].

One may ask why this is of importance for magnetic refrigeration and thermomagnetic energy conversion as these technologies require soft magnetic materials in order to be magnetized and demagnetized without any hysteretic losses. This fact holds true for transformer materials like Fe-Si alloys, but some magnetocaloric materials are not of cubic symmetry like for example the hexagonal Fe_2P system. For this reason can exhibit magnetocrystalline anisotropy resulting in losses for the overall energy conversion device.

3 Experimental methods

3.1 Sample preparation

3.1.1 Melting techniques

For melting the samples with specific compositions two different techniques were applied: Induction melting and arc-melting.

In induction melting a high frequency electric source is used to drive a large alternating current through a coil wherein a high rapidly alternating magnetic field is generated within the coil. The material to be molten is then placed inside the coil and a current flow is induced into the conducting material which is known as eddy current. This effect is strongest in ferromagnetic materials but works for all conducting materials. In this work a Reitel Induret induction melter was used. The device was modified and equipped with a vacuum pump allowing for atmospheres below 1×10^{-3} mbar. Conducting materials were put in an Al_2O_3 crucible that is placed within the coil. In order to melt non-conducting materials or powders the Al_2O_3 crucible was set into a graphite crucible prior to placing the material into the melter allowing for indirect heating of the material. Prior to melting the device is pumped three times with a vacuum pump for 5 minutes with consecutive flushing steps with argon. Prior to melting an Ar atmosphere of 1.6 - 1.8 mbar was established in the melter. Melting was performed until the sample has fully melted which was controlled by visual inspection.

Arc-melting was performed in a Buehler MAM-1 arc melter. In order to melt a material an electrode is positioned close to the material and several kilo amperes of DC voltage are applied between the tip of the electrode and the grounded base plate. The same pumping and flushing steps as in induction melting were applied for arc-melting. Melting was performed until a homogeneous bubble of molten metal was formed. The cooling rate of the material is much higher than in the induction furnace as the molten sample is in direct contact with a water cooled copper base plate.

3.1.2 Powder metallurgical processing

Powder metallurgical processing is divided into three main steps: Powder fabrication, shaping and sintering often followed by a post treatment step like grinding shaping etc. Powder metallurgy is of special interest when producing materials that are either hardly soluble or have high melting temperatures. Furthermore, materials of constituents with large differences in melting temperatures can be formed by this process. Within the framework of this thesis, high energy ball milling was used for powder fabrication, cold-uniaxial pressing was applied for shaping and solid phase sintering was used for phase formation of the Fe_2P alloy.

For fabrication of the Fe_2P-alloys elemental powders were mixed together under argon atmosphere in the wanted ratios. In order to achieve a mixture of very fine grained powders, 5 g of powder were filled into hardened steel milling vials together with two milling balls and sealed under argon atmosphere. Milling was performed on a SPEX 8000D mixer mill at 875 cycles/min. After milling powders were removed from the milling vial under argon atmosphere and 1 g of powder was filled into a press form and precompacted by hand. To avoid oxidation, the press form was wrapped into a plastic paraffin film and put into two sealable plastic bags and afterwards pressed uniaxially at room temperature with a hydraulic press.

Before sintering, the green body was wrapped into molybdenum foil to avoid oxidation during sintering. The wrapped body was then inserted into a Al_2O_3 crucible and placed into a vacuum furnace. Prior to every sintering step the furnace was flushed 3 times with argon and pumped for half an hour. Pumping of the chamber was performed constantly at a temperature of 473 K prior to high temperature application in order to remove residual water vapor. Before heating to sintering temperature the furnace was filled with argon gas to a pressure of 1.4 mbar. In order to compensate for the expansion of the gas a pressure release valve was added to the system. After sintering the sample surfaces were grinded by sandpaper to remove a possible oxidation layer on the samples.

3.1.3 Single crystal growth

Single crystals were grown by melting a pre-alloy using high frequency induction melting of 40 - 50 g starting material. The pre-alloy is then crushed into pieces and filled into a Al_2O_3 crucible and capped with molybdenum foil. The samples are placed into a vacuum furnace and a pumping and flushing step as described above was applied. Samples were heated above their melting temperature T_m and then slowly cooled to about 2/3 of T_m with a cooling rate of $0.5\,\mathrm{Kmin}^{-1}$ and then annealed at this temperature for 2 weeks, allowing the formation of a very coarse grained microstructure.

Large grains of the ingot were removed by crushing and cutting steps. The quality of the single crystals and their orientation was verified by Laue XRD on a goniometer head. Single crystals were then cut into a cubic shape using an erosion wire saw along the main crystallographic axes.

3.2 Characterization methods

3.2.1 X-ray diffraction

X-ray Diffraction (XRD) is a powerful and non destructive tool to investigate a material's crystal structure with an information depth of up to a few μm. Additional information can be obtained about the texture (the distribution of preferred orientations), mean crystallite size and the residual stress in the studied specimen.

When X-rays interact with an atom, they can either be absorbed or scattered which gives rise to the emission of a coherent electromagnetic wave of the same frequency in all directions of space. On a periodic array of atoms, such as in a crystal, the waves emitted by a single atom can interfere with waves emitted by other atoms. This gives rise to destructive or constructive interference of the waves resulting in a diffraction pattern characteristic of the crystallographic arrangement of the material. The crystallographic directions along which interference are of constructive nature, are defined by the Laue conditions [86].

The Bragg conditions can be derived from the Laue equations and describe a simple geometric relation for the nature of the constructive interference on the crystallographic planes, described by the Miller Indices (hkl). The Bragg law relates the angle 2θ to the inter planar spacing d_{hkl} in the following way:

$$2d_{hkl}\sin\theta = n\lambda \tag{3.1}$$

with λ being the wave length of the incident beam.

In a tetragonal crystal system the lattice parameters are: $a = b \neq c$ with the angles being $\alpha = \beta = \gamma = 90°$. The lattice parameter can be related to the inter planar distance d_{hkl} by using the following equation:

$$\frac{1}{d_{hkl}^2} = \frac{h^2 + k^2}{a^2} + \frac{l^2}{c^2} \tag{3.2}$$

In a orthorombic crystal system the lattice parameters are: $a \neq b \neq c$ with the angles being $\alpha = \beta = \gamma = 90°$. The lattice parameter can be related to the inter planar distance d_{hkl} by using the following equation:

$$\frac{1}{d_{hkl}^2} = \frac{h^2}{a^2} + \frac{k^2}{b^2} + \frac{l^2}{c^2}. \tag{3.3}$$

However, in a hexagonal crystal system the lattice parameters are also $a = b \neq c$ but with the angles of $\alpha = \beta = 90°$ and $\gamma = 120°$. The lattice parameters can be related to the inter planar distance d_{hkl} by the following equation:

$$\frac{1}{d_{hkl}^2} = \frac{4}{3}\frac{h^2 + hk + k^2}{a^2} + \frac{l^2}{c^2} \tag{3.4}$$

.

One of the most common measurements performed on polycrystalline samples, in order to investigate the crystal structure, is the θ-2θ scan. The θ-2θ scan was used to conduct the measurements presented in this thesis. Measurements were performed in transmission geometry on finely hand grinded metallic powder with Mo Kα_1 x-ray radiation with a Ge (111) monochromator mounted on the beam side.

All XRD measurements shown in this work were performed on a Stoe Stadi P instrument in transmission mode with Molybdenum $K\alpha_1$ radiation at room temperature.

XRD data was refined with a Rietfeld refinement routine implemented in Fullprof [87] by comparing the data to the JCPDS-ICDD (Joint Committee on Powder Diffraction Standards / International Center for Diffraction Data) database.

3.2.2 Electron Backscatter Diffraction

Electron backscatter diffraction (EBSD) is a microstructural characterization technique. It is is used to study crystalline materials in order to determine their structure, crystal orientations and phases within a scanning electron microscope. For the measurements performed in this work, polished crystalline samples are placed in a Tescan Vega 3 SEM at a highly tilted angle towards the diffraction camera in order to increase the contrast of the resultant electron diffraction pattern. When the electron beam hits the sample, electrons will enter the sample and some will backscatter towards the detector. In case the Bragg conditions are fulfilled the electrons diffract and form Kikuchi bands which correspond to each of the lattice diffracting crystallographic planes. If the crystal geometry is well described it is possible to relate the recorded Kikuchi bands to the underlying crystal phase and the orientation of the material grain within the electron interaction volume which then can be indexed by Miller indices [88]. The EDAX EBSD software used, detects the measured pattern bands via mathematical routine using a modified Hough transformations [89]. The EBSD technique was used to spatially describe the crystal orientation of the material and was used to examine the texture and sample morphology of Fe_2P based samples.

3.2.3 Neutron diffraction

Neutron diffraction is a widely used technology in modern material science that allows for high precision determination of magnetic and crystal structures. Because neutrons are charge neutral particles the non-magnetic scattering in a diffraction experiment is not based upon interaction with the electron cloud of a material but with the nucleus. This gives rise to certain advantages compared to XRD. The nuclear interaction of the neutron gives a position of an atom in a crystal lattice which is independent of the

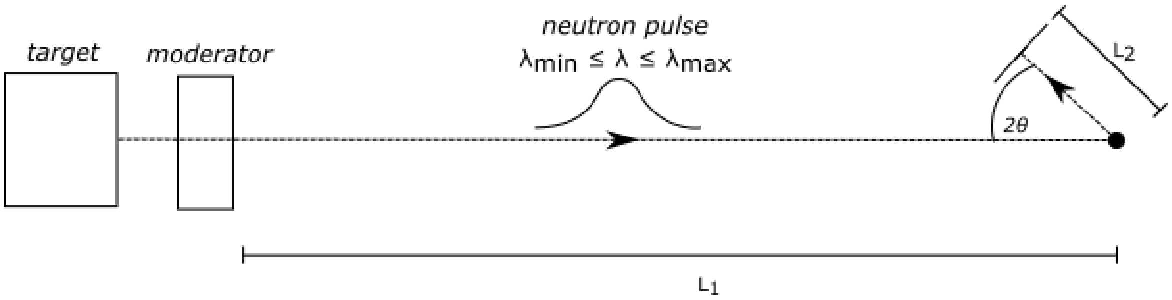

Figure 3.1: Schematic of the time-of-flight measurements technique. The total path length $L = L_1 + L_2$
.

shape or deformation of the electron cloud. The fact that neutrons are spin 1/2 particles also allows for probing of the magnetic properties of a crystal structure [90].

A fundamental quantity measured in scattering experiments is the differential scattering cross section $\frac{d\sigma}{d\Omega}$ which is the total number of neutrons scattered into the solid angle Ω per second in the direction of the measurement. The total scattering cross section σ_{tot} is the integral of the differential cross section over all angles [91].

$$\sigma_{tot} = \int \frac{d\sigma}{d\Omega} d\Omega \tag{3.5}$$

The strength of scattering of neutrons is strongly dependent on the element, the isotope of the element and the energy of the neutron. Absorption of neutrons can also occur depending on the element or isotope. Specifically the natural isotopes of B, Cd and Gd absorb neutrons strongly leading to a very limited applicability of neutron scattering for materials containing these elements [91, 90]. In order to account for this fact the isotope B^{11} was used in order to perform the neutron scattering experiments on MnB and FeB in this work.

Neutron scattering measurements shown in this work are based on the time-off-flight measurement technique. Here, the neutrons are detected as a function of time, rather than as a function of angle as previously explained for XRD. This technique is mostly used at spallation sources that produce a pulsed beam composed of a range of wavelength. The basic experimental setup is shown in Figure 3.1.

Here, a neutron pulse with a distribution of wavelengths travels from the neutron source (the target) to the sample and scatters at an angle 2θ. The time of flight t is the total time the neutron travels over the distance L. The fundamental scattering equation can be obtained by combining Braggs condition (Equation 3.1) with the de Broglie relation $\lambda = \frac{h}{p}$. If the momentum p is expressed as the product of mass m and velocity v and the time of flight of the neutron t over the distance L as $t = \frac{L}{v}$ one obtains the scattering equation relating the d_{hkl}-spacing to t:

$$t = \frac{L}{v} = \frac{L}{p/m} = \frac{mL\lambda}{h} = \frac{2m}{nh} L d_{hkl} \sin\theta \tag{3.6}$$

The resolution function of a time-of-flight instrument is:

$$\frac{\Delta d_{hkl}}{d_{hkl}} = \left[\left(\frac{\Delta L}{L} \right)^2 + \left(\frac{\Delta t}{t} \right)^2 + (\Delta\theta \cos\theta)^2 \right]^{1/2} \tag{3.7}$$

with ΔL being the uncertainty in the distance between the moderator and detector, Δt is the uncertainty in the time-of-flight and $\Delta\theta$ is the uncertainty in the scattering angle [92].

All measurements were performed at the ISIS neutron source at the Rutherford Appleton Laboratory in Didcot, Oxfordshire where measurement time was applied for in order to perform these specific measurements. Approximately 4 μs long pulses of neutrons are produced from a 800 MeV synchotron hitting a tantalum-clad tungsten target. The resultant wavelength at peak flux is approximately 1.8 Å. In order to perform the experiments the HRDP (High Resolution Powder Diffractometer) was used, a instrument designed specially for high-resolution structural studies of crystalline powders. The path length of the moderator to the detector L is approximately 100 m greatly increasing the resolution compared to shorter beamlines (see Equation 3.7). It is claimed to be the highest resolution machine of its type worldwide [93]. HRPD is equipped with three pairs of detector banks: a low-angle back centered bank at 30°, a centered bank at 90° and at 168° a backscattering bank. The backscattering bank has the highest resolution and is commonly used alone for the structure determination. The low-angle bank allows access to larger d-spacings which are used for the determination of magnetic structures.

3.2.4 Magnetic measurements

Magnetic measurements were performed in two different setups. A PPMS-14T (physical property measurement system) from Quantum Design and a LakeShore 7400 series vibrating sample magnetometer. Both measurements rely on the principle of the vibrating sample magnetometer (VSM).

The VSM is based on Faraday's induction law:

$$U_{ind} = -\frac{d\Phi}{dt}, \tag{3.8}$$

whit the voltage U_{ind} being induced by the time-dependent variation of a magnetic flux Φ.

In a VSM magnetometer a homogeneous magnetic field H is produced by electromagnets. H is used to magnetize the sample which is centered within the middle of the field source. The sample is fixed to a sample rod that vibrates with a given frequency and amplitude. The vertical movement of the sample induces an AC voltage U_{ind} in the pick up coils of the magnetometer. As H is kept constant, it has no effect on U_{ind}. The induced voltage is only proportional to the magnetic moment of the sample if the frequency and amplitude of the sample rod is kept constant. The induced voltage is also dependent on the sample geometry and the properties of the pick-up coils. The magnetometer is calibrated prior to measurements with a Ni-sample of known geometry.

For the characterization of polycrystalline materials needle like samples in the range of 3 - 50 mg were extracted from the bulk samples and mounted onto the sample sticks. For low temperature measurements Kapton tape and for high temperature measurements ZrO_2 cement was used for fixing the samples on the sample rod. Samples were mounted with the needle being aligned along the magnetic field direction in order to minimize demagnetization effects.

For the determination of the isothermal entropy change $M(H)_T$ or $M(T)_H$ were used. For $M(T)_H$ measurements a step size of $\Delta H = 0.2\,\mathrm{T}$ was chosen with a temperature sweep rate of $2\,\mathrm{Kmin}^{-1}$. The $M(T)_H$ measurement procedure was chosen for the entropy change determination of first-order materials. Therefore, the samples were overheated and undercooled to at least 30 K above and below the transition temperature to avoid minor-loop effects. The isothermal entropy change was then obtained by the numerical Maxwell equation [79] using the trapezoidal rule with a field change of ΔH of n field steps:

$$\Delta S_T(T, \Delta H) = \frac{\mu_0 dH}{2}\left(\frac{dM_1}{dT} + \sum_{k=2}^{n-1}\frac{dM_k}{dT} + \frac{dM_n}{dT}\right). \tag{3.9}$$

As this is a time consuming process, the entropy change of second-order materials was determined from $M(H)_T$ field steps, choosing temperature steps of 2 - 3 K. For ensuring thermal equilibrium the sample was kept at a certain temperature for 2 min prior to measurement. For the evaluation of ΔS_t the following equation based on Maxwell relation was used:

$$\Delta S_T(T, \Delta H) = \mu_0 \sum_{ij}\left(\frac{M_{i+1} - M_i}{T_{i+1} - T_i}\right)(H_{j+1} - H_j). \tag{3.10}$$

Pressure-dependent magnetization measurements were performed in the PPMS-14T using a pressure cell CC-Spr-Φ8.5-MC4 model 1.3 GPa from Quantum Design. Hereby the sample is placed together with a piece of Sn into oil and pressurized with Cu-Be pistons as shown in Figure 3.2. A maximum pressure of 1.3 GPa can be applied depending on the sample size. $M(T)_H$ measurements were performed with a heating and cooling rate of $0.5\,\mathrm{Kmin}^{-1}$ in order to compensate the high mass of the pressure cell. From the superconducting transition of the Sn sample the pressure within the cell can be determined

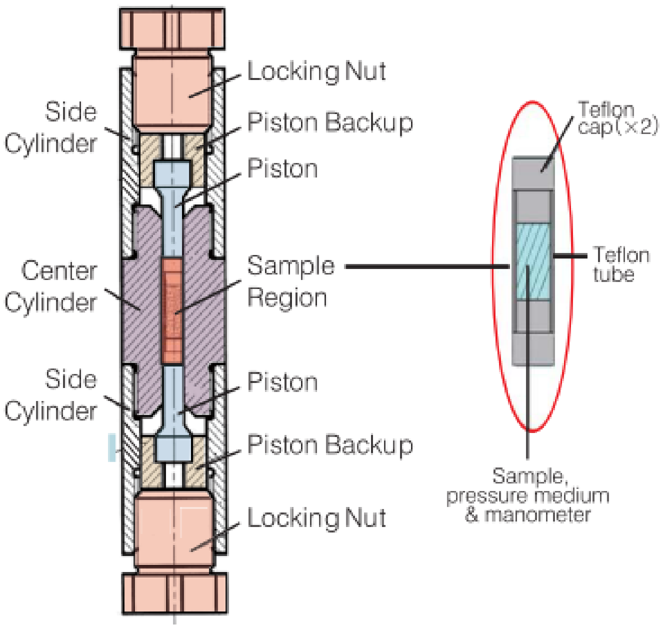

Figure 3.2: Schematic of the pressure cell used for pressure-dependent magnetization experiments. The image is taken from the pressure cell users manual.

from literature values [94]. The pressure in the cell is assumed to be temperature independent in a first approximation.

Single fragments of Fe_2P in the micrometer range were selected from a crushed sample under the microscope and mounted to the sample holder with kapton tape. The frequency and amplitude of the PPMS-14T VSM magnetometer were adjusted to account for highest precision and minimal noise. The actual size of the samples was calculated from the total magnetization measured under the assumption of a perfect spherical shape of the sample.

3.2.5 Measurements of the adiabatic temperature change in a Halbach setup and in pulsed fields

All measurements of adiabatic temperature change ΔT_{ad} shown in this thesis were measured directly in two different setups with distinct field application rate characteristics. ΔT_{ad} can be measured with two different protocols. The continuous protocol mimics the cyclic application of a material in a regenerator structure but incorporates the specific characteristics of thermal hysteresis. In this protocol the material is ramped to measurement temperature and the field is swept with continuous recording of the temperature change. The next measurement point is recorded by heating or cooling the sample to the next temperature and the process is repeated. As mentioned previously the material can be locked in thermal hysteresis and thus the continuous protocol is mostly applicable for second-order materials. However, the reversible ΔT_{ad} can be assessed using this protocol. On the other hand, the discontinuous protocol can assess the total thermodynamic ΔT_{ad} which is independent from previous measurements. In this protocol the material is always brought to a thermodynamic stable state, either completely ferromag-

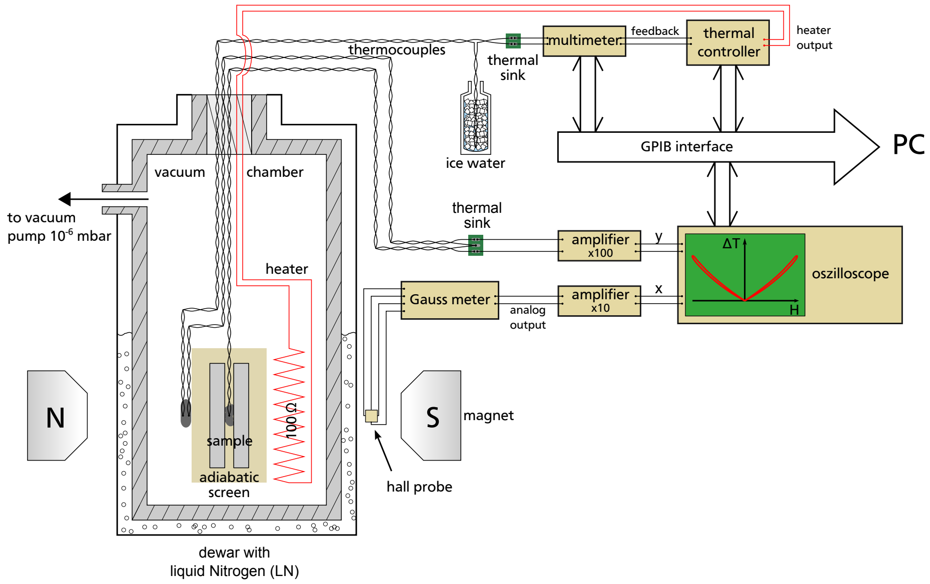

Figure 3.3: Schematic of the ΔT_{ad} measurement setup at TU Darmstadt. Image taken from [95], permission granted by Tino Gottschall.

netic or paramagnetic by heating or cooling prior to every field application. Both protocols were used in the framework of this thesis, and the protocol used is always mentioned.

Halbach array setup

Measurements with ”slow” field changes were performed in a custom built setup at the TU Darmstadt illustrated in Figure 3.3. The field source consists of two nested Halbach magnets rotating against each other achieving a maximum magnetic field of 1.93 T. The rotation is controlled by a stepper motor allowing for different rotations speeds generating a sinusoidal magnetic field profile. The sample temperature was constantly measured by a twisted home-made type T (Cu, Constantan) thermocouple. The end of the thermocouple was glued between two slates of the material using either thermal conductive epoxy or silver paste. A reference thermocouple measuring the absolute temperature against ice water was placed close to the sample. Thermal insulation in order to achieve adiabatic conditions was provided by wrapping the sample in isolating wool and by pumping the sample chamber with a turbo pump to a pressure better than 10×10^{-4} mbar. For temperature control of the sample a 100 Ω resistance coil heater tube was placed around the sample and the evacuated sample stick was placed into a liquid nitrogen Dewar. The magnetic field strength was measured by a Hall-probe sensor situated close to the sample tube. The magnetic field, the absolute temperature and the sample temperature are measured at the same time whereas the signal of the Hall-probe and sample-thermocouples are amplified and recorded by an oscilloscope. Temperature control was provided by a PID controller.

Pulsed-field setup

The ”fast” adiabatic temperature change measurements were performed at the Dresden High Magnetic Field Laboratory (HZDR) in a custom setup a user facility where one week of measurement time was applied for in order to perform these measurements. The magnetic field is generated by solenoids in which the sample holder is placed. Pulses of 2, 5, 10 and 20 T were applied resulting in a maximum field rate of 2700 Ts^{-1}. The adiabatic temperature change was measured similar to the setup in Darmstadt with a type T thermocouple, but with a much thinner wire diameter of 25 μm. In order to minimize the total length of the thermocouples a fork-like thermocouple was prepared with one end being glued in between two sample slabs by Ag-based epoxy and the other end fixed to the other side of the sample holder, close to the sample. Both the thin wires and the fork-like thermocouple are used in order to minimize induction caused by the magnetic field pulse. The thermovoltage of the thermocouple was amplified by a factor of 100. The temperature of the sample holder was measured by a PT100 temperature sensor. The sample stick was evacuated by a turbo pump to a pressure of 1×10^{-5} mbar and temperature control was performed by a resistance heater surrounding the sample and a liquid nitrogen dewar in which the sample stick is placed. The magnetic field strength is measured by a pick up coil placed on the end of the sample holder. The field profile versus time can then be obtained by integrating the measured induction signal by the field pulse. The characteristic field profiles for all pulses can be found later in chapter 6.8 of this thesis (Figure 6.19).

Even though many precautions where taken a small induced voltage signal overlapped the thermoelectric signal of the thermocouple. A consecutive reduction was performed for all measurements at different fields at a temperature far away from the transition. Eddy current heating is considered to be negligible.

4 Transition metal monoborides based on Mn and Fe

In the following chapter the magnetic and magnetocaloric properties of manganese and iron based monoborides are discussed. Magnetic transition metal borides are especially interesting for thermomagnetic applications as they show magnetic phase transitions in a wide temperature range [96, 97]. The materials can be implemented in a thermomagnetic generator as many of them show magnetic phase transitions far above room temperature. Reports have shown that the magnetic transition temperature can also be tuned to low temperatures allowing for the use in magnetic cooling.

Refractory borides are chemically inert and structurally stable even at elevated temperatures [98, 99]. Our primary interest in the monoboride system based on Iron and Manganese relates to the fact that MnB shows the highest magnetization of all monoboride systems [97] associated with a large magnetovolume effect [100]. FeB shows similar properties to MnB and shares the same crystal structure.

However, monoborides are difficult to prepare with high phase purity and precise composition due to the significant difference in melting temperatures of the constituents. As a result, experimental results found in literature significantly differ from each other [97, 101, 102, 103, 104, 105, 106]. First principle calculations on the pure compounds also highlight the important interplay between structure and composition related to the magnetic properties [99, 107, 108, 109, 110].

The findings shown in this chapter have been partially published in the following work:

- **M. Fries**, Z. Gercsi, S. Ener, K. P. Skokov and O. Gutfleisch, Magnetic and magnetocaloric properties of Mn based borides doped with Iron and Cobalt, Acta Materialia **112** (2014) 11256.

4.1 Experimental approach

Samples were produced via arc melting on a water cooled copper plate using commercial purity Mn (99.99 %), B (99 %), Fe (99.9 %) and Co (99.9 %). Before alloying, the manganese was cleaned by successive arc melting and grinding steps. The evaporation of Mn and B was taken into account by adding excess of 3 wt.% and 1 wt.%, respectively. In order to prepare FeB, an evaporation of B of 1wt.% was taken into account, like in the case of the Mn containing alloys. Arc melting was repeated three times to ensure material homogeneity. For each consecutive melting the sample was turned upside down. All investigated samples except $Mn_{0.5}Co_{0.5}B$ show homogeneous crystalline Pnma phase in the as-cast state. In order to prepare the material $Mn_{0.5}Co_{0.5}B$ an additional annealing step at 1473 K for 2 hours in a sealed quartz tube filled with Ar followed by water quenching was necessary to facilitate the formation of a single-phase material.

For the preparation of MnB and FeB for neutron diffraction experiments commercially pure Fe powder (99.9 %) was used with a mean grain size of 50 μm. Mn with a purity of (99.9 %) was melted in an arc-melter and the oxygen layer forming after melting was subsequently removed by a grinding step. The cleaned Mn was crushed and powderized in a mortar and sieved to a grain size of $< 50\,\mu$m in protective Ar atmosphere in the glovebox. ^{11}B powder, supplied by Zsolt Gercsi (Trinity College, Dublin) was used as a B source. The powders were mixed with an excess of 4 wt.% Mn, 0 wt.% Fe and 1 wt.% B and a total mass of 2 g was induction melted in a Al_2O_3 crucible in Ar atmosphere. The highly porous structure was remelted in the arc-melter to form a metallic pellet. For diffraction experiments the samples were powderized in a mortar under protective atmosphere stored there until the experiment.

The stochiometry and phase purity was checked with scanning electron microscopy (SEM) (Philips XL30 FEG) in back-scatter electron (BSE) contrast and energy dispersive electron spectroscopy (EDX) analysis by comparing the ratio of Mn/TM. As B is not detectable by EDX, we assume the ratio of B to be constant at 50 at.% as Mn/FeB are line compounds according to the phase diagram.

Differential scanning calorimetry (DSC) measurements were performed on a Netsch DSC 200 F3 Maia® under constant N_2 flow in an Al pan covered by an Al lid with a sweeping rate of 10 $\mathrm{Kmin^{-1}}$ on a powder sample of 40 mg. The DSC and c_p sensitivity was calibrated in the desired temperature range before the measurement.

Magnetic measurements were performed on sample fragments using a Quantum Design Physical Property Measurement System (PPMS 14 Tesla VSM) and a LakeShore vibrating sample magnetometer (VSM) with high temperature option. Magnetic isotherms were recorded in field steps of 0.05 T for cooling and heating in fields up to 4 T in the PPMS and 2 T in the VSM. Field cooling (FC) magnetization measurements were performed with a constant ramping rate of 3 $\mathrm{Kmin^{-1}}$ under a field of 1 T.

Temperature dependent neutron diffraction experiments of $Mn^{11}B$ and $Fe^{11}B$ were performed at the ISIS facility at Rutherford Appleton laboratory on the HRPD beamline from the 15.05 - 18.05.16.

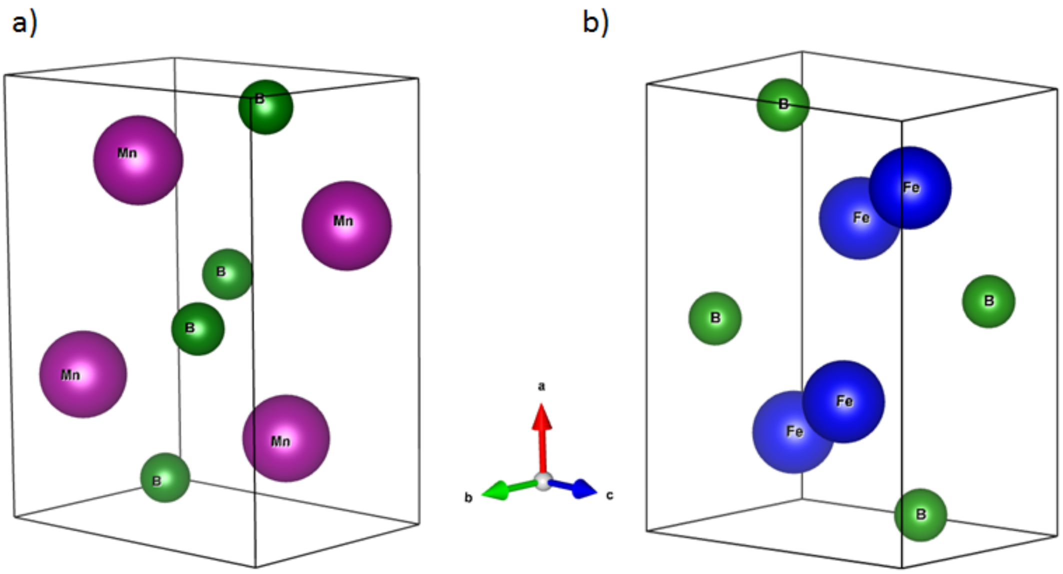

Figure 4.1: Crystal structure of a) MnB and b) FeB in the Pnma crystal structure with Mn, Fe and B sitting on the 4c sites of the crystal lattice.

4.2 Properties of pure MnB and FeB

4.2.1 Structural investigation of pure MnB and FeB

The crystal structure of both MnB and FeB are shown in Figure 4.1a) and b), respectively. Both MnB and FeB crystallize in the orthorhombic Pnma crystal structure with both Mn and Fe and B sitting on 4c crystal lattice sites.

The room temperature XRD measurement of MnB (see Figure 4.3a)) shows the diffraction pattern of an orthorhombic structure (*Pnma*, space group # 62) with $a = 0.558\,\text{nm}$, $b = 0.298\,\text{nm}$ and $c = 0.415\,\text{nm}$ in agreement with a previous study [111]. Besides the main phase, a small amount of Mn_2B impurity phase (<3 wt.%) was present, identified by Rietveld refinement.

A scanning electron microscopy image recorded in BSE mode is shown in Figure 4.2. The dark phase is the MnB main phase and the bright phase represents the Mn_2B secondary phase. A secondary phase content of 2-3 wt.% could also be confirmed by using the line intercept method. The Mn_2B also seems to be more brittle than the MnB main phase as the secondary phase tends to break out during the polishing step, as can be seen by the fragmentation of the phase in the SEM image.

The room temperature XRD pattern and the corresponding Rietveld refinement of FeB is shown in Figure 4.3b). FeB crystalizes in the same crystal structure as MnB with lattice parameters of $a = 0.551\,\text{nm}$, $b = 0.295\,\text{nm}$ and $c = 0.406\,\text{nm}$, which is in good agreement with the literature [112, 113]. The values are almost equal to those obtained on single crystals by Perkins [114]. A small amount of impurity phase

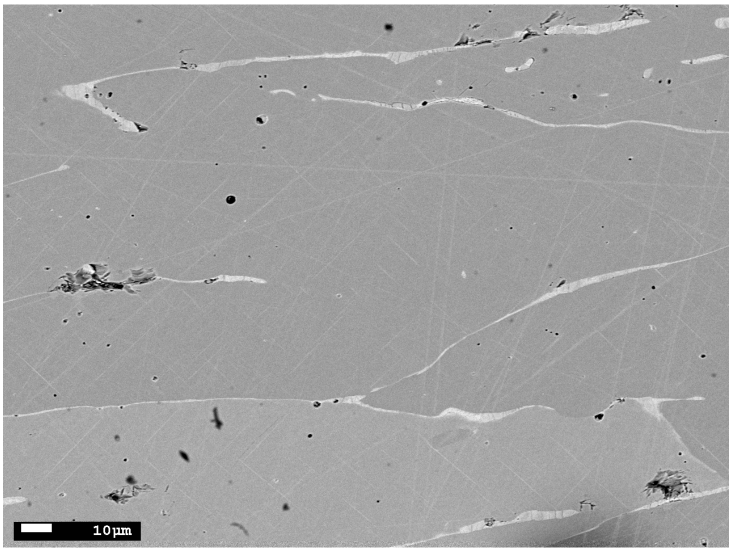

Figure 4.2: SEM image of MnB in BSE-mode showing two distinct phases. The majority phase is the MnB the white lines indicate the secondary phase Mn_2B.

could be found by Rietveld refinement (visible as a broad peak at 17.47°), yet the origin of this reflex remains unknown as all other reflexes could be indexed and fitted according to their peak positions and intensity relations. No secondary phase could be found in the SEM images in BSE mode. It is believed that the phase purity of the sampleis higher than 98% and is treated as a phase pure sample.

In comparison to MnB the lattice constants of FeB are slightly smaller following the trend of Vegards law.

4.2.2 Magnetic characterization

The temperature dependence of the spontaneous magnetization of MnB and FeB, M_s, is shown in Figure 4.4a) and b), respectively. The data was obtained from magnetic isotherms in a field change of 0 T to 4 T. For an accurate determination of M_s, Belov-Arrott plots [23, 24] were used according to the procedure described in [115]. The continuous line is a fit to the following expression proposed by Kuz'min [25]:

$$M_s(T) = M_s(0)\left[1 - s\left(\frac{T}{T_C}\right)^{\frac{3}{2}} - (1-s)\left(\frac{T}{T_C}\right)^{p}\right]^{\frac{1}{3}}, \tag{4.1}$$

where $M_s(0)$ is the spontaneous magnetization at 0 K and T_C is the Curie temperature.

The fitting parameters for MnB were found as $s = 0.7$ and $p = 10$. Such a large value of p is rather unusual (in most ferromagnets $p = 5/2$) and seems to be characteristic for Mn compounds (for instance p=6 in $GdMn_6Sn_6$ [116]). $M_s(0)$ is calculated as $156\,\mathrm{Am^2kg^{-1}}$ which is the highest of all monoborides reported in the literature.

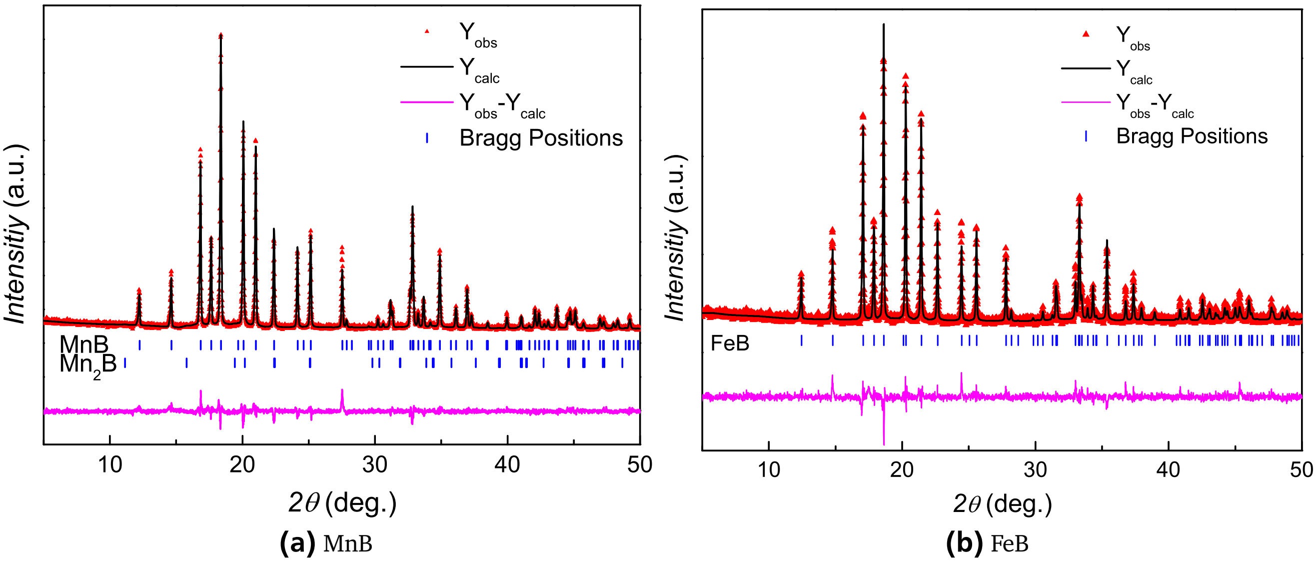

(a) MnB

(b) FeB

Figure 4.3: Room temperature XRD pattern of a) MnB and b) FeB with the corresponding Rietveld analysis.

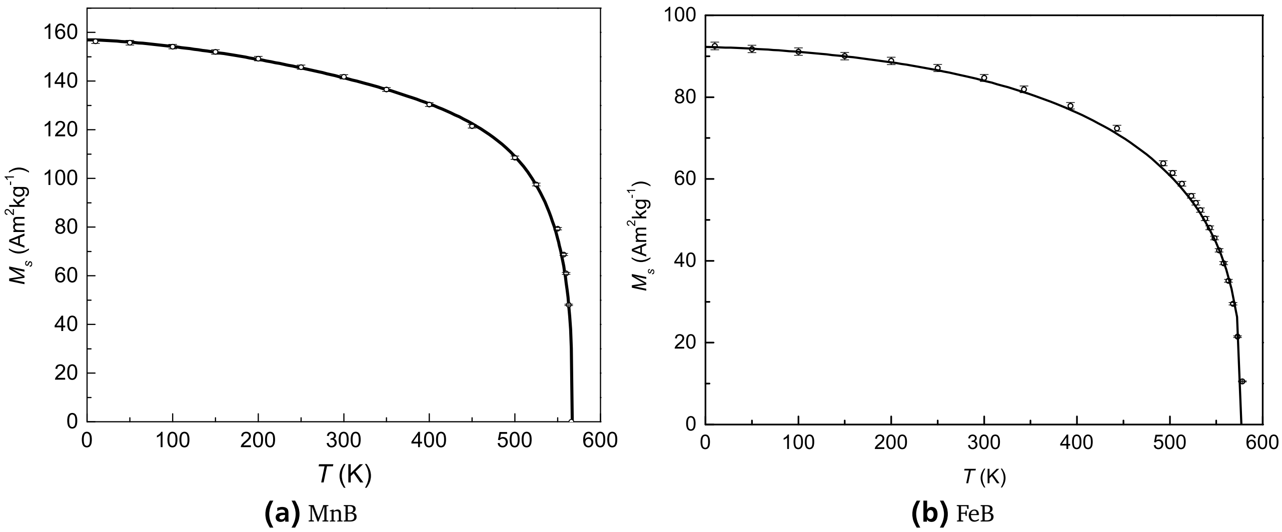

(a) MnB

(b) FeB

Figure 4.4: Temperature dependence of the spontaneous magnetization of a) MnB and b) FeB. The points indicate the M_s values obtained from Arrot-Belov plots. The continuous line shows the fit according to equation 4.1.

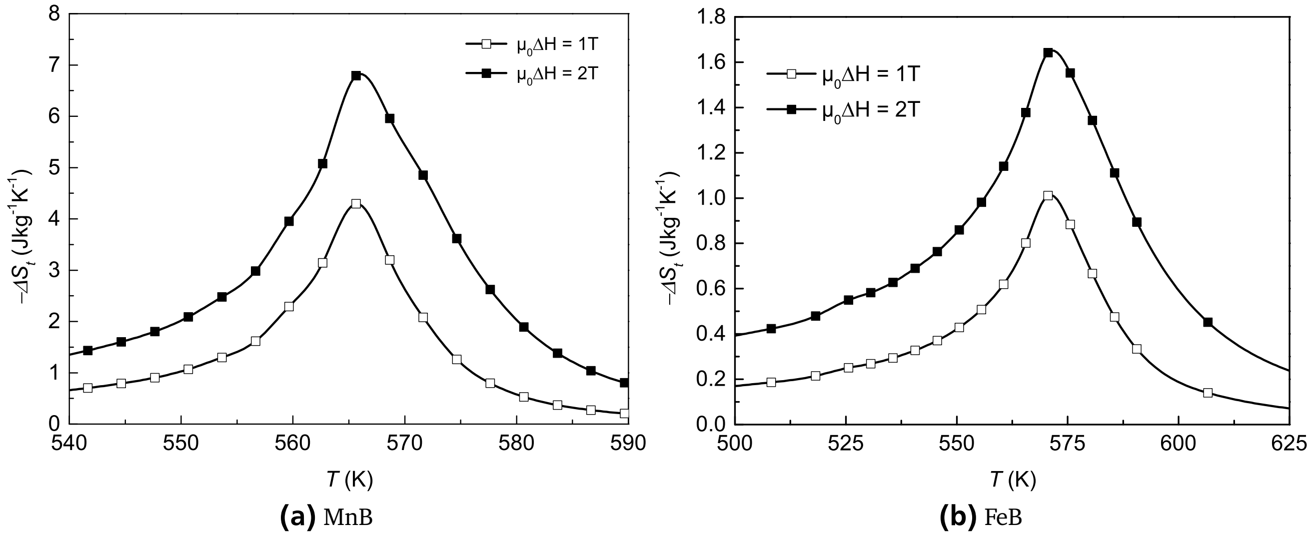

(a) MnB **(b)** FeB

Figure 4.5: Isothermal entropy changes versus temperature in a) MnB and b) FeB for field changes of 1 and 2 T. (The different scales on the y axis should be noted.)

MnB undergoes an abrupt ferromagnetic to paramagnetic transition with negligible hysteresis. T_C was estimated to be 567 K using Equation 4.1. This value is about 10 K lower than that reported previously in a thin film measured in a field of 0.05 T [106] or for a bulk value measured by Lundquist [102] and Kanaizuka [113]. This discrepancy can be explained by the different procedures used for obtaining T_C as it shifts with the different magnetic field applied during the measurement. In addition, slight composition differences may also yield different T_C values. From the paramagnetic Curie-Weiss law, we also determined the paramagnetic Curie temperature ϑ_p and found it to be at 579 K which is in agreement with literature values [102].

In the case of FeB shown in Figure 4.4b) the fitting parameters are $s = 0.5$ and $p = 3$, which are normal for a ferromagnet. FeB has a slightly higher Curie temperature than MnB with $T_C = 578\,\mathrm{K}$ which is in agreement with the literature [117]. The spontaneous magnetization $M_s = 92\,\mathrm{Am^2kg^{-1}}$ is much lower compared to MnB. Additionally, the transition in FeB is much more broadened compared to MnB. The absolute value of T_C is also around 10 - 15 K lower than proposed in literature [102, 112, 104] which may be explained by compositional differences or a difference in measurement procedure as previously mentioned for MnB.

ΔS_t values around T_C were calculated from measurements of magnetic isotherms, $M(H)|_T$ in a field change of 0 T to 2 T by using the numerical Maxwell Equation (Equation 3.10). The calculated magnetic entropy changes are shown in Figure 4.5. For the MnB alloy shown in Figure 4.5a), values of $4.3\,\mathrm{J\,kg^{-1}\,K^{-1}}$ and $6.8\,\mathrm{J\,kg^{-1}\,K^{-1}}$ were obtained for field changes of 1 T and 2 T, respectively. These obtained entropy changes are the highest values reported in the literature in this elevated temperature interval. In Figure 4.5b) entropy change values of $1\,\mathrm{J\,kg^{-1}\,K^{-1}}$ and $1.7\,\mathrm{J\,kg^{-1}\,K^{-1}}$ could be obtained for FeB in a field change of 1 and 2 T respectively. The large decrease in ΔS_t in comparison to MnB can be explained by the lower magnetization and the much broader phase transition of FeB.

4.2.3 Estimation of the thermodynamic efficiency of MnB

In order to judge the thermodynamic efficiency of MnB the efficiency was calculated according to the model described in Equation 2.14 proposed in [78].

A temperature interval of ΔT of 6 K between $T_{cold} = 563\,\mathrm{K}$ and $T_{hot} = 569\,\mathrm{K}$ was chosen with a field change of 3 T in order to compare the obtained values to Table 2.1. From the heat capacity curves shown in the inset of Figure 4.12a) a heat input Q_{in} of $6.186\,\mathrm{Jg^{-1}}$ was estimated with a magnetic output work from $M(H)_T$ curves (not shown) of $W_{out} = 0.050\,\mathrm{Jg^{-1}}$ leading to an absolute efficiency η_{abs} of 0.008. The Carnot efficiency η_{carnot} at this temperature interval is 0.0105. According to equation 2.14 the relative efficiency η_{rel} of MnB is 76% near the transition temperature under the above mentioned conditions. This is in comparison to the values given in Table 2.1 the highest value reported so far for a thermomagnetic material. The value is about four times higher as for example in Gd making MnB a very interesting candidate for thermomagnetic power conversion. However, it should be mentioned again as described in chapter 2.3.2 that absolute values should be treated with great caution.

4.3 $Mn_{1-x}Co_xB$ and $Mn_{1-x}Fe_xB$

Manganese atoms were substituted by cobalt and iron, respectively, in order to explore its effect on the magnetic transition temperature and entropy change. For this purpose, a series of samples, $Mn_{1-x}Co_xB$ with Co content varied between x=0.25 to x=0.9 as well as another series of alloys, $Mn_{1-x}Fe_xB$, with Fe contents of x=0.4, 0.5 and 0.6 were prepared. As already reported in the literature [104, 105], a broad compositional range of solid solubility is expected for the investigated compositions.

4.3.1 Structural characterization

All the samples were found to crystallize in the same orthorhombic (Pnma) structure as the pure MnB, FeB and CoB compounds. Small additional secondary phases of Mn_2B ($< 5\%$) could be observed in some samples of the composition $Mn_{1-x}Co_xB$ by means of XRD and SEM. The actual compositions of the main phase were adjusted to show no deviations from the nominal compositions within the error range of EDX measurements ($\approx$ 3 at%). The evolution of the XRD patterns with increasing Co content is shown in Figure 4.6a). Traces of secondary phase can be observed in the compounds $Mn_{1-x}Co_xB$ with x=0.1, 0.2 and 0.4, as indicated by the dotted lines. In the inset of Figure 4.6a) the evolution of the (101) and (200) diffraction peaks is shown as a function of composition. The peaks are both shifted monotonously to higher angles upon substitution of Mn with Co indicating a lattice shrinkage in a and c.

The lattice parameters for all studied compositions are listed in Table 4.1 and will be presented graphically later in Figure 4.16. The lattice parameter a decreases slowly with Co doping from a=0.558 nm to 0.548 nm in the compound $Mn_{0.5}Co_{0.5}B$ and it further drops to 0.539 nm in the compound $Mn_{0.25}Co_{0.75}B$. This behavior is also seen in the c lattice parameter. It changes from c=0.415 nm to 0.401 nm from x=0

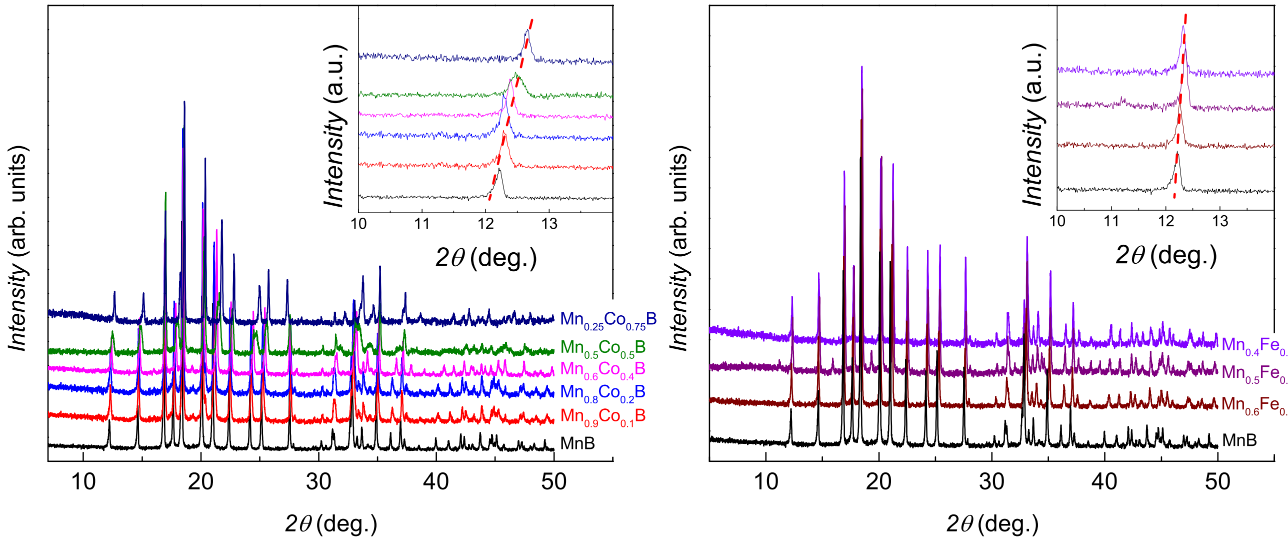

(a) **(b)**

Figure 4.6: The room temperature XRD patterns of samples $Mn_{1-x}Co_xB$ with increasing cobalt content in a) and $Mn_{1-x}Fe_xB$ with increasing iron content in b). The doted lines indicate the (200) and (002) reflexes of the secondary Mn_2B phase. The insets of a) and b) show the evolution of the (101) and (200) reflection in more detail.

to x=0.75 monotonously. Whereas the *b* lattice parameter behaves oppositely and decreases with the increasing Co concentration. The unit cell volume shows a gradual shrinkage from 0.0691 nm^3 for MnB to 0.0648 nm^3 for $Mn_{0.25}Co_{0.75}B$.

All the Fe-doped compositions form the same phase with Pnma crystal symmetry similar to the parent compound. The XRD patterns of the alloys are shown in Figure 4.6b). As it can be seen from inset of Figure 4.6b) doping with Fe shifts the reflections of (101) reflex to higher angles similar to the Co containing samples. Contrary to the Co-alloyed counterparts, the (200) reflex is only slightly shifted, indicating only small changes in the *a* lattice parameters by the Fe dopant. Only lattice parameter *c* shows a decrease with Fe alloying as shown in Table 4.1 and later in Figure 4.16.

Table 4.1: Lattice parameters and unit cell volume of the compounds $Mn_{1-x}Co_xB$ and $Mn_{1-x}Fe_xB$ obtained from Rietveld refinements of XRD data.

Composition	a (nm)	b (nm)	c (nm)	$V_{unitcell}$ (nm^3)
MnB	0.558	0.298	0.415	0.0691
FeB	0.551	0.295	0.406	0.0660
$Mn_{0.9}Co_{0.1}B$	0.555	0.298	0.414	0.0684
$Mn_{0.8}Co_{0.2}B$	0.554	0.297	0.412	0.0678
$Mn_{0.6}Co_{0.4}B$	0.550	0.297	0.408	0.0668
$Mn_{0.5}Co_{0.5}B$	0.548	0.297	0.406	0.0661
$Mn_{0.25}Co_{0.75}B$	0.539	0.300	0.401	0.0648
$Mn_{0.6}Fe_{0.4}B$	0.555	0.298	0.412	0.0681
$Mn_{0.5}Fe_{0.5}B$	0.554	0.296	0.410	0.0672
$Mn_{0.4}Fe_{0.6}B$	0.554	0.297	0.410	0.0675

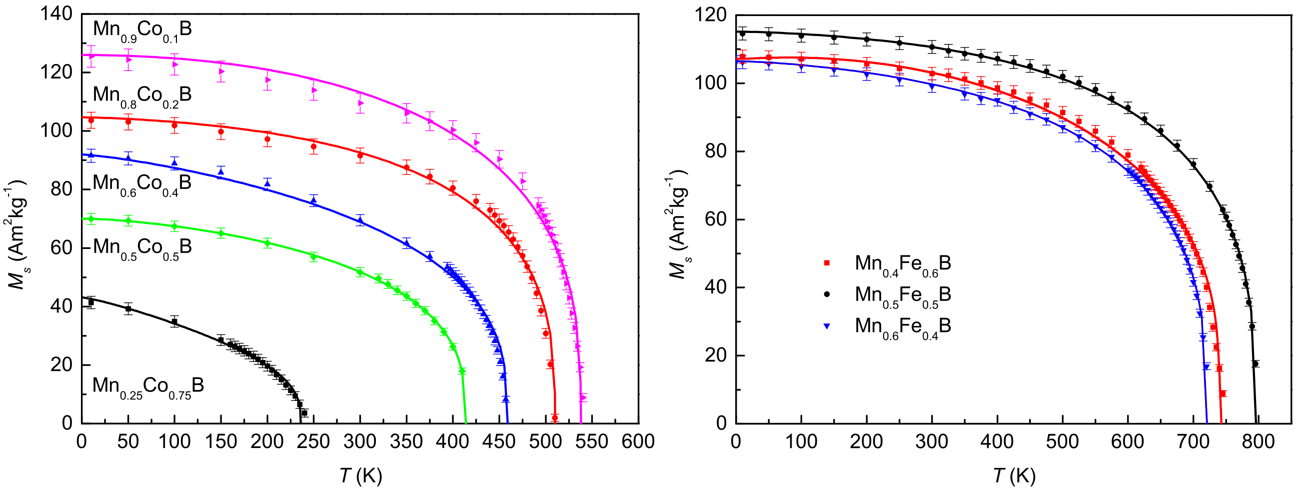

(a) **(b)**

Figure 4.7: Temperature dependence of the spontaneous magnetization of the system $Mn_{1-x}Co_xB$ for different Co concentrations in a) and $Mn_{1-x}Fe_xB$ for different Fe concentrations in b). Symbols indicate the M_s values obtained from Arrot-Belov plots. The lines show the fits to Equation 4.1.

4.3.2 Magnetic properties

The temperature dependence of spontaneous magnetization of $Mn_{1-x}Co_xB$ obtained from Arrot-Belov plots for all the measured compounds is shown in Figure 4.7a). Solid lines are fits according to Equation 4.1. With the gradual increase of the Co content both the magnetization and T_C decrease while the transition also broadens. In comparison with the ferromagnetic T_Cs, the measured paramagnetic Curie temperatures of all investigated samples are shown in Figure 4.8 together with previous values from the literature. Indeed, the decrease in Curie temperature with increasing Co content is in qualitative agreement with the values reported by Lemius and Küntzler [104] from NMR investigations. Apart from the compound $Mn_{0.9}Co_{0.1}B$, all compounds exhibit a PM T_C that is higher than the ferromagnetic one.

The spontaneous magnetization of $Mn_{1-x}Fe_xB$ compounds as a function of temperature is shown in Figure 4.7b). The $Mn_{0.5}Fe_{0.5}B$ compound shows the highest M_s (115 Am^{2}Kg^{-1}) and T_C (796 K) among the $Mn_{1-x}Fe_xB$ samples. In addition, the magnetic transition is also the sharpest. All obtained T_C values (both paramagnetic and ferromagnetic) for the Fe substitution are shown in Figure 4.8. A non-monotonous decrease of T_C also matches with the earlier work by Kanaizuka [113]. In contrast to the Fe substituted samples, no clear trend is observed in the Co substituted samples for the paramagnetic Curie temperature ϑ_p.

The reduced magnetic moment in the paramagnetic phase was suggested to increase the harnessable ΔS_t by Fujita et al. [118]. The calculated $T_C - \vartheta_P$ is the smallest for MnB (12K) and it augments with Fe concentration to 22, 40 and 34 K for x=0.4, 0.5 and 0.6, respectively. On the Co-rich side, significantly larger $T_C - \vartheta_P$ values (23- 106 K) are calculated without clear correlation to concentration changes suggesting the lack of collective spin arrangement as discussed in a later section of this chapter.

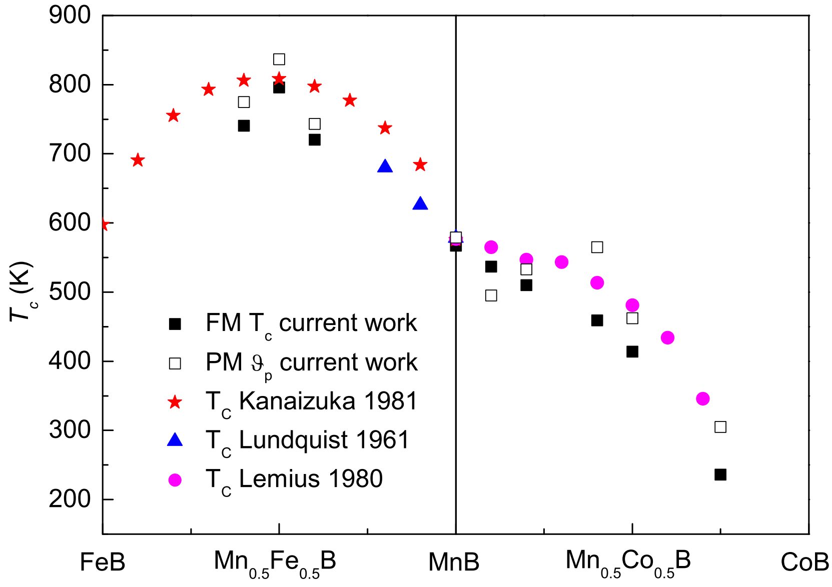

Figure 4.8: Change of the ferromagnetic (FM) T_C obtained by Arrot-Belov plots and paramagnetic (PM) T_C obtained by fitting the Curie-Weiss law for the compounds $Mn_{1-x}Co_xB$ and $Mn_{1-x}Fe_xB$ together with data from the literature [113, 102, 104].

Table 4.2: Ferro- and paramagnetic Curie temperatures, spontaneous magnetization and fitting parameters of Equation 4.1 for the compounds $Mn_{1-x}Co_xB$ and $Mn_{1-x}Fe_xB$.

Composition	FM T_C (K)	PM T_C (K)	M_s (Am^2kg^{-1})	s	p
MnB	567	579	158	0.7	10
FeB	578		92	0.5	3
$Mn_{0.9}Co_{0.1}B$	537	495	126	0.2	2.4
$Mn_{0.8}Co_{0.2}B$	510	533	105	0.5	3.4
$Mn_{0.6}Co_{0.4}B$	459	565	92	0.2	1.2
$Mn_{0.5}Co_{0.5}B$	414	462	70	0.9	2.6
$Mn_{0.25}Co_{0.75}B$	236	305	43	-183	1.5
$Mn_{0.6}Fe_{0.4}B$	721	743	103	0.7	3.5
$Mn_{0.5}Fe_{0.5}B$	796	836	115	0.4	3.5
$Mn_{0.4}Fe_{0.6}B$	741	775	111	0.7	3.5

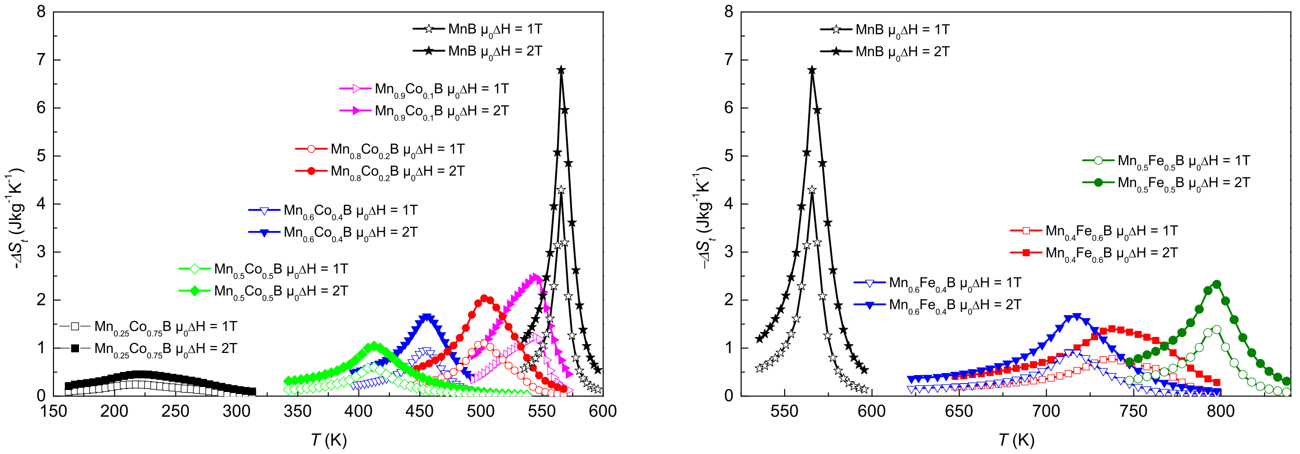

(a) **(b)**

Figure 4.9: a) Magnetic entropy changes of the compounds $Mn_{1-x}Co_xB$ for different Co contents, b) of the compounds $Mn_{1-x}Fe_xB$ for different Fe contents in field changes of 1 T (empty symbol) and 2 T (full symbol) as derived from Maxwell relations.

4.3.3 Magnetocaloric properties

The results of magnetic entropy change calculations are shown in Figure 4.9a) for $Mn_{1-x}Co_xB$. The entropy change calculated for $Mn_{0.9}Co_{0.1}B$ decreased to 2.5 $Jkg^{-1}K^{-1}$ for a field change of 2 T with a shift in maximum entropy change value to a lower temperature as expected from the shift of T_C. The magnetic entropy change is less than half of that of the pure compound MnB (6.8 $Jkg^{-1}K^{-1}$) and with Co addition ΔS_t is further reduced. The compound $Mn_{0.25}Co_{0.75}B$ shows the lowest transition temperature and ΔS_t of 0.45 $Jkg^{-1}K^{-1}$. The reduced magnetic entropy changes of $Mn_{1-x}Co_xB$ alloys compared to the pure MnB compound can be explained by the decreased magnetization near the transition and by the broadened transition in temperature.

In the samples with high (x=0.6) and low iron content (x=0.4), the magnetic entropy change decreases rapidly, similarly to the Co doped counterparts. However, the equiatomic $Mn_{0.5}Fe_{0.5}B$ has the highest ΔS_t of 2.35 $Jkg^{-1}K^{-1}$ in field change of 2 T with a peak value just slightly below 800 K . This value is almost half than that for the pure MnB compound, yet the highest one reported in this temperature range.

From theory, the temperature derivative of the magnetic transition relates directly to the magnetic entropy change. However, in materials with second order type transition, the “sharpness” of the transition is limited, thus the value of ΔS_t suggests a direct relation with M_s. Indeed, the obtained ΔS_t seems to be directly proportional with the amplitude of spontaneous magnetization for all investigated compositions. The only sample that does not obey this trend and shows a significantly higher ΔS_t is the parent compound MnB. As mentioned, MnB was reported to show strongly negative thermal expansion up to T_C [100] similar to other Mn-based materials [119, 120]. In latter materials, the strong Mn-Mn exchange competition results in a non-collinear spin arrrangement with measurable MCE at the triple point.

Additionally, recent DFT calculations suggest a possibility for the formation of MnB within a different orthorhombic symmetry, namely Cmcm (63) [121]. A potential mechanism for a phase transition from a Pnma to Cmcm structure is twinning at the unit cell level [122].

4.4 Clarification of the nature of the phase transition in MnB and FeB

The ground states of transition metal monoborides were calculated by Zsolt Gercsi (Trinity College, Dublin) with a DFT calculation at 0 K and the results of the most stable structure were compared to available literature values. Hereby, the difference between the Pnma and Cmcm crystal structures was investigated. The results are shown in Figure 4.10. As FeB and MnB are the only monoborides known to be ferromagnetic, the ferromagnetic (FM) and paramagnetic (PM) ground states were calculated for both crystal structures. The theoretical calculations show that the paramagnetic monoborides with Ti and Co crystallize in the Pnma structure and that the one with V, Cr and Ni crystallize in the Cmcm crystal structure. This is consistent with literature [96] and the ground states could be correctly calculated by DFT. In the case of FeB one can see that the FM ground states shown in red only exhibit a very small energy difference, but the Pnma structure seems to be more stable than the Cmcm structure. In most phase diagrams only one crystal structure of FeB is present, yet FeB crystallizes in two different structures, the most common high temperature β-FeB structure with Pnma crystal structure, known as the high temperature phase and α-FeB in Cmcm crystal structure, known as the low temperature phase. Both modifications are ferromagnetic and the low temperature α-FeB modification was firstly described by Fruchart *et al.* [123]. This phase can be obtained by low temperature synthesis or by mechanical working [124].

The FM ground state for MnB was calculated to be Pnma, which fits well to literature and our results. Yet, the existence of a low temperature crystal phase of MnB was also reported [105]. Analogue to the FeB system the high temperature phase was named β-MnB with Pnma crystal structure and the low temperature phase α-MnB in Cmcm structure [125]. The structure was first observed in single crystals grown by a chemical transport technique, below a temperature of 1323 K [126]. The magnetic properties of this α-MnB phase are not well studied as they were determined from samples that were ball milled for many hours in order to transform from the Pnma crystal structure to the Cmcm crystal structure. Results show, however, that the M_s and T_C are lower in α-MnB than compared to the β-MnB structure [127] which is also in agreement with our preliminary studies on single crystals.

The crystal structure of MnB in the Cmcm modification is shown in Figure 4.11. Both the Pnma and Cmcm crystal structures are geometrically closely related with each other and the transition between both structures can be made by successive shifts of the (010) planes along the [100] direction and choosing a new unit cell by rotation of 70° of the crystallographic axes a and b. The coordination number remains unchanged to the Pnma crystal structure and the relative positions of the Mn atoms remain unchanged. The orientations of all atoms change relative to the a and b-axes, as well as the positions of the B atoms in regard to the Mn atoms. The differences in magnetic properties can therefore be ascribed to the different bond length of Mn-Mn and Mn-B in the Cmcm structure compared to the Pnma structure.

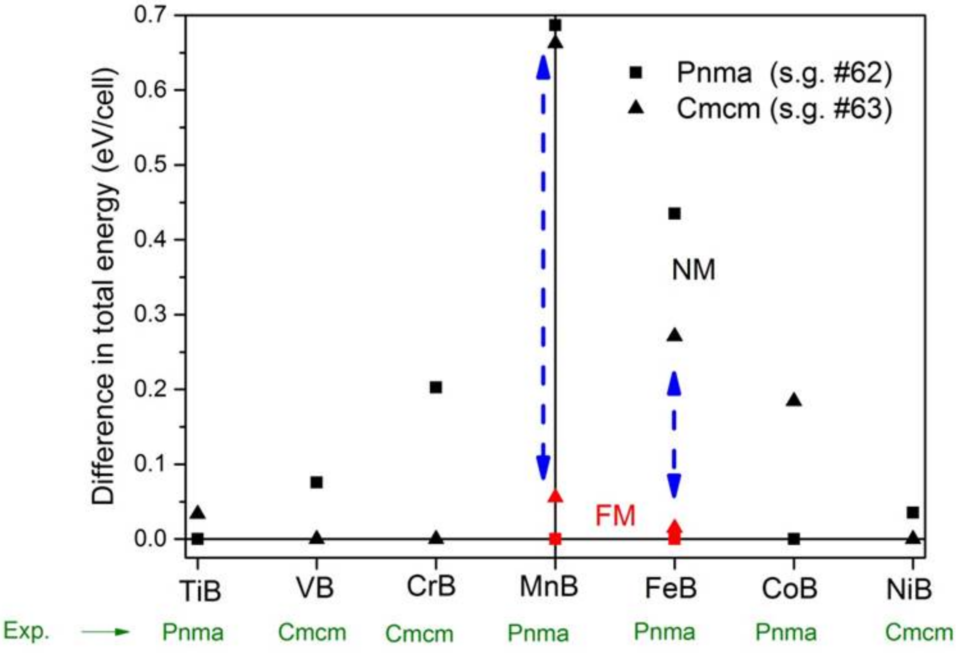

Figure 4.10: DFT calculation of the base structures in magnetic and non-magnetic states for several monoborides at 0 K, including experimentally assessed crystal structures.

Looking at the PM ground states of MnB and FeB in Figure 4.10 one can see that DFT calculations yield a lower total thermodynamic energy for the Cmcm structure than for Pnma structure. Calculations suggest that the crystal structure will transform above the Curie temperature in our case from a Pnma FM structure to a PM Cmcm structure undergoing a first-order phase transition.

In order to clarify the nature of the phase transition, DSC curves of MnB and FeB were recorded in a temperature interval between 350 to 650 K for heating and cooling. They are shown in Figure 4.12a) and b), respectively. For MnB shown in Figure 4.12a) endothermic and exothermic peaks can be observed in both the cooling and heating branches that correspond to the magnetic-ordering temperature with $T_t = 574$ K for heating and 588 K for the cooling branch. The shift in the maximum values are due to the relatively fast heating and cooling speeds of the measurements. The heat capacity c_p calculated from the cooling curve is plotted in the inset of Figure 4.12a). The heat capacity shows a sharp peak in a narrow temperature interval mirroring the sharp magnetic phase transition. The heat needed to drive the transition is comparable to other second-order magnetocaloric phase change materials like Gd [128].

For FeB, the DSC curves are shown in Figure 4.12b). Only very small endo- and exothermic peaks can be observed compared to MnB in Figure 4.12a). The peak temperatures of 578 and 575 K correspond to the magnetic transition in FeB and their shift can be explained by the fast heating and cooling speeds of the measurements and not by a hysteretic property of a first-order phase transition.

The nature of a phase transformation can be judged in first approximation by considering the Banerjee criterion by using purely magnetic methods [129]. The presence of a negative slope in the H/M versus

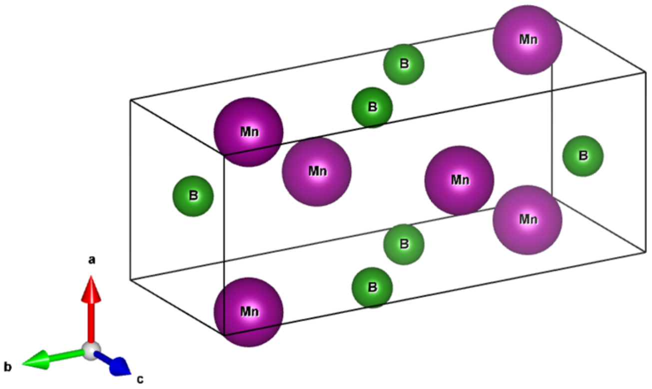

Figure 4.11: MnB in Cmcm crystal structure with Mn and B atoms sitting on 4c atom sites in the crystal structure.

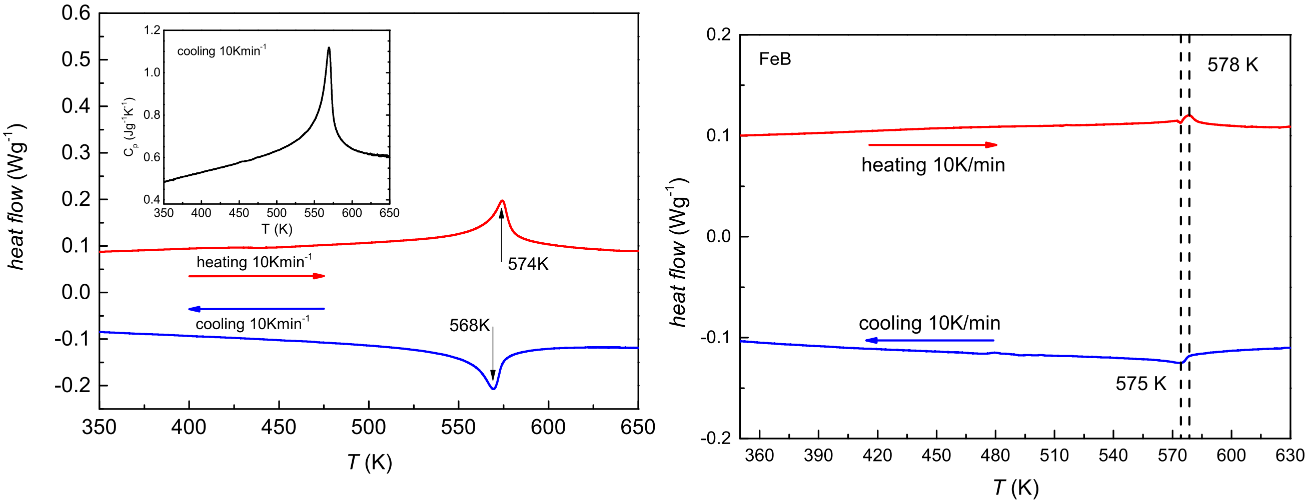

(a) MnB **(b)** FeB

Figure 4.12: DSC measurements on MnB in a) and FeB in b) in zero field for a heating and cooling sweeping rate of $10\,\mathrm{Kmin}^{-1}$. The inset of a) shows the heat capacity c_p calculated from the cooling curve.

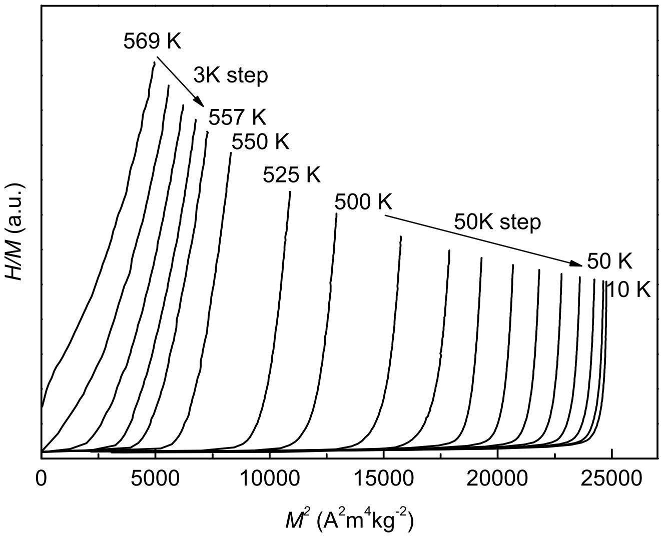

(a) MnB

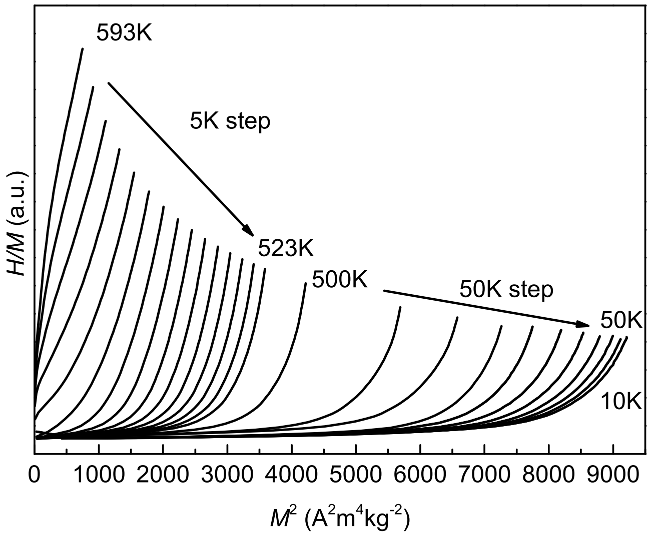

(b) FeB

Figure 4.13: The Arrot-Belov plot of the compound a) MnB and b) FeB derived from magnetic isotherms in field changes of 0 to 4 T and 0 to 2 T, respectively at different temperatures.

M^2 curves near the transition temperature indicates the presence of a first-order phase transformation. Arrot-Belov plots obtained from $M(H)_T$ measurements in fields of 0-4 T for MnB and 0-2 T for FeB are shown in Figures 4.13a) and b), respectively. One can see no indication of a first-order phase transformation, as the slope is always positive for MnB as well as for FeB. However, one has to take into account that the Banjeree criterion does not always work properly especially for materials close to a tricritical point due to the small size of the discontinuity of the free energy derivatives at the transition. Therefore the changes in physical magnitudes at the first-order transition are reduced, making its ascription very difficult by inspection of experimental magnetization measurements only [130, 131].

Temperature dependent XRD measurements on MnB have not shown any indication of a structural transition, but a negative volume change of around -0.13% around the Curie temperature [100] could be observed.

In order to study the transition in more detail, high resolution neutron powder diffraction (HRPD) was performed on the samples from 4.2 K to above the transition temperature T_t. In Figures 4.14 and 4.15 the lattice parameters a, b and c as well as the calculated unit cell volume V are shown for MnB and FeB, respectively. No magnetic scattering was taken into account when fitting the unit cell.

Both phases MnB and FeB could be fitted to the Pnma crystal structure over the whole temperature range. All the maximal isomorphic subgroups of lowest index and minimal non-isomorphic supergroups were fitted, but the fits did not converge for all of them. Therefore no structural first-order phase type phase transition could be found either in MnB nor in FeB. The theoretical ground state calculation in Figure 4.10 could therefore not be validated.

In Figure 4.14d) the temperature dependent unit cell volume of MnB is shown. The unit cell volume stays nearly constant up to 100 K and then rises almost linearly with temperature to a temperature of 550 K followed by a sudden drop. The unit cell shrinks up to the transition temperature of 567 K from where it then continuously rises again. The same trend of the curve is visible for lattice parameter c shown in Figure 4.14c). The unit cell expands in a non-linear way in a direction and a shrinkage in b can be observed from a temperature of 450 K and below, shown in Figure 4.14a) and b) respectively. Neutron diffraction experiments were both done under heating and cooling and no hysteretic effects were observable within the measurements.

The results of the temperature dependent neutron diffraction analysis of FeB are shown in Figure 4.15. As in MnB, the unit cell volume in Figure 4.15d) stays nearly constant to a temperature of 100 K. Yet, in FeB a linear increase in unit cell volume can be observed with no invar-like properties and therefore no negative thermal expansion as in MnB. The unit cell increases in a and c direction (shown in Figures 4.15a) and c)) following the trend of the cell volume. Like in MnB, the lattice shrinks in b direction although the transition is much broader compared to MnB (compare to Figure 4.14c)) reflecting also the broader temperature dependent magnetic phase transition. No abnormal behavior of the lattice parameters could be observed close to the phase transition.

The strong invar effect in MnB as shown for lattice parameters c and the unit cell volume around the transition temperature suggests a strong coupling of the crystal lattice and the magnetic properties of the sample. Taking into account the rather large magnetocaloric effect in MnB as shown in the previous section and the lambda like peak in the heat capacity one could conclude the nature of the transition to be of first-order. On the other hand, the missing occurrence of thermal hysteresis, the fulfillment of the Banerjee criterion for second-order phase transitions and no presence of a structural transition probed by temperature dependent neutron diffraction brings us to the conclusion that the transition in MnB is of second-order type. Considering all the facts, the transition in MnB can be assumed to be close to a tricritical point, combining both the positive features of a first- and second-order phase transition without the detrimental properties of large latent heat occurring during the phase transition as well as thermal hysteresis. The reason for the extremely sharp phase transition of MnB in comparison to that of FeB remains unclear so far. For better understanding a careful analysis of the interatomic distances of Mn and B during the magnetic phase transition could be performed coupled with theoretical calculations.

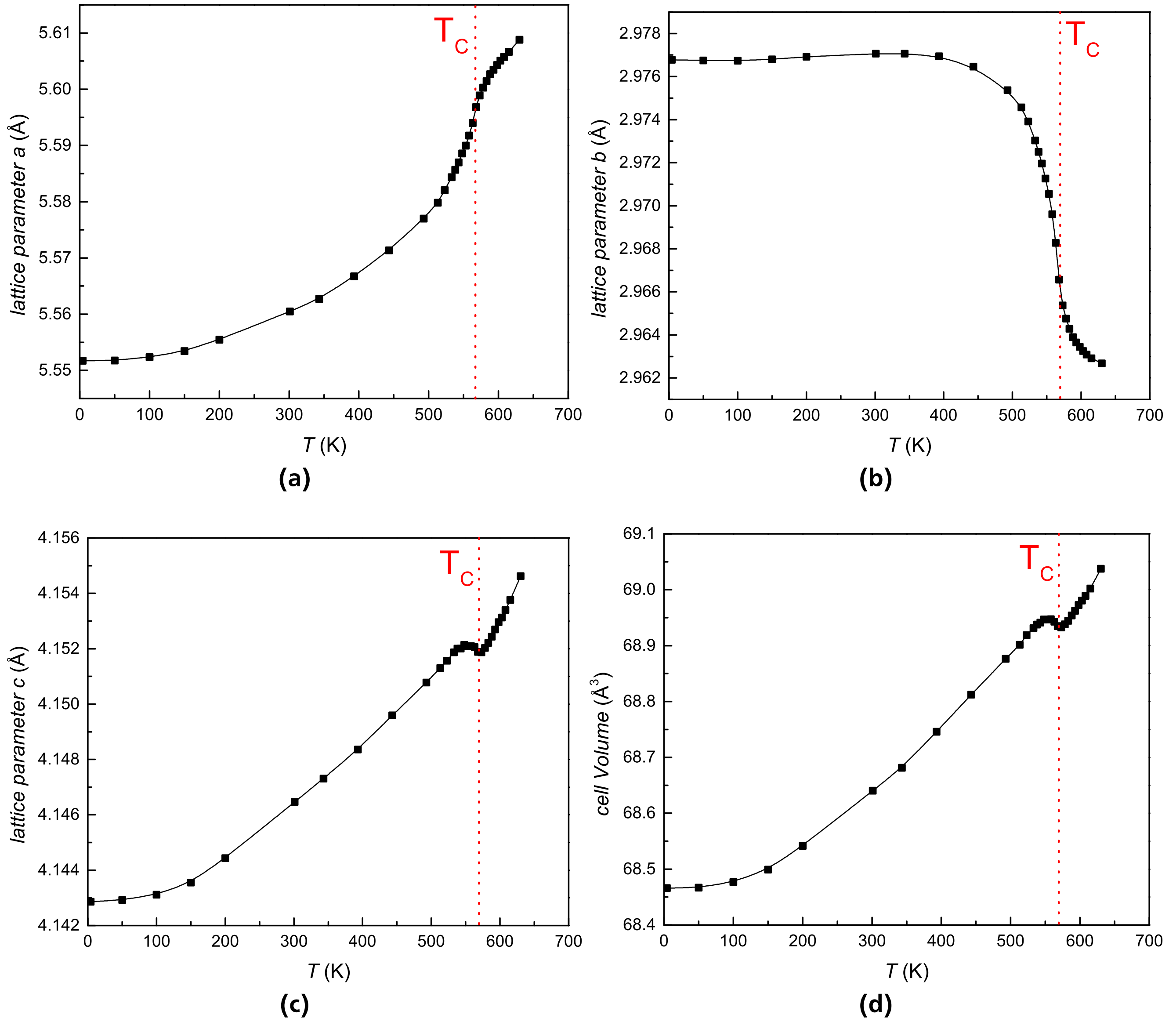

Figure 4.14: Temperature dependent lattice parameters a, b, c in a), b) and c), respectively and calculated cell volume of MnB in d) obtained by neutron diffraction. The dashed line indicates the Curie-temperature obtained by equation 4.1.

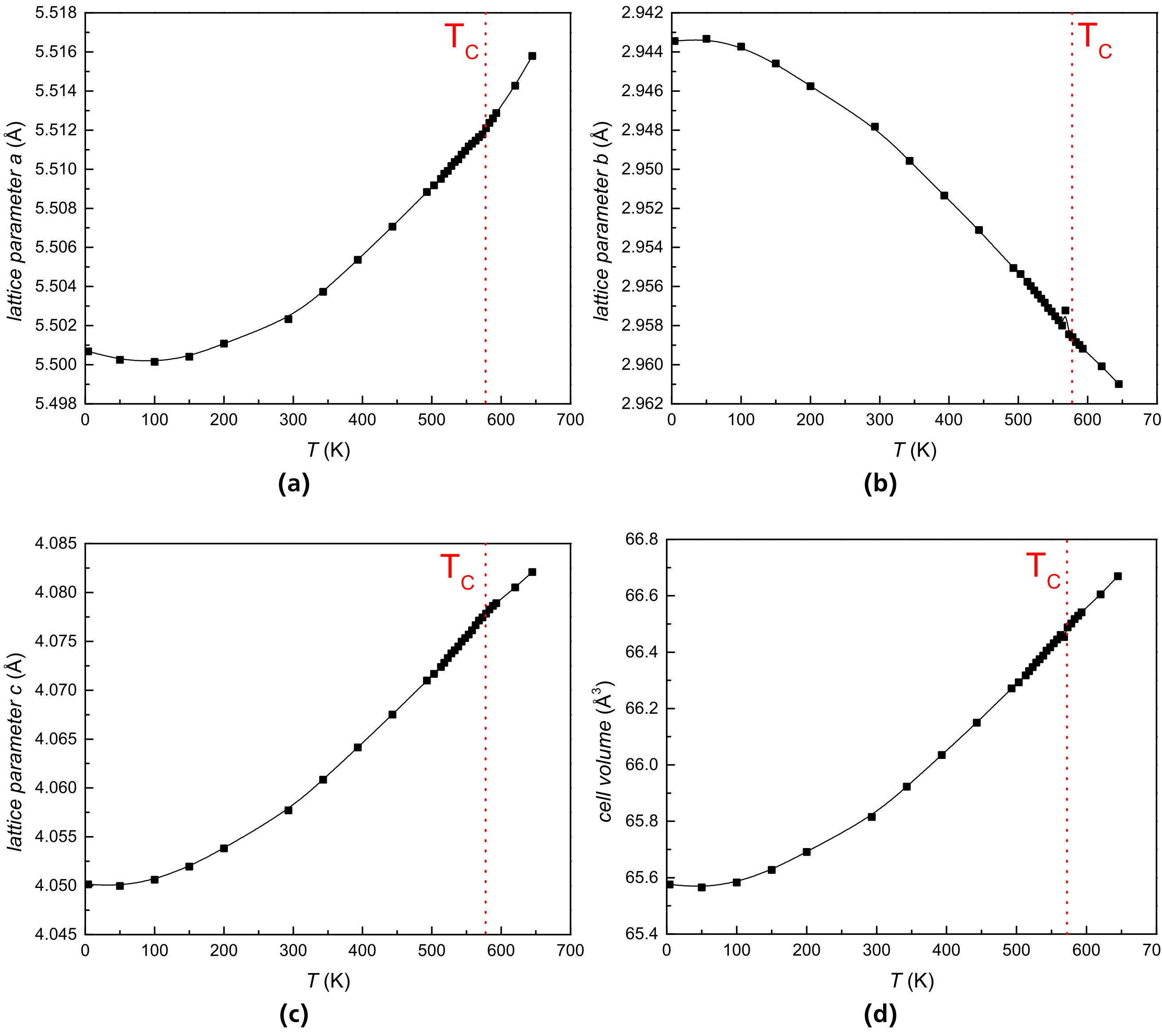

Figure 4.15: Temperature dependent lattice parameters a, b, c in a), b) and c), respectively and calculated cell volume in d) of FeB obtained by neutron diffraction. The dashed line indicates the Curie-temperature obtained by equation 4.1.

The nature of phase transition of FeB is of second-order. All measurements yield this behavior including the small entropy change, the lack of thermal hysteresis, the Banerjee criterion, DSC measurements and temperature dependent neutron diffraction. Due to the broad phase transition, FeB is therefore much less useful than MnB in context of the thermomagnetic regenerator as its efficiency will be much lower.

4.5 Theoretical calculations

The Density Functional Theory (DFT) calculations shown here were performed in collaboration with Zsolt Gercsi (Trinity College Dublin). The results of structural relaxation with the dopants is shown in Figure 4.16. Here, we follow the experimental approach. MnB is taken as the center point and the effect of Co (Fe) doping on the lattice and magnetic moments is plotted on the left (right) to it. The experimental data was collected at room temperature showing a complex behavior. The lattice parameter a peaks at the binary MnB composition shortening by both Co and Fe addition. The same tendency is found for lattice parameter c, whilst the b-axis shortens from CoB to FeB through MnB (left to right) in Figure 4.16. Neither the Vegard's law is observed (size effect) nor does the electron count (addition) correlate directly with the lattice dimensions. As a general feature, the FM order results in larger lattice parameters than that in the NM states. Based on the largest differences between the FM and NM lattice parameters, the strongest magneto-elastic response is expected for the binary MnB. Indeed, considering the unit cell volume MnB shows strong invar-type behavior experimentally, upon cooling through the magnetic ordering temperature. This behavior can be linked to the highest magnetic moment developed on the MnB compared to the FeB and CoB counterparts (explained below). At first, we use the well-established Stoner theory of itinerant magnetism to explain the origin of stable ferromagnetism in MnB and FeB, contrary to CoB. The condition upon ferromagnetism is stable can be given as [21]

$$I \cdot D(E_f) > 1, \tag{4.2}$$

where I is the Stoner exchange integral, typically in the order of 0.5 eV and D is the non-magnetic density of states (DoS) at the Fermi level.

In Figure 4.17, we compare the NM DoS of MnB, FeB and CoB as calculated by DFT. The energy landscape of the non-magnetic states shares many common features for all three investigated compounds. It has been well established that the stability of these transition metal (TM) monoboride (TM-B) compounds is linked to the dominant boron-boron (p-p) bonds along the boron chains beside the TM-B (p-p and d-p) interactions [99]. These interactions are of similar character in the investigated compositions and located in the ≈ -5 eV to ≈ -2 eV energy range.

A rigid-band description of the electronic properties works well for these compounds and the most significant difference among the compositions is the position of the Fermi level that mostly affects the magnetic properties. For MnB, the E_f is situated in the middle of the dense states dominated by 3d electrons. Indeed, the high number of $\mathrm{D}(E_f)=2.89\,\mathrm{eV/f\,u}$ ensures the satisfaction of Equation 4.2. With the electron addition from MnB to FeB, E_f is only shifted higher as the extra electron occupies additional states but the

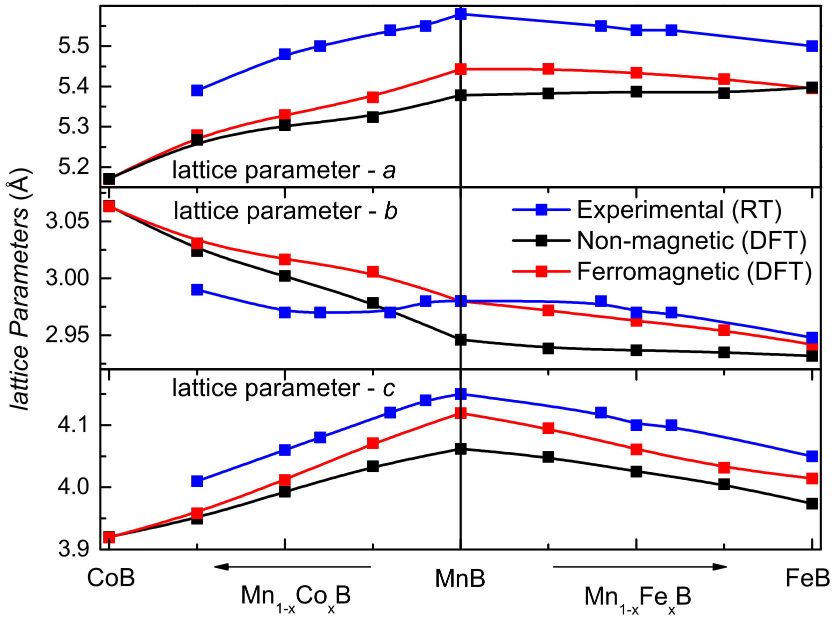

Figure 4.16: Evolution of lattice parameters with Co and Fe doping in MnB. The experimental results are compared to the relaxed ferromagnetic and non-magnetic solutions, respectively.

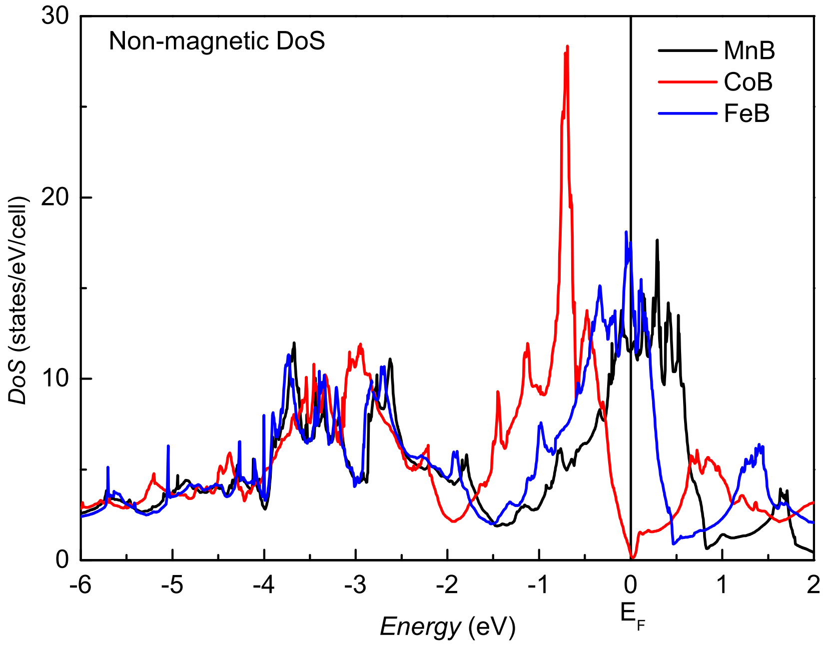

Figure 4.17: Non-magnetic density of states of MnB, CoB and FeB compounds for comparison.

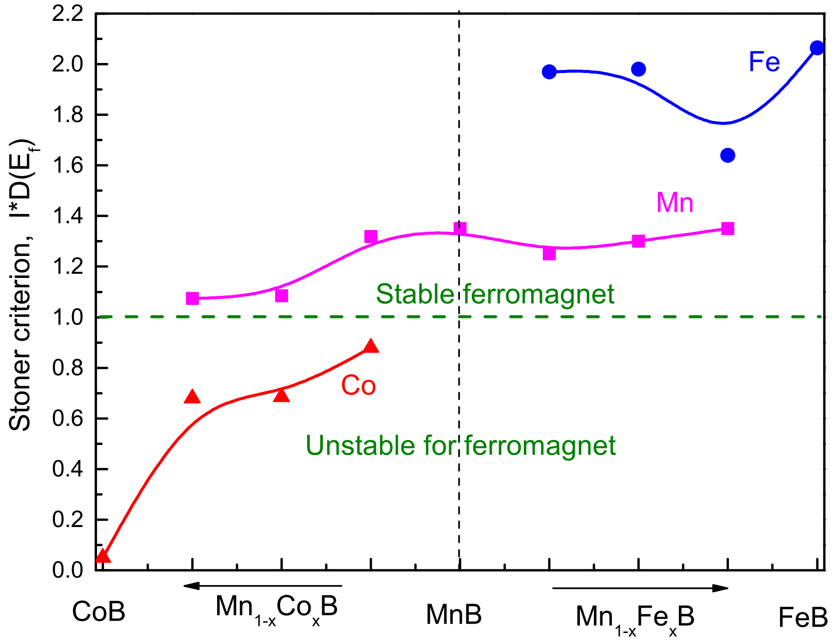

Figure 4.18: Stoner criterion of the transition metal elements in $Mn_{1-x}(Fe/Co)_xB$ alloys based on partial density of states.

energy landscape of these states is unaltered with $D(E_f)=4.38\,eV/fu$. When another electron is added as Fe is replaced by Co, the $D(E_f)$ sharply falls into a pseudogap with $0.08\,eV/fu$ and Equation 4.2 is no longer satisfied for ferromagnetism. One can use the same argument (Eq. 4.2) to further analyze the magnetic stability of the dopants using the partial density of states (PDoS). Replacement of Mn with Fe increases $D(E_f)$, which can be uniquely ascribed to the new states from Fe, without altered contribution for the Mn-states (not shown). On the other hand, the Co-substituents have little contribution to $D(E_f)$ and the Stoner criterion is not satisfied for these elements in the $Mn_{(1-x)}(Fe/Co)_xB$ alloys (Figure 4.18).

The expected magnetic moments from the calculations are shown in Figure 4.19. Binary MnB has the highest magnetic moment of $1.86\,\mu_B$. This is in full agreement with the experimental value of $1.84\,\mu_B$. The presence of Co or Fe elements in the lattice causes a reduction from latter value. This decrease can be attributed to both a lower moment of the dopant as well as to the reduced moment of Mn. By exploring the MnB-CoB pseudobinary line, it is visible that the Co atoms carry a much smaller magnetic moment compared to Mn, accounting for the sharp decrease in magnetization (left hand side of Figure 4.19).

The shortest Mn-Mn distances are dominated by the shrinkage in c-axis. The shortening Mn-Mn separations (d_1, d_2) result in broader bands with reduced magnetic moments. Recently, the effect of interatomic distance between manganese in the orthorhombic Pnma structure using the prototype MnP binary compound was calculated [132, 133]. A change in the magnetic coupling, FM(1) to antiferromagnetic (AFM) around 2.95 Å separation and another AFM to FM(2) transition around 3.37 Å were predicted. Based on these results, the complex, metamagnetic behavior of the magnetocaloric CoMnSi could be explained [119] and a new metamagnet was predicted for the first time based on CoMnGeP [133]. The above mentioned atomistic model also predicts the dominance of non-magnetic state (NM) over ferromagnetism when the shortest Mn-Mn distance is approaching the critical value around and below 2.66 Å.

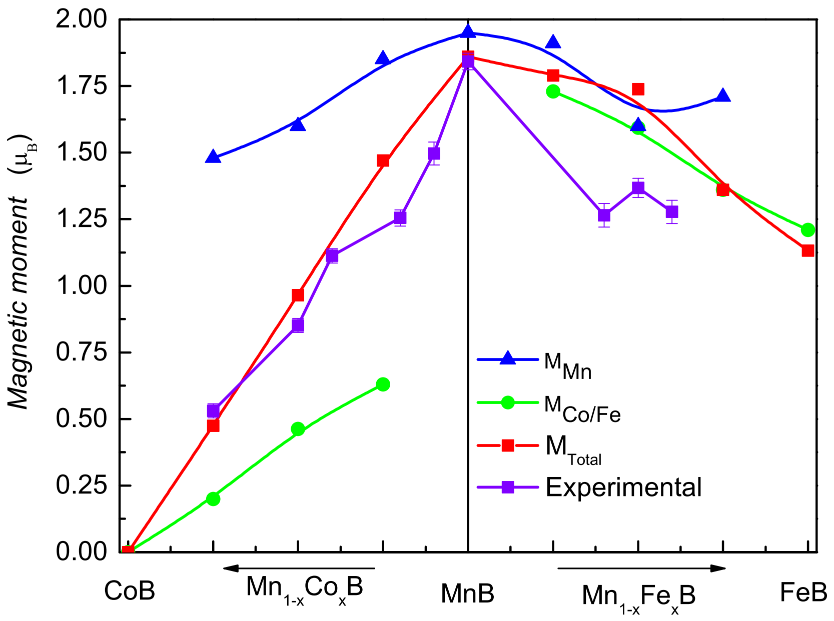

Figure 4.19: Evolution of magnetic moment as a function of Fe/Co-addition in $\mathrm{Mn}_{1-x}(\mathrm{Fe/Co})_x\mathrm{B}$.

The d_1 distance is strongly affected by the change in the c-axis that has a maximum at MnB ($d_1 = 2.67$ Å) and it drops with the smaller atomic radius of Co (152 pm) than that of Mn (161 pm) to 2.62 Å for CoB. The reduced magnetic moment of Mn reflects the expected trend towards a NM state. On the other hand, the moments of Co quickly vanish with the lower Mn concentration. Later findings, together with the unfulfilled Stoner criterion for Co elements (Figure 4.18) suggest that the magnetism on Co is induced only by the proximity of large Mn moments in the lattice. As for the ($\mathrm{Mn}_{1-x}\mathrm{Fe}_x\mathrm{B}$) pseudobinaries, the magnetic moment of Fe was found to be similar in size as compared to that of the Mn. Both decline with higher Fe concentration as a result of the shortening Mn(Fe)-Mn(Fe) separations. Indeed, the same magnetic trend with comparable values are also found experimentally. The main difference between the Co- and Fe-doped compositions is the nature of the Fe moments. The latter develop large and stable moments, similar to these of the Mn in the lattice.

In this chapter structural, magnetic and magnetocaloric properties of refractory MnB with its pseudobinary derivatives, $\mathrm{Mn}_{1-x}\mathrm{Co}_x\mathrm{B}$ and $\mathrm{Mn}_{1-x}\mathrm{Fe}_x\mathrm{B}$, are reported. We found that all samples share the same orthorhombic crystal structure (Pnma) at room temperature. The pure compound MnB shows M_s of 156 $\mathrm{Am^2kg^{-1}}$ which is the highest of all monoborides with a Curie temperature of 567 K. MnB shows a sharp ferromagnetic to paramagnetic phase transition with an entropy change of 6.8 $\mathrm{Jkg^{-1}K^{-1}}$ in a field change of 2 T with no hysteresis loss. The magnetic ordering temperature is tunable by the dopants: Fe-addition increases, whilst Co-addition acts oppositely and lowers T_C. However, the doping results in broader phase transitions causing a reduction of entropy changes in the alloys.

DFT calculations qualitatively account for our experimental findings as the energy landscape of DoS shares common features for the end compositions (MnB, FeB, CoB). The calculated high DoS(E_f) for MnB in the NM state ensures the energy gain by the ferromagnetic order according to the Stoner criteria. With the electron addition by Fe, the position of E_f shifts to higher energies, but the condition for ferromagnetism remains satisfied. On the other hand, additional electrons by Co shift the E_f to a valley in DoS, where the collective magnetic order is unstable for Co. Ab-initio calculations also capture the correct experimental trends and values for the lattice parameters of the investigated compositions within the expected discrepancy due to the 0 K nature of DFT. Based on the largest difference in the calculated NM and FM volumes, strong magneto-elastic interactions, manifested in anomalous thermal lattice expansions are expected in the binary compound as well as in the moderately Fe-doped samples. The reported anomalous thermal volume expansion in literature [100, 134] confirms these predictions, although, the sharp and non-hysteretic magnetic transition in MnB still requires further study. All samples showed no sign of mechanical fatigue due to cycling around the magnetic transition temperature. The nature of the phase transition could be clarified to be of second-order by various methods including neutron diffraction.

The here investigated refractory borides show tunable MCE with sharp, hysteresis free transitions at elevated temperatures that could be exploited for future, energy efficient thermomagnetic energy conversion.

5 Properties of Co_2B-based compounds

The magnetic and structural properties of the transition metal diboride systems M_2B, with M being one of the 3d transition metals from Cr to Ni have been investigated since their first report in 1962 by Lundquist *et al.* [103] and Cadeville *et al.* [112]. They have suggested that the dependence of the magnetic moment per metal atom on the outer shell electrons is very similar to the Slater-Pauling curve for $3d$ transition metal alloys. The difference is that the curve is shifted towards lower electron numbers and was attributed to the fact that the compounds have a partially filled $3d$ shell and the characteristics are similar to those of $3d$ transition metals. It was shown many years later that Co_2B exhibits a significant magnetovolume effect around its Curie temperature [135] making it potentially interesting for magnetocaloric purposes or thermomagnetic power generation as a large coupling between the lattice and magnetism is expected.

In order to study the influence of doping on the Co_2B system, Co was gradually replaced by Mn up to a Mn content of x=0.8 as already shown in [136, 137, 138]. This step has been undertaken in order to minimize the amount of Co, as it is considered a critical element by the EU [37] and far too expensive to enable mass production of this alloy. Mn is a good candidate for this purpose as it is cheap, widely available and previous results have shown that the Curie temperature could be tuned to lower temperature compared to the pure Co_2B. Fe would also be a suitable candidate for substitution, however it was shown that with increasing Fe content the Curie temperature will be increased. The addition of iron also leads to a gradual increase in M_s and shows features of uniaxial anisotropy at room temperature and is being explored as a potential candidate for Rare-Earth free permanent magnet applications [139, 140, 141, 142]. Recently, magnetic Co-Co_2B nanoclusters were explored in terms of their catalytic properties showing that they are suitable for the chemoselective reduction of aromatic compounds [143]. Additionally, Co_2B-base alloys were also explored as coatings of CoCrMo (ASTM-F75) alloys, not because of their magnetic properties but because of their chemical inertness and hardness intrinsic to borides [144].

The findings shown in this chapter have been or will be partially published in the following:

- **M. Fries**, K. P. Skokov, D. Yu. Karpenkov, V. Franco, S. Ener, and O. Gutfleisch, The influence of magnetocrystalline anisotropy on the magnetocaloric effect: A case study on Co_2B, Applied Physics Letters **109** (2016) 232406

- A. Edström, M. Werwinski, D. Iusan, J. Rusz, O. Eriksson, K. P. Skokov, I. A. Radulov, S. Ener, M. D. Kużmin, J. Hong, **M. Fries**, D. Yu. Karpenkov, O. Gutfleisch, P. Toson and J. Fidler, Magnetic properties of $(Fe_{1-x}Co_x)_2B$ alloys and the effect of doping by 5d elements, Physical Review B **92** (2015) 174413

5.1 Experimental approach

The $Co_{2-x}Mn_xB$ alloys were prepared by induction melting of commercial purity Co (99.99%, Mateck), Mn(99.99%, Mateck) and B (99.999%, Mateck) under argon atmosphere. Phase purity was confirmed by powder XRD and SEM in BSE mode. The stochiometry of the samples was adjusted according to the stochiometry obtained by deriving the Co/Mn ratio from EDX measurements. The shown compositions have an error of less than 3 at.%. No additional annealing step was necessary in order to facilitate the desired crystal structure. Polycrystalline pieces with a needle like shape were extracted from the ingots. Magnetic measurements were performed on a LakeShore 7400 series VSM magnetometer with the magnetic field applied along the needle. No demagnetization corrections were applied. Low temperature measurements $< 400\,\mathrm{K}$ were performed in a LN_2 flow cryostat. Measurements with higher temperature were performed in a furnace. The heating and cooling rate was kept at $2\,\mathrm{K\,min^{-1}}$ for $M(T)$ measurements.

In order to obtain single crystals the ingots were remelted under Ar atmosphere and slowly cooled to room temperature leading to enhanced grain growth. Large single crystalline grains were extracted and the crystalline quality and orientations were checked by Laue and powder XRD. For magnetic measurements the sample was cut into a $1\,\mathrm{mm} \times 1\,\mathrm{mm} \times 1\,\mathrm{mm}$ cube with edges parallel to [001] and [100], [010]. A polycrystalline sample was taken from the same pre-alloy batch as the single crystal. The size and shape of the polycrystalline sample was chosen to be comparable with the single crystal. In order to study the influence of magnetocrystalline anisotropy on the magnetocaloric effect, the adiabatic temperature change was obtained by means of direct measurements in a purpose-built setup described in chapter 3.2.5. Magnetic isotherms are recorded on a Quantum Design 14 T PPMS magnetometer and are analyzed using the Maxwell relation (Equation 3.10). Both measurements were carried out on a single crystal along [001] and [100], [010] (equivalent) directions and on a polycrystalline sample.

5.2 Properties of Co_2B

A schematic of the crystal structure of Co_2B is shown in Figure 5.2. Co_2B crystallizes in the tetragonal I4/mcm crystal structures with the Co atoms (shown in blue) sitting on the 8h and the B atoms (shown in green) on the 4a crystal lattice sites.

5.2.1 Structural properties

A Laue diffraction XRD pattern of a pure Co_2B single crystal is shown in Figure 5.2a). The pattern could be fully indexed. All the spots refer to specific crystallographic lattice planes of the tetragonal Co_2B structure. The c-axis of the crystal is perpendicular to the image plane and with the [102] and [012] crystallographic directions indexed in the image. One can see no additional reflexes when comparing the image to a simulated reflex pattern. A distinct broadening or doubling of the spots cannot be observed leading to the assumption that the crystal shows no sign of twinning or secondary phases and that the crystal is of good quality. This can be observed also in Figure 5.2b). Here, a powder XRD pattern is

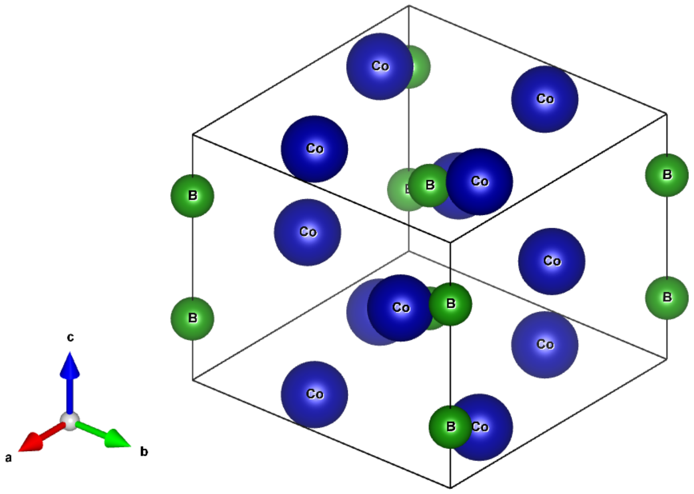

Figure 5.1: Schematic of the crystal structure of Co_2B crystallizing in the tetragonal I4/mcm crystal structure with Co atoms placed on 8h and B atoms on the 4a sites of the crystal lattice.

shown for a crushed piece of the single crystal measured at room temperature. This technique is by far more sensitive in terms of determination of secondary phases. The corresponding Rietveld simulation shows almost no deviation to the measured result and the lattice parameters of a, b = 0.501 nm and c = 0.422 nm could be fitted which are in good agreement to literature [136, 135]. The phase purity was also confirmed by BSE imaging (not shown).

5.2.2 Magnetic and thermomagnetic properties

The spontaneous magnetization, M_s, determined from Arrot-Belov plots as described in the previous chapter is plotted versus temperature in Figure 5.3. The data is determined from the easy-axis of magnetization curves. The continuous line is a fit to Equation 4.1. The fitting parameters are s = 0.33 and p = 4 which are typical for a ferromagnet. M_s at 0 K is extrapolated to 68 $\mathrm{Am^2kg^{-1}}$ which refers to 0.72 μ_B per Co atom in the unity cell with a Curie temperature T_C of 420 K being in good agreement to previous works [145, 146, 147, 148, 149].

The anisotropy energy E_a was determined as the area between the magnetization curves along the [100] and [001] directions recorded at the same temperature as shown in Figure 5.6c). No demagnetization correction was necessary since the sample dimensions in both directions are identical. The so obtained E_a is presented as a function of temperature in Figure 5.3b). One can observe that Iga's values of E_a [147] are noticeably lower than the ones obtained here. The brevity of Iga's paper prohibits a any definite statement about the source of this underestimation. Iga's values of E_a were deduced from torque curves taken in a field of 1.6 T, which is just above the anisotropy field at low temperatures. In an oblique orientation, such a field is insufficient for making the magnetization vector parallel to the applied field. The remaining misalignment distorts the torque curves and has to be corrected for. Unfortunately, there is no mentioning of such a correction [147]. It can be concluded that Co_2B is more strongly anisotropic

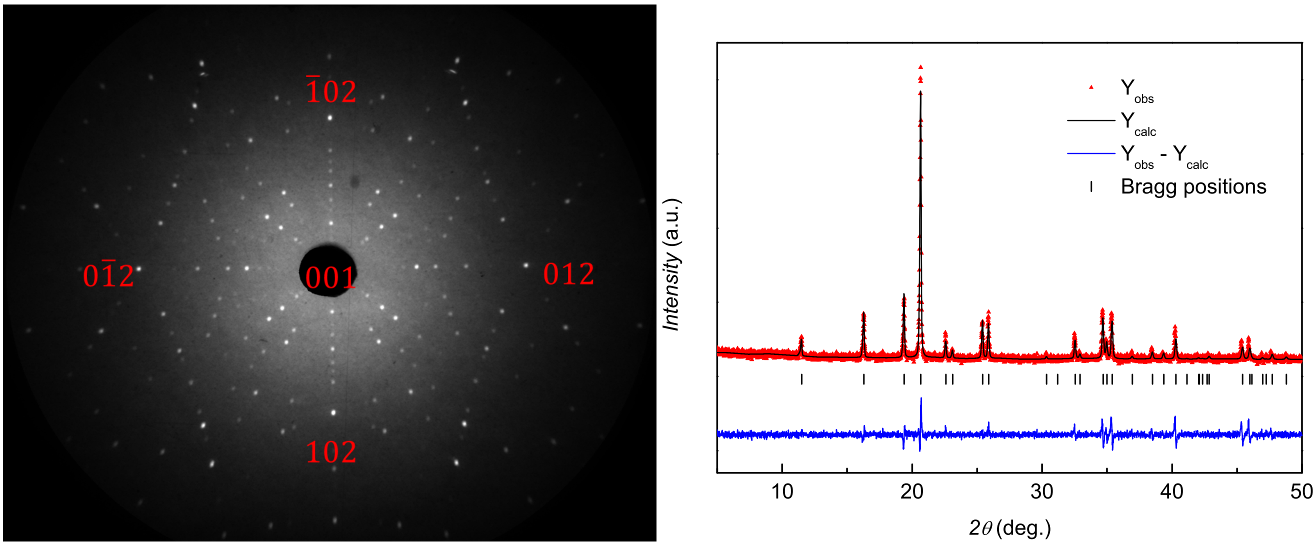

(a) **(b)**

Figure 5.2: a) Laue XRD pattern of a Co2B single crystal with the c-axis oriented perpendicular to the image area. b) Room temperature XRD pattern of Co_2B with corresponding Rietveld analysis.

than previously reported. Indications of this behavior can also be found in [137], where the applied field was 3 T and values comparable to the present work can be found.

The Co_2B compound has an uniaxial magnetic anisotropy at low temperature (magnetic moment is parallel to the [001] axis), however, at T_{srt} of 78 K a spin reorientation transition occurs, as can be seen in Figure 5.3. As a result at T_{srt} the Co_2B single crystal turns magnetically isotropic and above this temperature, till the Curie temperature, the magnetization vector lies in the (001) plane (easy-plane anisotropy). Similar values were obtained by Kadomatsu *et al.* [137]. Other values of the spin reorientation at a lower temperature were determined in [150] on polycrystalline samples of Co_2B.

5.3 Influence of magnetocrystalline anisotropy on the magnetocaloric effect

Most studies on magnetocaloric compounds have been conducted using isotropic polycrystalline samples considering only the conventional magnetocaloric effect, peaking at the Curie temperature. This can be explained by the fact that most magnetocaloric compounds are magnetically soft and are of cubic crystal structure [36, 20]. Accordingly the anisotropic contribution at the Curie temperature is non existent.

Yet it has been found that especially the Fe_2P-type materials which are industrially viable [31] show large magnetocrystalline anisotropy [151] which could strongly influences the magnetocaloric properties [152]. In order to build an efficient cooling device the magnetocaloric effect, namely the adiabatic temperature change ΔT_{ad} and isothermal entropy change ΔS_t need to be maximized within the limitations of the available field source. Therefore the effect of anisotropy is not only of theoretical importance but also of practical significance when designing a heat exchanger made of a magnetocaloric material. Till now detailed experimental studies on the effect of anisotropy on the magnetocaloric effect do not

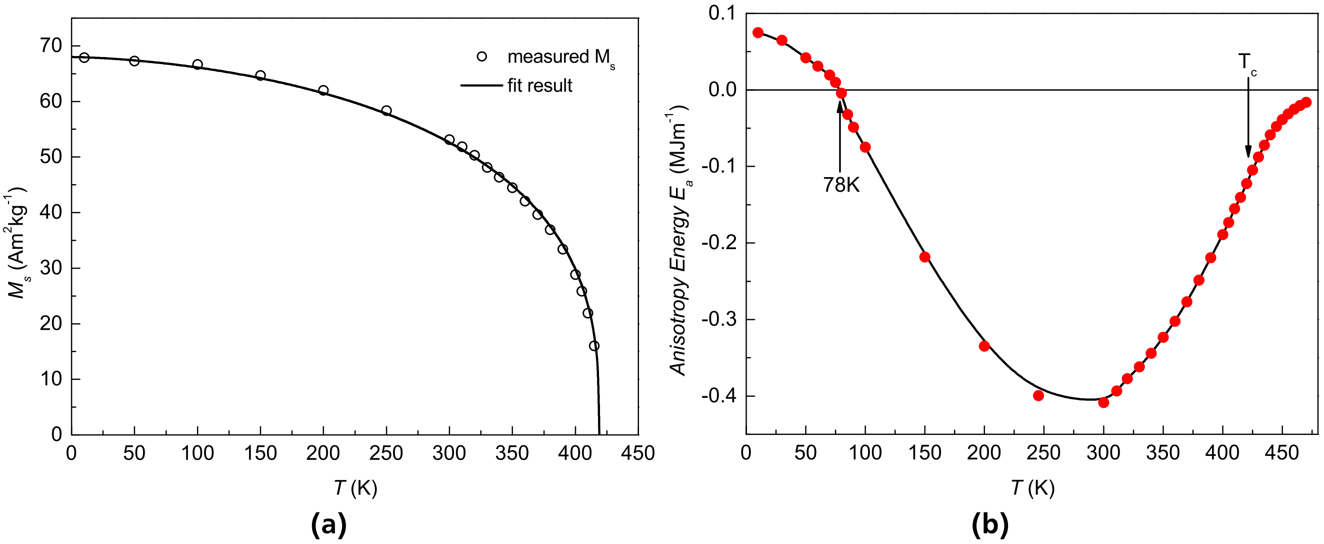

Figure 5.3: a) Spontaneous magnetization M_s versus temperature obtained from Arrot-Belov plots. The continuous line is a fit to equation 4.1. b) Magnetocrystalline anisotropy energy versus temperature, showing a spin reorientation at 78 K calculated with a field change of $\mu_0\Delta H$ = 4 T.

exist because the analysis of anisotropic effects is generally hindered by the lack of single crystal data on magnetocaloric materials.

The anisotropy of the magnetocaloric effect (MCE) has already been discovered several decades ago. Vonsovskiy theoretically predicted a difference in heat capacity at a different magnetic field orientation for a cobalt single crystal in 1938 [153]. In the work of Akulov and Kirensky from 1940 [154] the rotational MCE was directly measured on a nickel single crystal. According to these works, the anisotropic effect in pure 3d metals is below 0.1 KT^{-1} due to low values of their magnetocrystalline anisotropy. However, it was found that the MCE in single crystals of rare earth (RE) metals can be strongly anisotropic, with a different sign of MCE when applying a field along easy and hard axes of a single crystal [155, 156].

According to recent studies conducted on single crystals, the magnitude and shape of the magnetic entropy change can be significantly different when the external field is applied along different crystallographic directions [157, 158, 159, 160, 161, 162, 163, 164, 165]. However, the temperatures at which this effect was observed are far below room temperature.

The previously discussed single crystal of Co_2B was used as a model system as this system offers a well-defined determination of magnetocrystalline anisotropy.

The adiabatic temperature change ΔT_{ad} measured in a field change of 1.93 T in the setup described in chapter 3.2.5 is shown in Figure 5.4. The maximum adiabatic temperature change for an external field applied along the hard axis [100] is 0.65 K at a temperature of 425 K. This is around 40 % lower than that compared for applying the field in the easy plane (100) which is 0.90 K. The polycrystalline measurements are in between the values obtained for applying a field along easy plane and hard direction

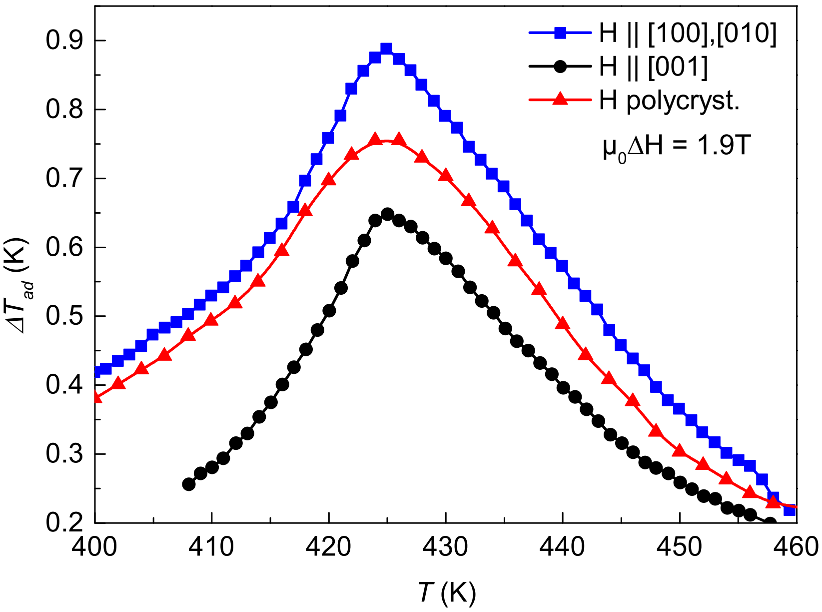

Figure 5.4: ΔT_{ad} versus T in field changes of 1.9 T measured along [100],[010] and [001] directions shown in blue squares and black dots. Measurements performed on a polycrystalline samples are shown with red triangles.

of magnetization. A maximum adiabatic temperature change of 0.75 K is observed for the polycrystalline sample. In all cases the peak ΔT_{ad} takes place at the same temperature of 425 K.

Figure 5.5a) shows $\Delta S_t(T)$ for a field change of 2 T calculated from Maxwell equation (Equation 3.10) exhibiting a similar shape and peak temperature for both polycrystalline and single crystal samples. The field dependence of maximum entropy change ΔS_t values at a constant temperature of 420 K are shown in Figure 5.5b). As in the ΔT_{ad} measurements, an anisotropic behavior is observed in the field dependent $\Delta S_{t,max}$ measurements. Even in fields up to 4 T (much higher than the anisotropy field of approximately 2 T) the entropy changes do not converge and the effect of anisotropy cannot be overcome.

As in the case of the adiabatic temperature change measurements, the values of the polycrystalline sample are between the ones of the single crystal with fields applied in easy plane and hard axis. Both above described effects of ΔT_{ad} and ΔS_t that occur in the polycrystalline samples can be explained by an arbitrary grain orientation leading to values lying in between the values obtained for field alignment along easy plane and hard axis of magnetization, respectively.

In order to quantitatively study the physical origin of this effect, the temperature dependence of anisotropy energy E_a is calculated in different field changes up to 4 T in a temperature range between 360 K and 470 K. The results are shown in Figure 5.6a). E_a is determined by subtracting the integration of $M(H)$ at constant T for different fields applied parallel to the [100] axis and (100) plane as previously described. E_a is sketched as the filled area in Figure 5.6c).

The values of magnetocrystalline anisotropy are rather low compared to other hard magnetic materials [139] yet two things are rather peculiar: first, E_a is still existent above T_C and second, E_a does not saturate with fields above the anisotropy field. This is obvious when looking at the recorded $M(H)$ curves

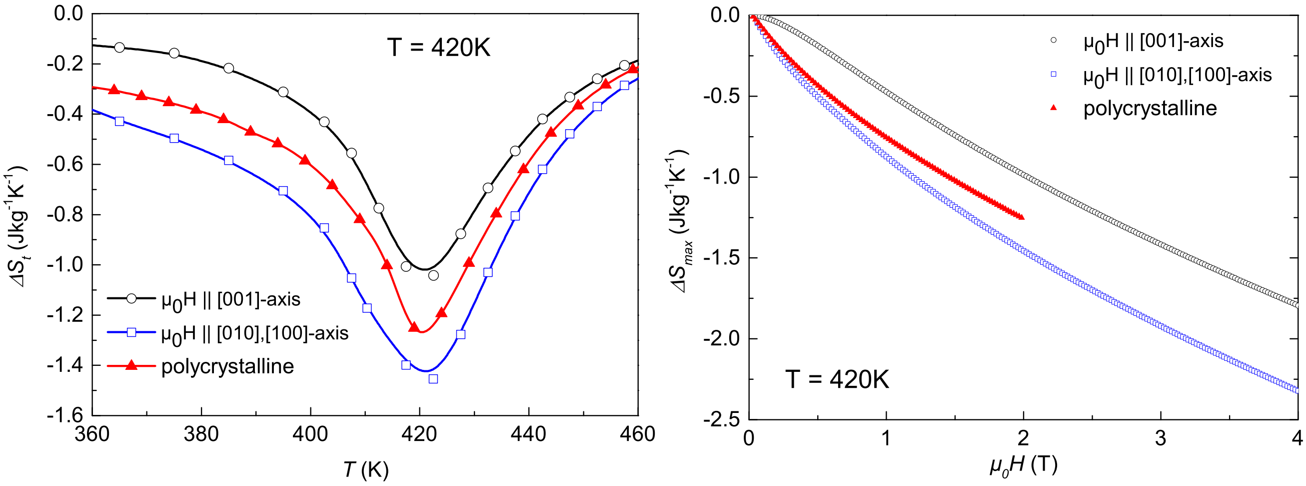

(a) **(b)**

Figure 5.5: a) Temperature dependence of ΔS_t in a field change of 2 T and b) Field dependence of ΔS_{max} for fields applied parallel to [100], [001] axis and to a polycrystalline sample.

in Figure 5.6c) where the magnetization versus field is plotted for the temperatures of 300 K and 422 K (2 K above T_C). It can be seen clearly that M does not fully saturate, making the integral non-converging. Furthermore, anisotropy energy (marked by the hatched area) is still existent above T_C defying Zener's theory of temperature dependence of anisotropy [21]. This phenomenon becomes even more obvious when looking at Figure 5.6b) where the field dependence of E_a is plotted at temperatures above and below T_C. Above the Curie temperature of 420 K E_a is still increasing almost linearly with the applied field.

The effect of magnetization anisotropy was predicted by Callen and Callen [166, 167] and described as an alignment of magnetic moments within a narrow cone along the easy axis of magnetization and an alignment along a wider cone in hard direction. This effect directly also correlates to a difference in paramagnetic susceptibilities.

To estimate the contribution of anisotropy energy on the magnitude of the anisotropic MCE the rotational magnetocaloric effect was calculated. As proposed by Nikitin *et al.* in [160] the rotational entropy change ΔS_{rot} under adiabatic conditions can be calculated by the following expression:

$$\Delta S_{rot} = -\left[\left(\frac{\delta E_{a,H}}{\delta T}\right) - \left(\frac{\delta E_{a,0}}{\delta T}\right)\right] = -\left(\frac{\delta \Delta E_a}{\delta T}\right), \tag{5.1}$$

where $E_{a,H}$ and $E_{a,0}$ are the magnetocrystalline anisotropy energy in the field H and in the zero magnetic field, respectively. The results of the ΔS_{rot} calculations obtained by equation 5.1 are shown in Figure 5.7. A peak in the rotational entropy change is found at T_C, coinciding with the measurements shown in Figure 5.5. In fields above 1 T the magnitude of the rotational MCE saturates. This is due to the fact that the differences in field dependent anisotropy energy are mostly only influenced by the anisotropic saturation magnetization, as can be seen in Figure 5.6.

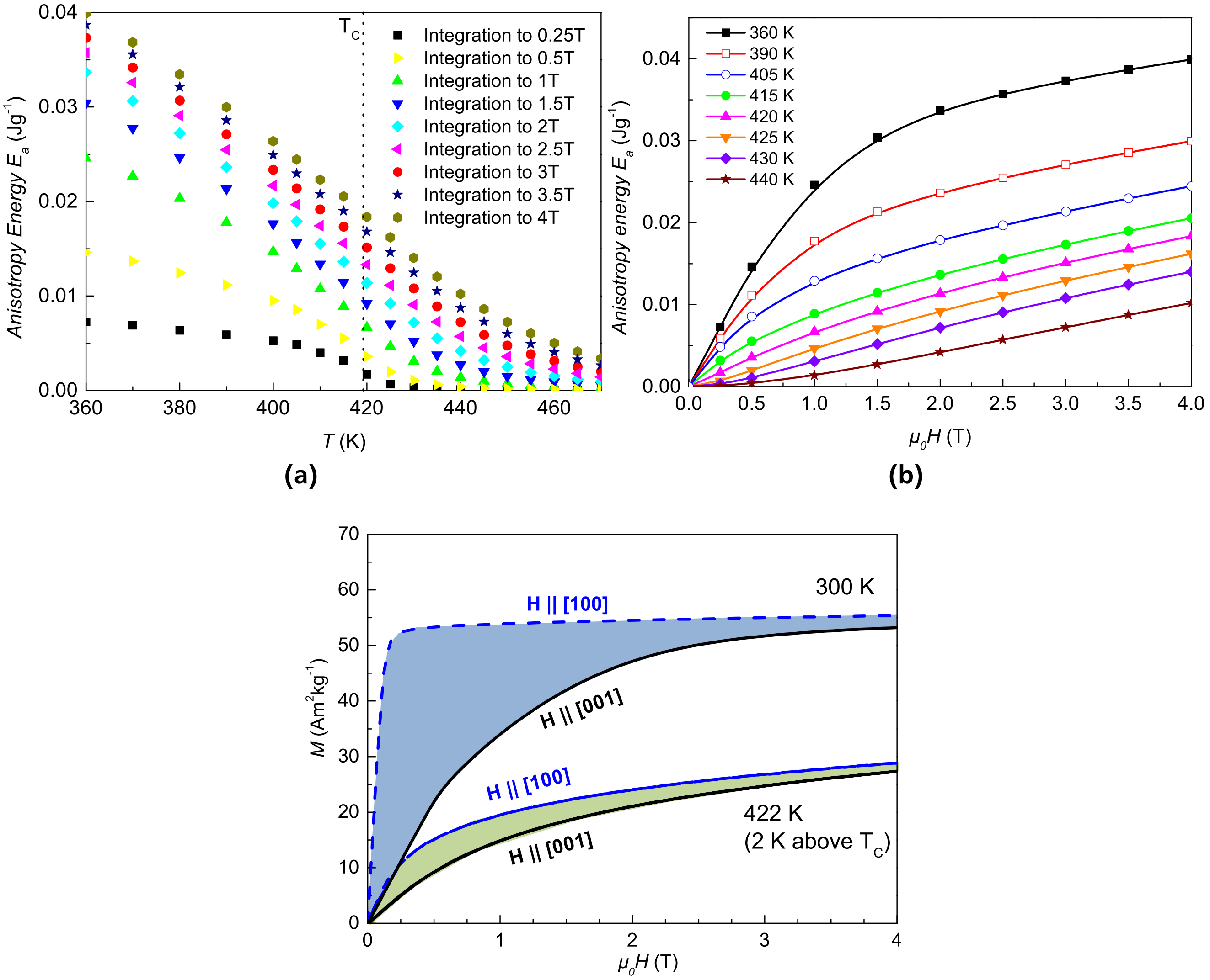

(a) **(b)**

(c)

Figure 5.6: a) Anisotropy energy (E_a) vs temperature for fields ranging from $0.25\,\mathrm{T}$ to $4\,\mathrm{T}$ for the Co_2B single crystal. b) Field dependence of E_a at different temperatures below and above T_C and c) Field dependence of magnetization at two distinct temperatures, below and above T_C. The hatched area indicates E_a.

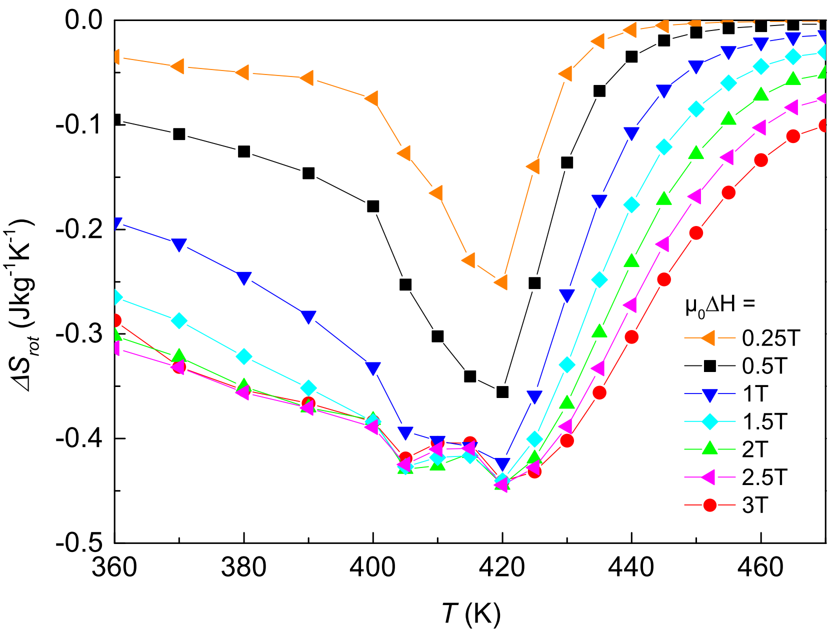

Figure 5.7: Rotational entropy change ΔS_{rot} of Co_2B versus temperature plotted for different fields.

Figure 5.8a) shows the maximum values of ΔS_{rot} at a constant temperature of 420 K (at T_C). Additionally the differences in entropy changes between the easy plane (100) and hard axis [001] calculated by Maxwell equation ($\Delta S_{max,001} - \Delta S_{max,100}$) are shown which are directly correlated to the anisotropic magnetocaloric effect. The field dependence of entropy changes values obtained by both methods are similar, suggesting that the effect of the anisotropic magnetocaloric effect in the studied material system is due the anisotropy energy of the system.

Figure 5.8b) shows a factor that is defined as the anisotropy factor $\eta_{anisotropy}$, describing the potential loss of the magnetocaloric effect due to magnetocrystalline anisotropy. $\eta_{anisotropy}$ is defined as:

$$\begin{aligned} \eta_{anisotropy} &= \frac{(\Delta S_{max,easy} - \Delta S_{max,hard})}{\Delta S_{max,easy}} \\ &= \frac{(\Delta S_{max,[001]} - \Delta S_{max,(100)})}{\Delta S_{max,[001]}}. \end{aligned} \tag{5.2}$$

The dotted lines in the inset of Figure 5.8 indicate a potential loss in entropy change of 50 % in a field change of 1 T and 35 % in 1.9 T. The difference in entropy changes between applying a field in easy plane and hard axis of magnetization is less pronounced than in the case of adiabatic temperature changes. (see Figure 5.4).

The field dependence of the anisotropy factor follows an exponential phenomenological decay law with:

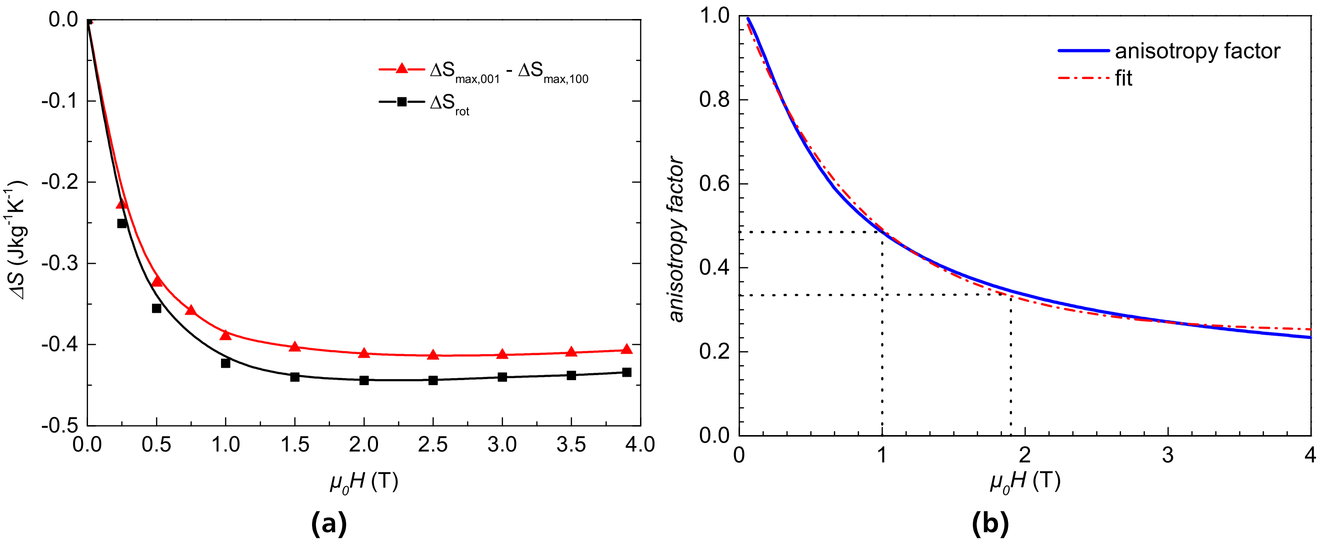

Figure 5.8: a) The maximum values of ΔS_{rot} at constant temperature (black squares) and the difference of maximum entropy changes in easy and hard directions (red triangles). b) Field dependence of the anisotropy factor described in equation 5.2 with corresponding exponential fit.

$$\eta_{anisotropy}(H) = 0.25 + 0.79 \exp\left(\frac{-H}{0.86}\right),$$

suggesting a large influence of magnetocrystalline anisotropy energy especially in low fields below 1 T. This finding is of special importance as this field range is aimed for a real household refrigeration scenario as the permanent magnet setup will play the greatest role in price and eco-friendliness as described in [168]. The findings show that the magnetocaloric effect will be underestimated in measurements of MCE on polycrystalline materials exhibiting magnetocrystalline anisotropy. Even more important, it shows that special care needs to be taken when producing heat exchangers for active magnetocaloric regenerators comprised of non-cubic magnetocaloric materials like for example polymer bonded plates as shown in [52]. In order to maximize the magnetocaloric effect by using the magnetic field source as efficiently as possible the particles should be aligned parallel to the applied magnetic field with respect to their easy axis of magnetization.

In conclusion, the majority of studies of the magnetocaloric effect (MCE) near T_C are performed by using isotropic polycrystalline samples where the contribution coming from magnetocrystalline anisotropy is averaged out. Whereas, in the case of cubic symmetry the use of polycrystalline samples is justified, it was shown that in the case of non-cubic magnetic materials the magnetic anisotropy near T_C is important. MCE measurements on polycrystalline samples lead to underestimation of ΔT_{ad} and ΔS_t. Especially in the target scenario of utilizing materials in small magnetic fields (e.g. 1 to 2 T) the effect of anisotropy is of great importance. Furthermore, due to the nature of ΔS_t, the effect of anisotropy cannot be overcome even in high fields available in the laboratory. Utilizing textured non-cubic magnetocaloric materials with easy axis of magnetization parallel to the applied field is therefore recommended in a real magnetocaloric working device to increase overall efficiency.

5.4 Properties of $Co_{2-x}Mn_xB$

Next the structural properties of the system $Co_{2-x}Mn_xB$ will be discussed. Co was gradually replaced by Mn up to a content of x=0.8.

5.4.1 Structural properties

Room temperature XRD diffraction patterns of $Co_{2-x}Mn_xB$ are displayed in Figure 5.9. All samples have crystallized in the same tetragonal crystal structure as the Co_2B base compound. It is assumed that the Mn atoms randomly occupy the 8h sites of the crystal lattice (see Figure 5.1), gradually replacing the Co atoms. All compounds of this series show no signs of secondary phases both in the XRD analysis and the corresponding BSE images. The ratio between Co and Mn was determined by means of EDX. The discrepancies between the nominal compositions and the values measured are in error margins of the device (less than 3 at.%). The system is fully mixable as previously shown in [136, 137, 138]. The results of the Rietveld refinement are shown in Figure 5.10. In Figure 5.10a) an increase in lattice parameter a can be observed from $a = 5.006\,\text{Å}$ in pure Co_2B to $a = 5.088\,\text{Å}$ in $Co_{1.2}Mn_{0.8}B$. This behavior is consistent with Vegard's law as the atomic radius of Mn is larger than that of Co. This also becomes obvious when looking at the (110) reflection plotted in the inset of Figure 5.9. The reflex of the (110) lattice plane is shifted to higher angles implying a decrease of the $a = b$ lattice parameter. Whereas the c lattice parameter only slightly increases with Mn substitution as also displayed in Figure 5.10a) leading to an anisotropic expansion of the unit cell. The unit cell volume and XRD density are shown in Figure 5.10b). The total unit cell volume is increased from $21.09\,\text{Å}^3$ in pure Co_2B to $21.53\,\text{Å}^3$ in $Co_{1.2}Mn_{0.8}B$ with a drop in density of $8.09\,\text{gcm}^{-3}$ to $7.80\,\text{gcm}^{-3}$, respectively. The behavior is in good agreement with literature [136, 169, 170].

5.4.2 Magnetic and thermomagnetic properties

$M(T)$-curves measured in a field of 1 T for $Co_{2-x}Mn_xB$ are illustrated in Figure 5.11a). In a field of 1 T all materials have reached magnetic saturation as confirmed by $M(H)_T$ measurements. A complex behavior is visible when looking at the magnetization values at 100 K. $Co_{1.9}Mn_{0.1}B$ has a magnetization of $64\,\text{Am}^2\text{kg}^{-1}$, while the magnetization is rising to $70\,\text{Am}^2\text{kg}^{-1}$ for $Co_{1.8}Mn_{0.2}B$. A maximum of magnetization of $102\,\text{Am}^2\text{kg}^{-1}$ is reached for $Co_{1.7}Mn_{0.3}B$ and $Co_{1.6}Mn_{0.4}B$. By further increasing the Mn concentration magnetization values continuously drop and reach a value of $58\,\text{Am}^2\text{kg}^{-1}$ in $Co_{1.2}Mn_{0.8}B$. These observations are consistent with previous measurements shown in [136, 138]. As mentioned before it is expected that by doping of Mn in $Co_{2-x}Mn_xB$ the Co atoms in the unit cell are replaced by Mn atoms. When the Co atoms are replaced with a small amount of Mn the average magnetic moment

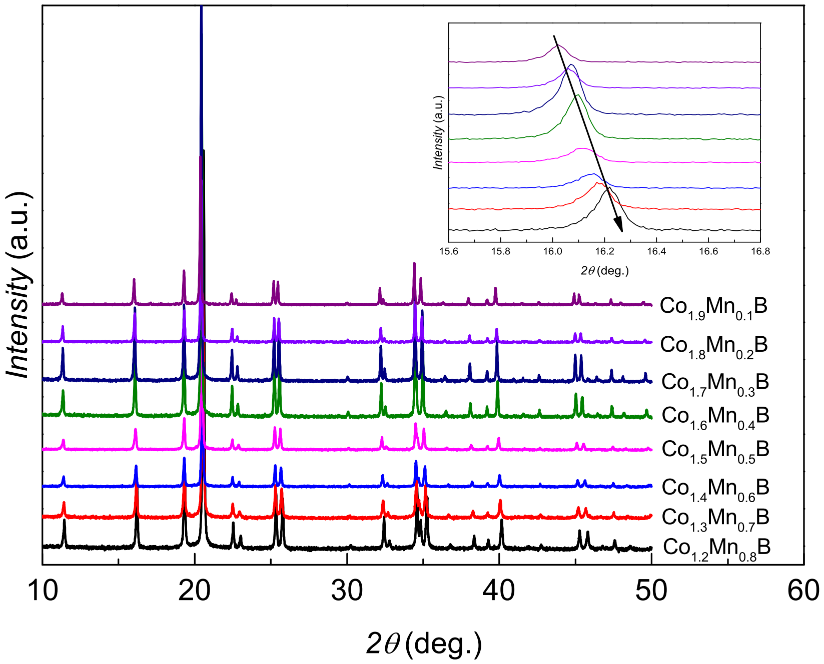

Figure 5.9: Room temperature XRD paterns for the compounds $Co_{2-x}Mn_xB$ with varying Mn content. The inset shows the shift of the (110) reflection to lower angles with increasing Mn content.

increases since the magnetic moment of Mn is larger than that of Co. When increasing the Mn concentration the probability rises that a Co or Mn atom will be surrounded by more Mn atoms. Apparently, the center atoms (Co or Mn) atoms lose their magnetic moment or couple antiferromagnetically with the neighbor atoms when the number of Mn atoms reaches a critical value. At a Mn concentration of x = 0.3 and 0.4 seemingly the highest amount of ferromagnetic coupling between Co and Mn is realized in this system. From then on non-magnetic or antiferromagnetic coupling of the Mn atoms will lower the overall magnetization. Therefore, one can come to the conclusion that the coupling of Co-Co and Co-Mn atoms is ferromagnetic and the coupling of Mn-Mn is non-magnetic or antiferromagnetic. Similar observations were also made for the system Ni-Mn, where the coupling between Ni-Ni and Ni-Mn is ferromagnetic and the coupling of Mn-Mn is antiferromagnetic [171]. However, in the system Co-Mn the coupling of Co-Co is ferromagnetic and the Mn-Co and Mn-Mn coupling is antiferromagnetic [172]. Preliminary results from DFT calculations (Ingo Opahle and Eszter Simon, both TU Darmstadt) suggest that the Mn-Mn coupling is of non-magnetic nature in the whole compositional range. A non-magnetic coupling of Mn is also confirmed in the compound Mn_2B [173].

The ferromagnetic and paramagnetic Curie temperatures for the system $Co_{2-x}Mn_xB$ are plotted in Figure 5.11b). The ferromagnetic Curie temperature were obtained by Arrot-Belov plots from $M(H)_T$ curves in field of 0 to 2 T. The paramagnetic Curie temperature were obtained by fitting the Curie-Weiss law to the susceptibility in a field of 1 T. As mentioned before, pure Co_2B has a T_C of 420 K. The ferromagnetic and paramagnetic Curie temperatures overlap perfectly. The Curie temperature reaches its maximum at $Co_{1.9}Mn_{0.1}B$ and $Co_{1.8}Mn_{0.2}B$ with a T_C of 449 K. The paramagnetic T_C is slightly higher for $Co_{1.8}Mn_{0.2}B$ than the ferromagnetic T_C. From $Co_{1.8}Mn_{0.2}B$ to $Co_{1.2}Mn_{0.8}B$ T_C drops continuously to 249 K for the ferromagnetic T_C and 278 K for the paramagnetic T_C. The behavior of the ferromagnetic Curie temper-

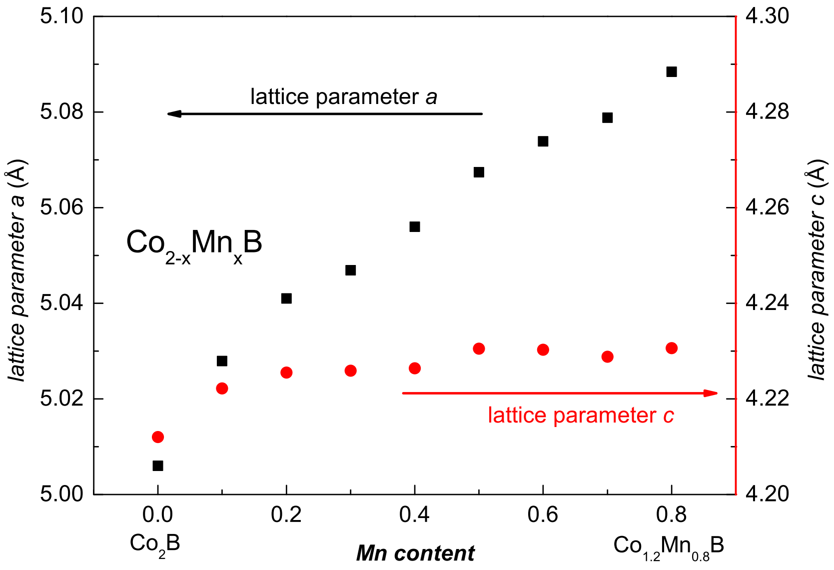

(a) lattice parameter a and c

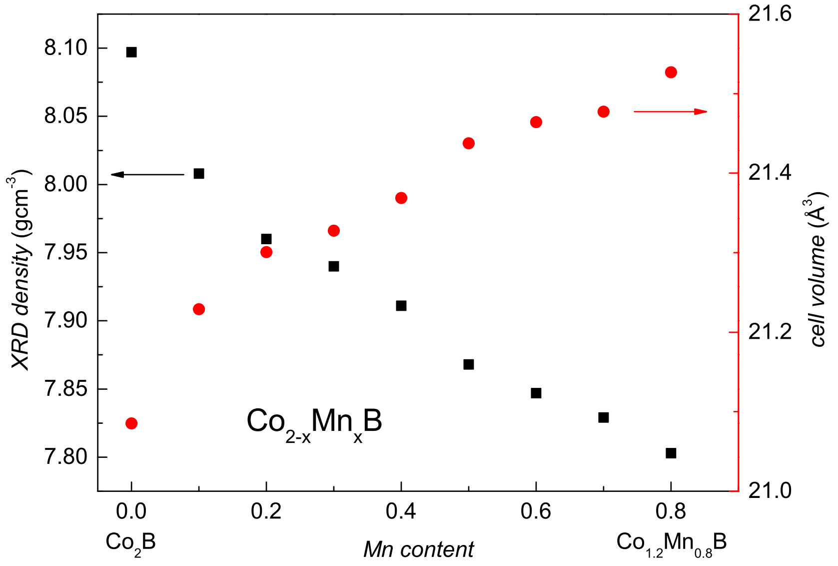

(b) XRD density and cell volume

Figure 5.10: Room temperature lattice parameters a and c shown in a) for the compounds $Co_{2-x}Mn_xB$ in the range of x=0-0.8 and the corresponding XRD density and cell volume in b).

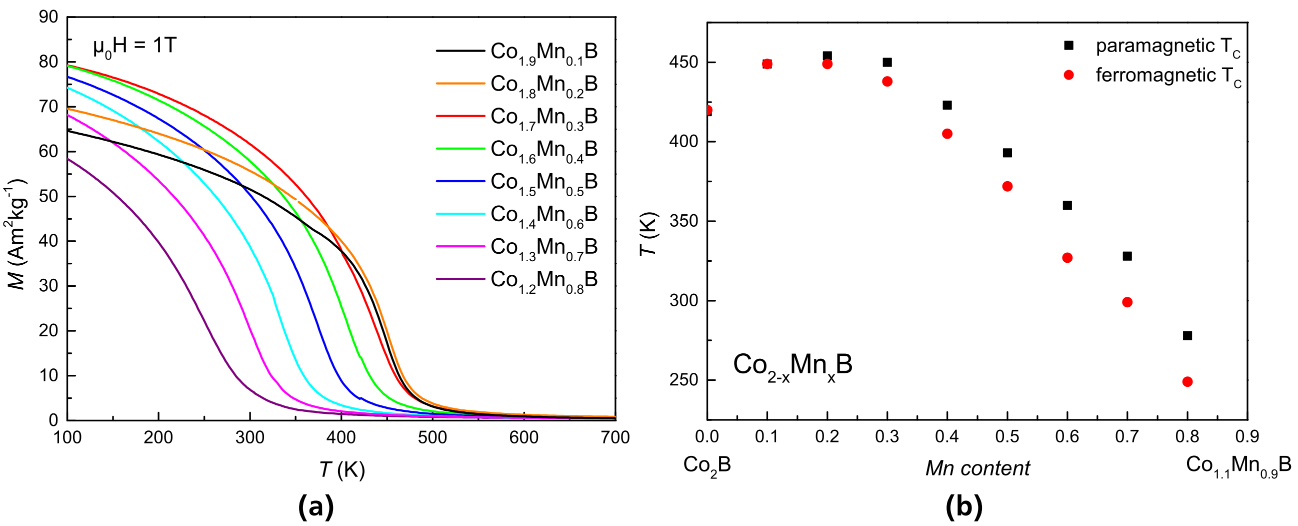

Figure 5.11: a) Magnetization versus temperature curves of the compound $Co_{2-x}Mn_xB$ measured in a field of $\mu_0 H = 1\,T$. b) Paramagnetic and ferromagnetic Curie temperatures of the compound $Co_{2-x}Mn_xB$ in dependence of the Mn content.

ature was previously confirmed as well in polycrystalline as in amorphous materials [138]. The rising deviation of the ferromagnetic and paramagnetic Curie temperatures also yields the previous assumption that the coupling in the system becomes more non-magnetic or antiferromagnetically with rising Mn concentration as in a purely ferromagnetic system both Curie temperatures should overlap [21].

In order to prove this statement of the magnetic coupling in $Co_{2-x}Mn_xB$ more experiments will be necessary like for example neutron diffraction, coupled with DFT calculations explaining the complex behavior of doping in this system.

To judge the magnetocaloric applicability of this system ΔS_t curves of the system $Co_{2-x}Mn_xB$ in a field change of 2 T are shown in Figure 5.12. The calculation of the entropy changes was performed by using the numerical Maxwell equation 3.10 from $M(H)_T$ curves. This procedure was chosen as no indication of a first-order phase transition was visible from $M(T)$ curves shown in Figure 5.11. $Co_{1.9}Mn_{0.1}B$ has the highest magnetic entropy change of $1.37\,Jkg^{-1}K^{-1}$ at 449 K lowered to $1.19\,Jkg^{-1}K^{-1}$ in $Co_{1.8}Mn_{0.2}B$ at the same temperature. The magnetic entropy change continuously decreases with increasing Mn-content and lower transition temperature. The compound $Co_{1.3}Mn_{0.7}B$ has a transition around room temperature at 295 K with an entropy change of $1.05\,Jkg^{-1}K^{-1}$.

To conclude, the transition temperature in the system $Co_{2-x}Mn_xB$ is tunable in a large temperature range, yet the magnetocaloric effect is rather small compared to other materials and not enough heat could be pumped with these materials. Additionally the density is reduced when doping Mn into the system accounting for an even lower volumetric entropy change. When taking into account the high price and criticality of Co the material is neither interesting for magnetocaloric cooling nor thermomagnetic power generation applications.

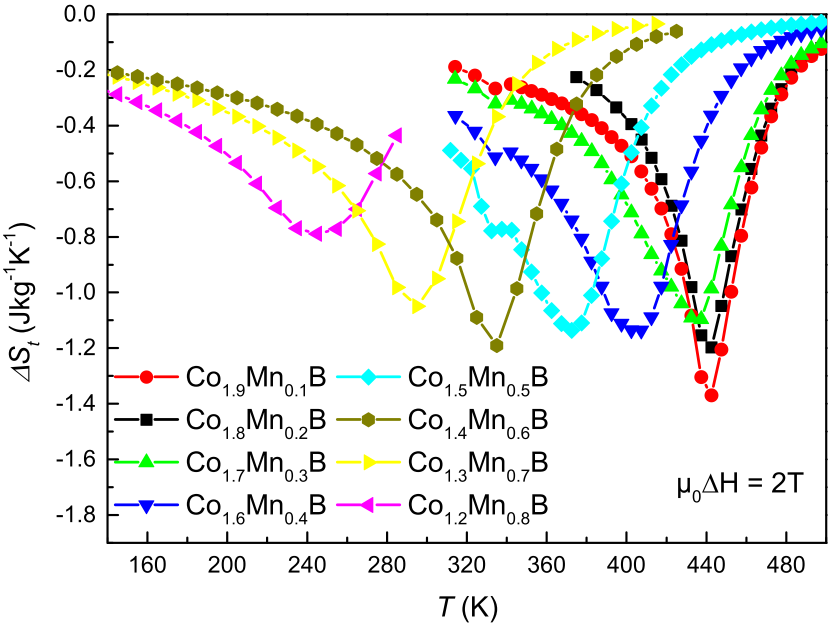

Figure 5.12: Isothermal entropy changes for the compounds $Co_{2-x}Mn_xB$ calculated from $M(H)_T$ curves in a field change of $\mu_0\Delta H = 2\,\mathrm{T}$.

A complex coupling behavior is present for doping Mn into the system influencing the magnetic exchange interaction drastically which is not fully clarified at the moment but will be explored in the future by more detailed DFT calculations.

6 Properties of Mn-Fe-P-Si Fe_2P-based magnetocaloric compounds

Fe_2P-type alloys are class of very promising rare-earth-free magnetocaloric materials. The family is derived from the prototypical Fe_2P-based compound, showing a sharp first-order phase transition at T_t = 217 K [174, 175]. In 2002, the compound $MnFeP_{0.4}As_{0.55}$ was reported by Tegus *et al*. [56] to exhibit a giant MCE near room temperature at which the structural and magnetic transformations coincide. Besides the large thermal hysteresis, the other drawback of this type of alloy is the content of toxic arsenic, which limits its use in a domestic refrigeration appliance. Since the discovery of this alloy, large efforts have been focused on tuning the transition and especially on the substitution of critical elements in this system. The As could be completely replaced by Si, while conserving the magnetocaloric properties. Furthermore, the transition temperature is highly tuneable by adjusting the Mn and Si content [176]. In this material class, the first-order transition also manifests itself in a large volume change of the hexagonal structure. Conventionally, the desired phase is prepared by ball milling of precursor powders, compaction and a subsequent heat treatment procedure for sintering [176] or by melt spinning [177].

Studies in the class of Mn-Fe-P-Si-type alloys have shown that the hysteresis could be minimized by fine adjustment of the Mn/Fe and P/Si ratio. The drawback of this adjustment is the decrease in overall magnetization and therefore, a decrease in ΔM at the transition. In order to increase both values, one has to work at the optimum composition of $MnFeP_{0.66}Si_{0.33}$ [178, 179]. This composition has a low value of ΔT_{ad} ($\approx$ 2 K in 1 T), but, at the same time, shows a rather high value of $\Delta S_t = -8\,\mathrm{Jkg^{-1}K^{-1}}$ [180]. A major disadvantage of these compounds is their mechanical instability. The instability is considered to be from the volume change of +0.2% [178] when crossing the transition temperature leading to embrittlement of the bulk samples.

Recently, the above-mentioned issues were tackled by applying internal pressure to the compound by adding boron to the system [59]. For the compound $MnFe_{0.95}P_{0.595}B_{0.075}Si_{0.33}$, a cyclic adiabatic temperature change of $\Delta T_{ad} = 2.55$ K with a cyclic $\Delta S_m = -10\,\mathrm{Jkg^{-1}K^{-1}}$ in a field change of 1 T with a thermal hysteresis of 1.6 K was observed. This enhancement of properties is ascribed to the larger field dependence of T_t and lower latent heat of this material compared to Mn-Fe-P-Si. Furthermore, the mechanical integrity of this compound was reported to be optimized to a point where no breaking or cracking of the samples could be observed, even after 10 000 cycles of magnetization and demagnetization [181]. This improvement in the structural integrity was ascribed to the fact that there is no discontinuous volume change present when passing through the transition but a comparable change in the a/c lattice parameters of the base Mn-Fe-P-Si compound is preserved. It was also shown that the B-containing compounds $Mn_xFe_{1.95-x}P_{1-y-z}Si_zB_y$ are highly tuneable while preserving the giant MCE with a limited thermal hysteresis in a broad temperature range [182]. Very recent works show that boron can also be substituted by nitrogen, possibly increasing the industrial applicability of this compound [183].

In summary, the compounds of Mn-Fe-P-Si-B/N are, as the La(Fe,Mn,Si)$_{13}$H$_x$-type alloys, a highly promising class of materials for magnetic refrigeration due to their precisely tuneable transition temperatures with low hysteresis and high reversible values of ΔS_t and ΔT_{ad} at low fields applicable in a refrigeration device. Furthermore, they also consist of cheap, non-toxic and readily available elements [184].

The results shown in this chapter are partly published in the following journals:

- O. Gutfleisch, T. Gottschall, M. Fries, D. Benke, I. Radulov, K. P. Skokov, H. Wende, M. Gruner, M. Acet, P. Entel and M. Farle, Mastering hysteresis in magnetocaloric materials, Philosophical Transactions A **374** (2016) 20150308.
- M. Fries, L. Pfeuffer, E. Bruder, T. Gottschall, S. Ener, L. V. B. Diop, T. Gröb, K. P. Skokov and O. Gutfleisch, Microstructural and magnetic properties of Mn-Fe-P-Si (Fe$_2$P-type) magnetocaloric compounds, Acta Materialia **132** (2017) 222.
- T. Gottschall, D. Benke, **M. Fries**, A. Taubel, I. A. Radulov, K. P. Skokov and O. Gutfleisch, A matter of size and stress: Understanding the first-order transition of materials for solid-state refrigeration, Advanced Functional Materials **27** (2017) 1606735.

6.1 Experimental approach

Samples with Fe_2P-type structure were produced by a powder metallurgical route followed by an annealing step. Powders with a purity of 99.9% of Mn, Fe_2P, Si and P (total amount 5 g) were mixed in inert atmosphere. In order to compensate evaporation losses, additional P was added to the stochiometric weighed elements. Milling was performed in a Spex 8000 D high-energy ball mill at 875 cycles/min in a hardened steel vial with 2 hardened steel balls and a ball to powder ratio of 3.34 for 80 min. The ball-milled powder was then uni-axially compacted in a press-form with 0.1 GPa pressure at room temperature using a PW 20 hydraulic press. The green-bodies were then wrapped in Molybdenum foil and sintered in a Gero 7542 vacuum tube furnace under a constant Ar pressure of 1.25 bar for 2 hours at 1373 K followed by a 20 hours annealing step at 1123 K and slow cooling to room temperature. Prior to all measurements, the surface layers of the sample where ground off in order to remove possible surface oxidation. A list of samples discussed in this chapter is given in table 6.1.

A Tescen high resolution scanning electron microscopy (SEM) equipped with an energy-dispersive x-ray (EDX), back-scatter electron (BSE) and electron back-scatter diffraction (EBSD) detector was used for microstructural characterization. The stochiometry of the compounds presented in this article were determined by EDX with an error of less than 3 at%. Prior to all magnetic measurements, the materials were cycled 3 times in liquid nitrogen with subsequent heating to room temperature in order to remove the ”virgin” effect if not mentioned otherwise. Magnetization measurements were performed using commercial vibrating sample magnetometers, Lake Shore 7400 Series and Quantum Design PPMS-14. For the $M(T)$ measurements, a sweeping rate of 2 Kmin^{-1} was used, if not mentioned otherwise. Temperature-dependent optical microscopy was performed on Zeiss Imager D2.m microscope equipped with a LN_2 cryostat from evico magnetics as described in [55].

Direct measurements of the adiabatic temperature change ΔT_{ad} were carried out in two different devices. ”Slow” adiabatic temperature change measurements were performed in a purpose-built device setup described in chapter 6.8.2 with two nested Halbach magnets with a maximum sinusoidal field change of $\mu_0 \Delta H$ of 1.93 T with a starting field change rate of 0.93 Ts^{-1}. For measurements of the adiabatic temperature change a differential T-type thermocouple was glued between a stack of two sample plates and glued together with thermally-conductive epoxy.

Table 6.1: List of samples discussed in this chapter

Sample ID	composition main-phase	composition secondary-phase	wt.% secondary phase	M/NM
Sample 1 (S1)	$Mn_{1.32}Fe_{0.71}P_{0.5}Si_{0.56}$	$Mn_{1.49}Fe_{1.35}Si$	5	1.93
Sample 2 (S2)	$Mn_{1.24}Fe_{0.70}P_{0.5}Si_{0.58}$	-	0	1.80
Sample 3 (S3)	$Mn_{1.19}Fe_{0.68}P_{0.5}Si_{0.57}$	$Mn_{1.32}Fe_{1.21}Si$	3	1.75
Sample 4 (S4)	$Mn_{1.13}Fe_{0.59}P_{0.5}Si_{0.52}$	$Mn_{1.33}Fe_{1.16}Si$	6	1.67
Sample 5 (S5)	$Mn_{1.20}Fe_{0.68}P_{0.5}Si_{0.66}$	-	0	1.62
Sample 6 (S6)	$Mn_{1.22}Fe_{0.59}P_{0.5}Si_{0.59}$	-	0	1.73
Sample 7 (S7)	$Mn_{1.30}Fe_{0.70}P_{0.5}Si_{0.55}$	$Mn_{1.54}Fe_{1.34}Si$	1	1.901

”Fast” ΔT_{ad} measurements were carried out in pulsed magnetic fields up to 20 T at the Dresden High Magnetic Field Laboratory in Dresden-Rossendorf, described in chapter 3.2.5. For all measurements shown, the maximum field is reached within a time frame of 0.13 s leading to a field-sweep rate of up to 2700 Ts^{-1} achieved in a field change of 20 T. A thin differential T-type thermocouple of 25 μm wire thickness was attached similar to the ”slow” measurement in order to detect the temperature change. In order to correct the measurement signal due to an induction into the thermocouple a background signal was recorded at high temperature far away of the phase transition and deducted from all the measurement signals. Earlier measurements on this setup suggest that eddy current heating of the samples is negligible [185, 186, 187].

For all measurements in section 6.8 of the adiabatic temperature change ΔT_{ad} a non-continuous measurements protocol was chosen [55]. The memory of the material was removed after every field application cycle by heating the sample to 300 K being fully paramagnetic and subsequently cooling down to the specific measurement temperature.

6.2 Structural and microstructural characterization

Figure 6.1 shows the room temperature XRD measurement of the $Mn_{1.32}Fe_{0.71}P_{0.5}Si_{0.56}$ sample.

The synthesized $Mn_{1.32}Fe_{0.71}P_{0.5}Si_{0.56}$ sample was found to be mainly single phase according to the x-ray diffraction investigation. The XRD pattern indicates the presence of residual traces of the pseudo-binary cubic Fm$\bar{3}$m compound $(Mn,Fe)_3Si$ with the composition $Mn_{1.49}Fe_{1.35}Si$ as minority impurity phase. The P-62m (#189) space group symmetry for $Mn_{1.32}Fe_{0.71}P_{0.5}Si_{0.56}$ could be confirmed. It is worth recalling that earlier published studies also reported the difficulty to synthesize the pure compound [176, 178]. The refined unit cell parameters for $Mn_{1.32}Fe_{0.71}P_{0.5}Si_{0.56}$ are $a=$ 6.1 Å and $c=$ 3.45 Å, which are in good agreement with previously reported values [188, 178, 189, 190].

The BSE image in Figure 6.2a) shows the porosity of the samples. The black spots in the BSE image correspond to the pores which are occurring during the formation of the Fe_2P-phase from the initial powder mixture and they are remaining during the rest of the production route. This porous structure is inevitable and could not be overcome by comparable powder metallurgical routes that are regularly used as described in literature [190]. Therefore, it is hindering a direct application of the material in bulk-like regenerator structures, like plates or channel structures because of their brittleness due to the high porosity.

The density of the Mn-Fe-P-Si sample was determined to be 5.9 gcm^{-3} (by using the Archimedes principle), which is 7% less than the theoretical density of 6.34 gcm^{-3}. By using the linear intersection method, the surface ratio of the pores was calculated from the BSE image of the Mn-Fe-P-Si sample. The obtained value of 8% is in good agreement with the difference which is obtained from the measured and theoretical densities. This finding shows that the observed density difference is due to the porous structure of the Mn-Fe-P-Si sample. The existence of the secondary $(Mn,Fe)_3Si$ phase was confirmed also by the BSE images (Figure 6.2a)). The secondary phase can be found at the triple junctions in between the Fe_2P

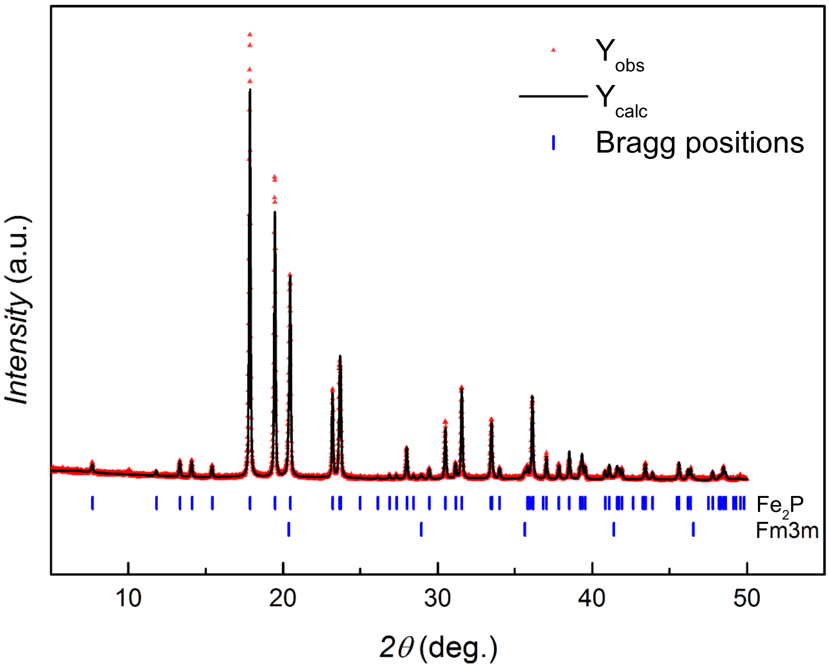

Figure 6.1: Room temperature XRD pattern of $Mn_{1.32}Fe_{0.71}P_{0.5}Si_{0.56}$ crystallized in the Fe_2P structure with a small (<3 wt.%) phase content of $(Fe,Mn)_3Si$ secondary phase.

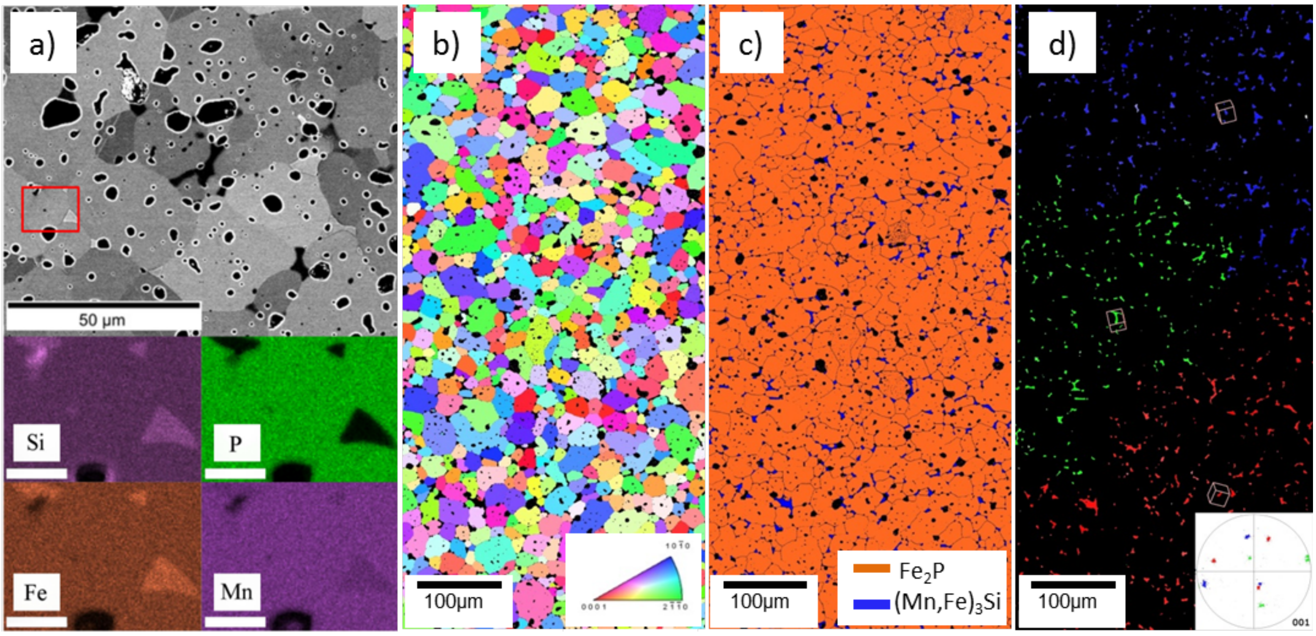

Figure 6.2: a) BSE SEM contrast images of $Mn_{1.32}Fe_{0.71}P_{0.5}Si_{0.56}$ sample. Bottom half of the image depicts the EDX mappings of the corresponding area indicated with the red square. The white bars in a) bottom correspond to the scale bar of 5μm. b) Inverse pole figure map of the main Fe_2P-type phase c) phase map from EBSD measurements d) $(Fe,Mn)_3Si$ phase map with color coding according to insert pole figure.

grains and displays a triangular shape. The phase composition of the main Fe_2P-type phase was identified as $Mn_{1.32}Fe_{0.71}P_{0.5}Si_{0.56}$ by EDX measurements, whereas the nominal composition of the alloy was $Mn_{1.25}Fe_{0.7}P_{0.5}Si_{0.5}$. The bottom pictures in Figure 6.2a) show EDX maps of the selected area indicated by a red square. The secondary phase is rich in Fe and Si with no trace of P within the secondary phase. We derive the composition of a $(FeMn)_3Si$ Heusler-type phase consistent with the XRD measurements (Figure 6.1).

EBSD measurements of the $Mn_{1.32}Fe_{0.71}P_{0.5}Si_{0.56}$ sample are illustrated in Figure 6.2b-d). The inverse pole figure map of Fe_2P in Figure 6.2b) indicates that the BSE image depicted in Figure 6.2a) is representative for the overall sample. The grain size of the Fe_2P phase is following a log-normal distribution with an average of 27 μm. No distinct crystallographic texture or grain elongation for the $Mn_{1.32}Fe_{0.71}P_{0.5}Si_{0.56}$ is observed (see Fig. 6.2b). To illustrate the overall distribution of the pores and secondary phases, phase specific color coding is used in Figure 6.2c). The secondary phase $(FeMn)_3Si$ (shown in purple in Fig. 6.2c) is preferably located at the triple junctions (already shown in Figure 6.2a) in detail) of the Fe_2P-type phase (shown in orange in Fig. 6.2c)) and this behavior is true for the entire sample.

In Figure 6.2d) the $(FeMn)_3Si$ phase with color coding according to the inset pole figure is shown. Three distinct orientation areas of $(FeMn)_3Si$ can be observed. The distinct orientations give an insight into the formation process of the Fe_2P-type phase. Large zones with spatially separated grains sharing the same crystal orientation indicate the presence of a coarse grained single-phase microstructure at elevated temperatures. Similar microstructures can be observed in several materials which undergo a partial phase transformation during cooling and have been studied regarding variant selection. In steels containing retained austenite, prior austenite grains can be identified by the zones showing retained austenite grains with same orientation [191, 192]. Other examples are duplex Ti alloys [193] or FeNi alloys in meteorites [194]. Thus, it is likely that the hexagonal Fe_2P and the cubic $(FeMn)_3Si$ phase evolve from the decomposition of single (presumably cubic) high temperature phase.

6.3 The virgin effect

The virgin effect in magnetocaloric compounds is a long studied phenomenon occurring in many MCE materials with a large magneto-elastic coupling like in the La-Fe-Si family [195], MnAs-type compounds [196], $(Mn,Fe)_2(P,Ge)$ [197, 198] and $(Mn,Fe)_2(P,Si)$ [199, 190, 200, 201]. The effect causes the large discrepancy between the first transformation cycle of a ”fresh” material and all subsequent cycles. A $M(T)$ curve of the virgin $Mn_{1.32}Fe_{0.71}P_{0.5}Si_{0.56}$ is displayed in Figure 6.3. On first cooling, the paramagnetic to ferromagnetic transition occurs at lower temperatures and additionally also the slope of the curve is much steeper than in all following cycles. The initial transition starts at 250 K and the sample transforms more or less in one jump. The first heating branch is already quite similar to the second heating branch and the shape of the curves does not change anymore in all subsequent cycles. The inflection point of the second cooling branch and the transition temperature of the sample on cooling is 268 K. The transition is shifted by approximately 20 K in comparison to the first ”virgin” cooling. The nature of this effect was studied already by means of neutron diffraction [199, 201], stating that a metastable phase

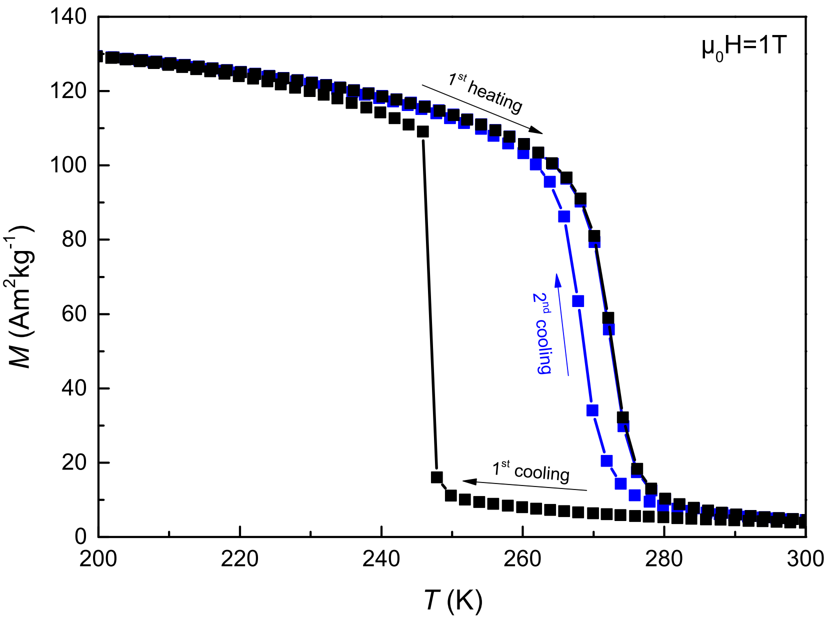

Figure 6.3: Magnetization versus temperature curves measured in a field of 1 T showing the first and subsequent cooling and heating cycles of a Fe_2P sample exhibiting a distinct virgin effect.

is present in the as-prepared state and transforms to a more stable phase after the first phase transition. Bartok *et al.* [190] recently describes the virgin effect as a stress-coupled effect occurring due to the anisotropic volume expansion of the hexagonal Fe_2P-type phase hindering the transformation. They reported a phenomenological relation between particle size, dislocation density and the virgin effect. The analysis was preformed by using Hall-Probe imaging which revealed the presence of cracks after cooling.

In order to in-situ study this phenomena on a macroscopic length-scale, a polished piece of $Mn_{1.32}Fe_{0.71}P_{0.5}Si_{0.56}$ was attached with thermally conductive silver paste to a sample stage that can be cooled by pumping evaporating liquid nitrogen throughout the sample space. The sample was then cooled from room temperature through the virgin transition with a cooling rate of $2\,\mathrm{Kmin}^{-1}$ while observing the process with a light microscope. The results are shown in Figure 6.4. At 249 K, a small crack is observed in the left corner, which corresponds well to the starting temperature of the transition obtained from the $M(T)$ curve shown in Figure 6.3 where a slight increase of magnetization is observed yielding a small fraction of ferromagnetic phase in the sample. On further cooling to 247 K, the cracks propagate through the entire material. The formation of cracks is a non-continuous process occurring in avalanches which is in good agreement with reference [190] where this was observed using DSC and field-dependent magnetization measurements. From reference [190] it can be concluded that only the cracked sample parts are in a ferromagnetic state which agrees well with our magnetization data in Figure 6.3. All materials investigated in this article lost their mechanical integrity after the first cooling cycle and exhibit a ”crippling brittleness” as stated in [151]. The cracking after the first cycle, together with the high possibility hinder a possible direct application of the material in a bulk-like heat exchanger. Heat exchanger structures could be possibly produced by bonding the material in a semi-elastic polymer matrix which can withstand the stresses evolving during the transition, as already shown for the La-Fe-Si family [52, 83].

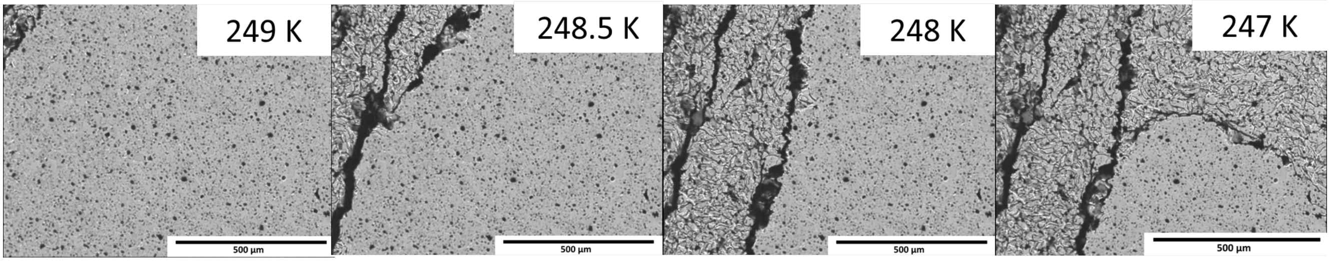

Figure 6.4: Temperature dependent microscopy showing the propagation of cracking of the sample when going through the critical transition temperature.

6.4 Magnetic and magnetocaloric properties

The temperature dependence of magnetization, $M(T)$ is presented in Figure 6.5a) for field heating (FH) and field cooling (FC). The magnetization of 115 $\mathrm{Am^2kg^{-1}}$ at 250 K in a field of 1 T agrees well with literature values of other compounds of the Fe_2P family [178, 190]. The thermal hysteresis in low fields measured at the inflection points of both the heating and cooling curves is about 7 K . While increasing the field up to 10 T, the transition broadens drastically and the thermal hysteresis decreases as the first-order character of the transition gets suppressed by the magnetic field.

In Figure 6.5b), the shift of the transition temperature T_t versus the applied field is shown for both heating and cooling curves in fields up to 10 T. By linear interpolation a field-dependent transition temperature shift of 3.2 $\mathrm{KT^{-1}}$ and 2.7 $\mathrm{KT^{-1}}$ for cooling and heating, respectively could be determined which is in good agreement to literature [182, 202]. Based on the magnetization data, the magnetic phase diagram was constructed (see Figure 6.5b) showing a ferromagnetic behavior below the cooling branch of the linear fit and paramagnetic behavior above the heating branch. The area in between both lines represents a mixed magnetic state region. A tricrital point could be extrapolated to a field of 16.7 T and a temperature of 317 K where no hysteresis should be observed and the material's transition turned into second-order type. In contrast to the above mentioned similarities with the existing literature, the obtained transition temperature of the $Mn_{1.32}Fe_{0.71}P_{0.5}Si_{0.56}$ phase differs from the literature values [203, 176, 178, 204]. To the best of our knowledge, the reported compositions in the literature are the nominal compositions and generally the actual compositions of the Fe_2P-type phases were not given in the literature. The control of the composition is not trivial and it needs to be adjusted as especially Mn and P prove to be quite volatile elements. The appearance of secondary phases also influences the overall stochiometry of the main magnetic phase and hence tunes the transition temperature unintendedly. The transition temperatures are sensitive to the actual composition of the phase, the origin of the observed differences in transition temperature can be explained by the slight compositional variations between the compared samples.

The entropy change ΔS_t, shown in Figure 6.6 for the cooling protocol was calculated from isofield magnetization curves in a temperature range from 220 to 330 K in field steps of 0.2 T up to a field of 10 T using the Maxwell equation 3.9. This type of determination was applied as the alternative way

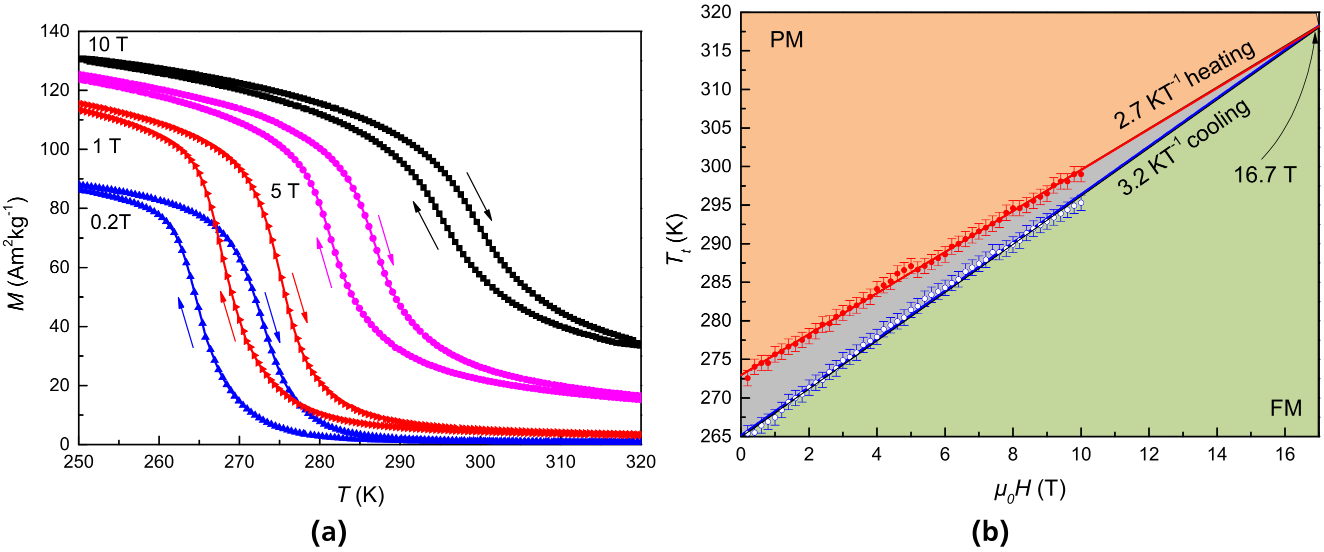

Figure 6.5: a) Magnetization versus temperature curves measured at different applied fields up to a field of 10 T measured on cooling and heating. b) Transition temperature T_t versus field obtained from the inflection points of the heating and cooling M-T curves up to 10 T. The straight lines represent a linear fit to the obtained data points. The intersection of the lines yield a tricritical point at 16.7 T at which the phase transition turn to second-order nature.

of calculation from isothermal magnetization curves as often used in literature has proven to be faulty especially in first order phase transitions of Fe_2P-alloys [28].

For field changes of 1 and 2 T, entropy change values ΔS_t of 8.5 and 17 Jkg^{-1}K^{-1} were obtained respectively. In fields higher than 5 T, the maximum entropy change saturates and slightly increases further in higher applied fields, due to the conventional second-order magnetocaloric effect overlaying the first-order transition in this material.

Being relevant for application, the low-field behavior of ΔS_t is plotted in Figure 6.7 showing no saturation in fields up to 2 T. In the inset of Figure 6.7, the calculated ΔS_t curves in a field change of 2 T are shown for heating and cooling. The area where the cooling and heating curves overlap (filled area) can be considered as the cyclic ΔS_t of the sample which is 16 Jkg^{-1}K^{-1} according to a method proposed by Kaeswurm *et al.* [205].

The adiabatic temperature change ΔT_{ad} was measured under a magnetic field change of 1.9 T as described in chapter 3.2.5 with a field-sweeping rate of 0.4 Ts^{-1} under cyclic conditions and is presented in Figure 6.8. A maximum ΔT_{ad} of 1 and 2.35 K was obtained for field changes of 1 and 1.9 T, respectively. In order to provide a more complete picture of the adiabatic temperature change, the time dependent magnetocaloric effect is plotted in the inset of Figure 6.8. It can be clearly seen that the effect of 2.35 K could only be achieved in the first field application. The cyclic ΔT_{ad} in this compound reduces to about 1.9 K for a field change of 1.9 T which can be explained by the thermal hysteresis. The field-dependent maximum values for the non-cyclic adiabatic temperature change are shown together with the isothermal entropy change in Figure 6.7. Whereas, the values of ΔS_t are comparable, the values of ΔT_{ad} are considerably lower than presented in literature for other Fe_2P-type compounds of comparable

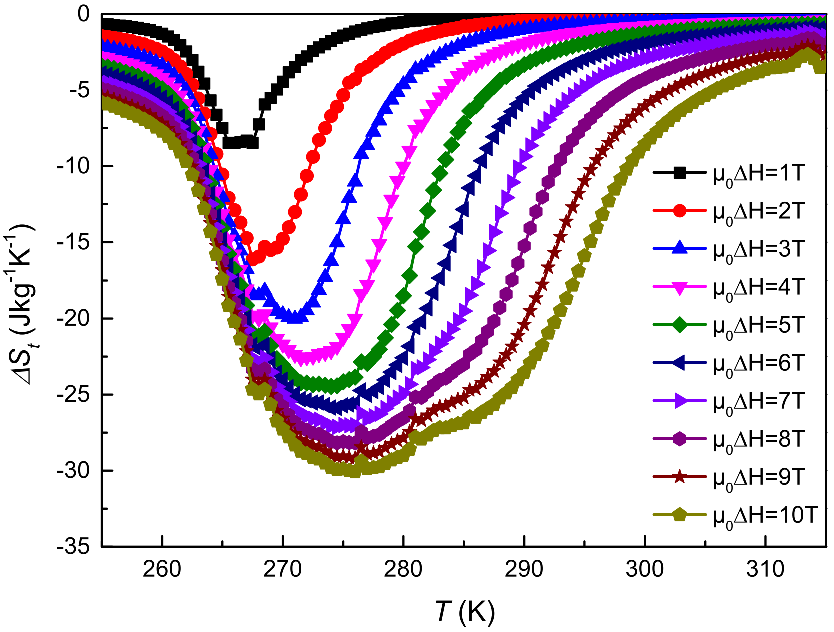

Figure 6.6: Temperature dependent magnetic entropy change ΔS_T for field changes of 1 to $10\,\mathrm{T}$ obtained from isofield magnetization measurements using the Maxwell equation.

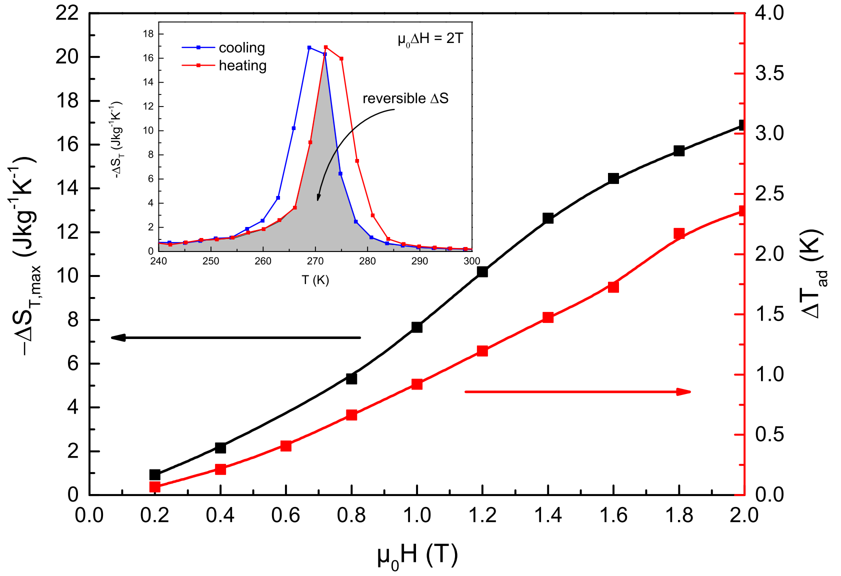

Figure 6.7: Field-dependent maximum adiabatic temperature change ΔT_{ad} and entropy change ΔS_t measured in a field change of 1.9 and $2\,\mathrm{T}$ respectively. The inset shows ΔS_t on heating and cooling in a field change of $\mu_0 \Delta H = 2\,\mathrm{T}$ calculated using the Maxwell equation. The hatched area represents the reversible ΔS_t for a cyclic field application.

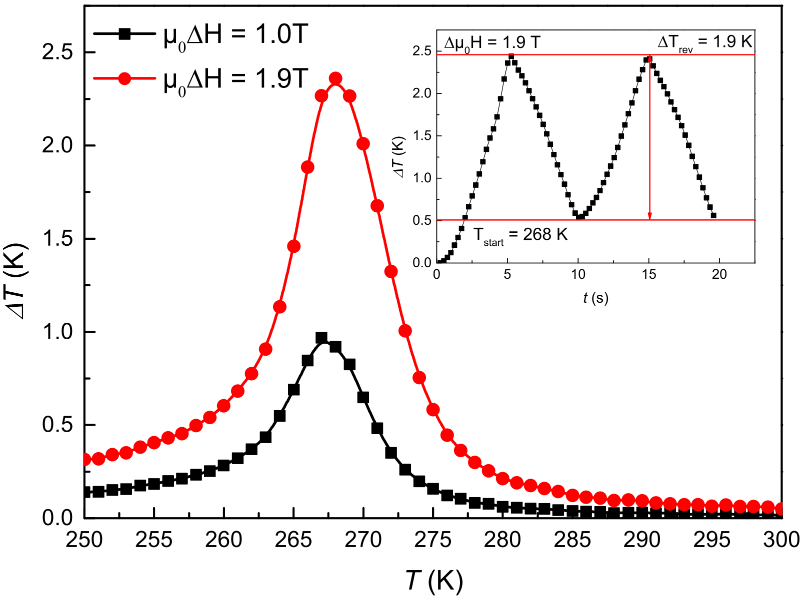

Figure 6.8: Adiabatic temperature change ΔT_{ad} of $Mn_{1.32}Fe_{0.71}P_{0.5}Si_{0.56}$ in field changes of 1 and 1.9 T measured on the cooling branch. The inset shows the time-dependent magnetocaloric effect at a temperature of 268 K showing a reversible ΔT_{ad} of 1.9 K.

stochiometry [180]. The reason for this discrepancy may be slight compositional differences between these specimen. The broader transition observed in the $M(T)$ measurements, together with a larger hysteresis and a smaller field-dependent shift of the transition temperature in applied magnetic fields, can also account for a lower adiabatic temperature change.

6.5 Influence of secondary phases

Structural and microstructural analysis presented in the previous sections reveal the occurrence of a secondary phase crystallizing in the cubic $Fm\bar{3}m$ structure. The question arises to what extent the magnetic properties are influenced by the occurrence and amount of the impurity phase. For this discussion, the comparison with a single-phase material is crucial.

Figure 6.9a) shows the $M(T)_H$ curves of three two-phase samples (Samples 1, 3 and 4, see Table 6.1) in comparison to that of a single-phase sample (Sample 2). An increasing amount of secondary phase leads to a significant drop in the transition temperature T_t and an almost linear decrease in the saturation magnetization M_s. Thus, the transition temperature of the sample with 6 wt.% impurity phase is lowered by 25 K compared to the single-phase sample. Moreover, just a minor amount of secondary phase of 3 wt.%, which even could not be detected in the X-ray diffraction pattern causes a shift of T_t by 9 K.

The reason for this significant decrease in T_t can be traced back to the change of stochiometry in the main phase due to the presence of the secondary-phase. As shown in the EDX maps (see Figure 6.2a)), this phase is strongly enriched with Si and Fe and slightly reduced with Mn in comparison to the main phase, while P is almost not present in this phase. This leads to an increase of the Mn/Fe-ratio as well as of the P/Si-ratio in the main phase with an increasing content of the secondary phase which is shown in

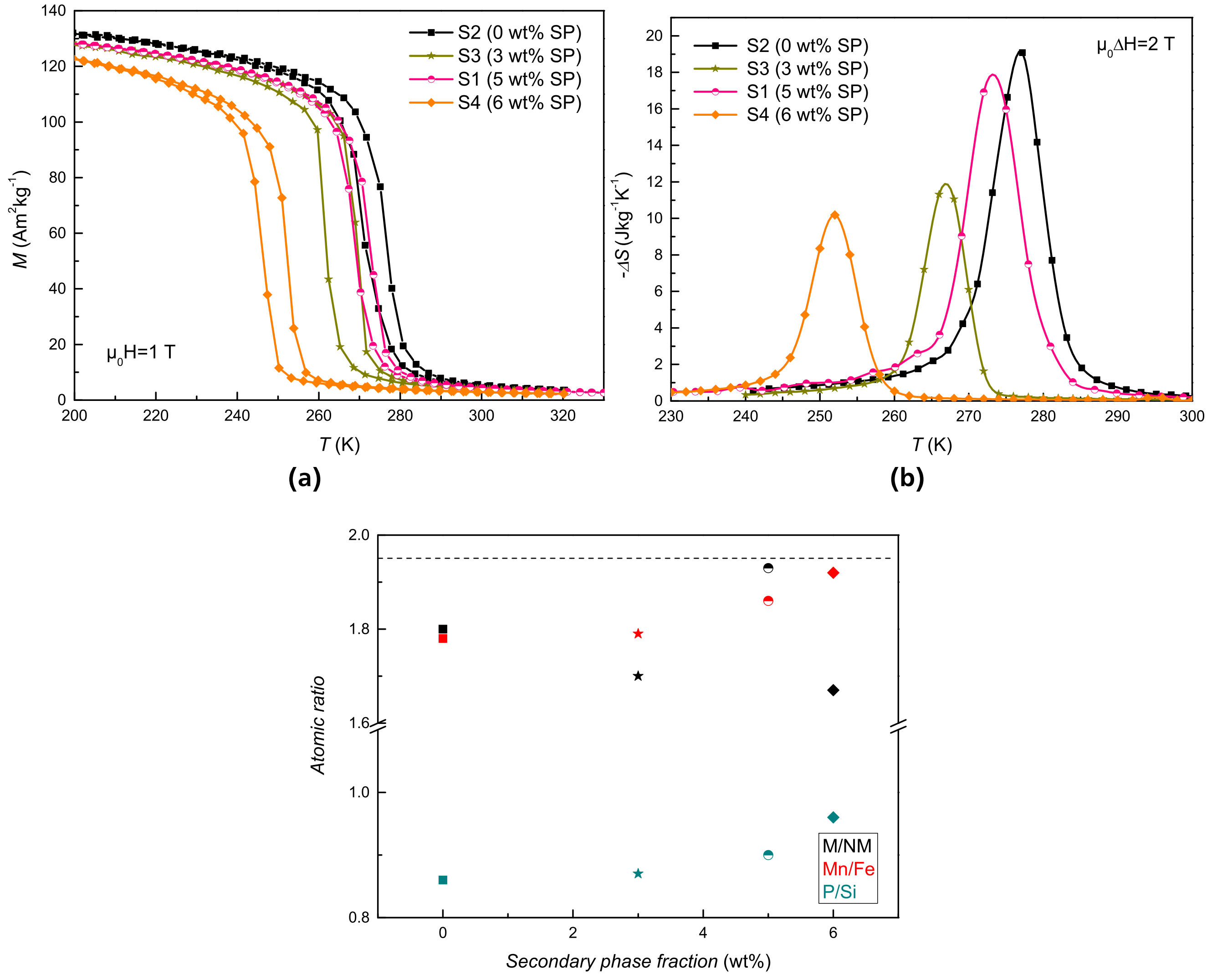

(a) **(b)**

(c)

Figure 6.9: a) Magnetization versus temperature curves recorded in a field of $1\,\mathrm{T}$. With increasing amount of secondary phase a decreasing transition temperature T_t and saturation magnetization M_s can be observed. b) Isothermal entropy changes (from ascending curves) for a field change of $2\,\mathrm{T}$. With increasing amount of secondary the isothermal entropy change decreases. c) Amount-of-substance ratios as a function of secondary phase fraction.

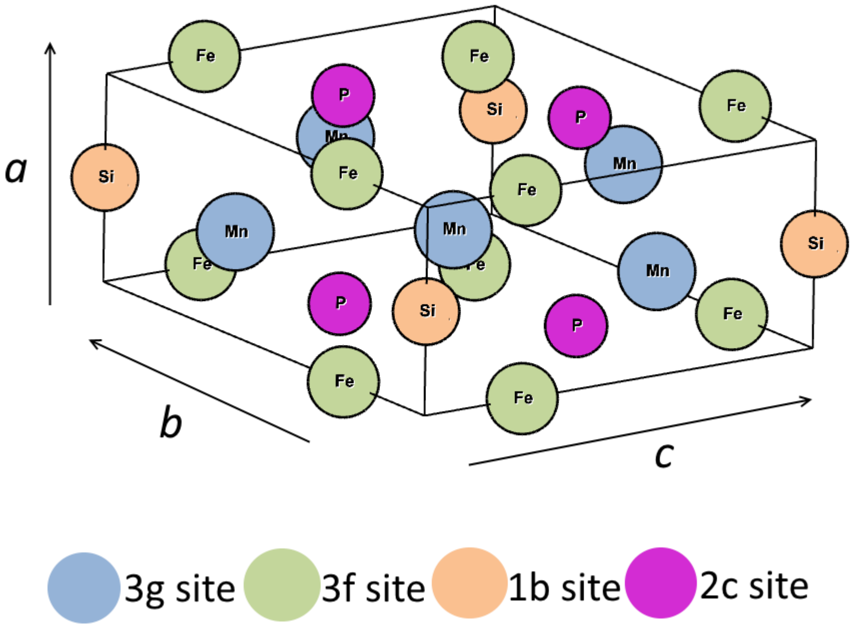

Figure 6.10: Representation of the Mn-Fe-P-Si Fe_2P-type crystal structure.

Figure 6.9c). Here, it can also be seen that the rising amount of the secondary phase is accompanied by a decrease in the metal/non-metal M/NM-ratio. However, this is not always the case, as the M/NM-ratio of the main phase depends on the grade of enrichment/depletion of Fe/Mn compared to the one of Si in this phase.

Both, the increase in the Mn/Fe- and the P/Si-ratio lead to a lowering of T_t as discussed in [203] and [188] which can be explained by a change in the site occupancy in the crystallographic lattice [178, 206]. A simplified schematic of the Mn-Fe-P-Si unit cell is shown in Figure 6.10. While the Mn atoms are preferentially positioned on the pyramidally coordinated 3g sites of the lattice, the Fe atoms prefer the tetrahedrally coordinated 3f sites. However, in a Mn-rich sample, the Mn atoms substitute Fe atoms on the 3f sites, reducing the magnetic moment of the 3f layer with increasing Mn content. Thus the rise in the Mn/Fe-ratio is accompanied by a decreasing moment of the 3f layers, leading to a lowering of T_t [178]. Another contribution to the decrease in transition temperature originates from the increase in the P/Si-ratio leading according to [206] to a reduced occupation of the 2c sites by Si. This weakens the magnetic moment of the 3f site resulting in a decrease in T_t. As both, an increasing Mn/Fe-ratio and P/Si-ratio result in a weakening of the total magnetic moment, there is also a small contribution in the lowering of the M_s [178, 206].

The major role in the decrease in M_s can be ascribed to the much lower magnetization of the secondary phase, which is according to [207] in the paramagnetic state for the whole measuring range. This is based on the finding, that almost the exact M_s values of the impurity samples can be determined by multiplication of the single-phased M_s with the secondary phase fraction in wt%. A trend concerning the thermal hysteresis cannot be identified in Figure 6.9a). This is in agreement with electronic structure calculations in [176], showing an opposing effect on the thermal hysteresis with increasing Mn/Fe- (decreasing thermal hysteresis) and P/Si-ratio (increasing thermal hysteresis).

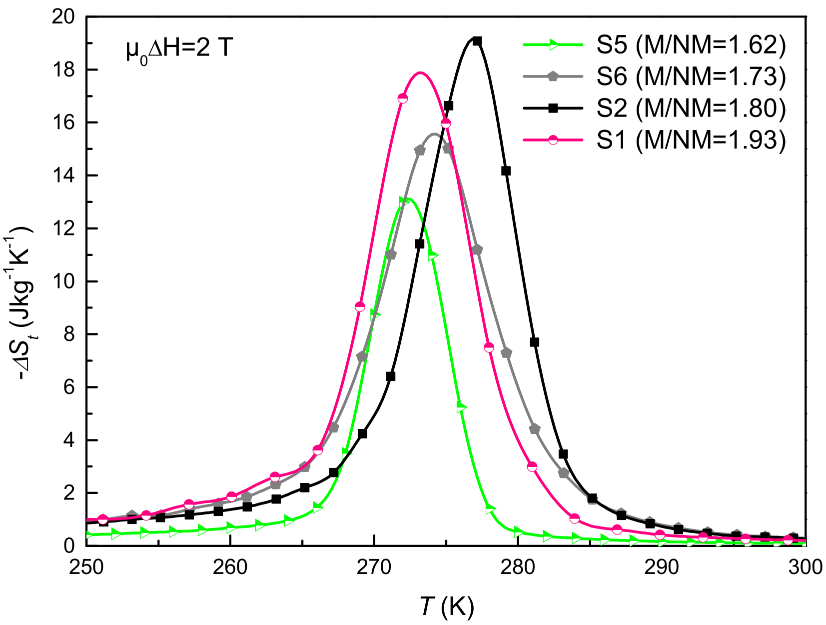

Figure 6.11: Isothermal entropy changes (from ascending curves) for a field change of 2 T. With increasing deviation of the M/NM-ratio from 1.95 the isothermal entropy change decreases for single-phase samples.

Figure 6.9b) shows the isothermal entropy change for a field change of 2 T. The isothermal entropy change increases from $-10.2\,\mathrm{Jkg^{-1}K^{-1}}$ of the sample with the highest impurity amount to $-19.1\,\mathrm{Jkg^{-1}K^{-1}}$ of the single-phase sample. In order to understand what makes the sample with 5 wt.% impurity phase so different from the others one should have a look at Figure 6.9c) again. While the Mn/Fe- and P/Si-ratio of the sample with 5 wt.% secondary phase fits almost perfectly into the trend, there is a big difference in the M/NM-ratio in comparison to the other samples, having huge consequences on the magnetocaloric properties. Although, the increasing amount of secondary phase should lead to a further shift in transition temperature and saturation magnetization as the Mn/Fe- and P/Si-ratio further increase, an even higher transition temperature than for the sample with 3 wt.% secondary phase and a comparable saturation magnetization can be observed. Moreover, this sample reveals a much lower thermal hysteresis and a much higher ΔS_t than the other two phase samples. This can be attributed to the M/NM-ratio which is much closer to 1.95 in off-stochiometric $(\mathrm{Mn,Fe})_{1.95}(\mathrm{P,Si})$ alloys. Besides the dependence of the magnetic properties on the Mn/Fe- and P/Si-ratio, the M/NM-ratio seems to have an even larger influence on the magnetic properties.

For the analysis of the influence of the M/NM-ratio in non-stoichiometric $(\mathrm{Mn,Fe})_{1.95}(\mathrm{P,Si})$ alloys, it is of great importance to avoid the formation of secondary phases in order to exclude other effects on the magnetic properties. Thus two further single-phase samples with M/NM-ratios of 1.62 and 1.73 (Sample 5 and 6, see table 6.1) were analyzed besides the ones regarded above having a M/NM-ratio of 1.8 (Sample 2). In Figure 6.11, a clear trend can be observed, that with an increasing deviation of the M/NM-ratio from 1.95 there is a reduction of the isothermal entropy change ΔS_t and the transition temperature for the single-phase samples. A particularity in Figure 6.11 is again given by the sample containing 5 wt.% secondary phase (Sample 1), which has a M/NM-ratio of 1.93. So the isothermal entropy change of this sample exceeds the one of the single-phase samples having M/NM-ratios of 1.62 and 1.73. This can be traced back to its much lower deviation from a M/NM-ratio of 1.95.

6.6 Influence of pressure on the magnetic phase transition

Pressure dependent magnetization curves in a field of 1 T were measured on a small fragment of a Fe_2P alloy (Sample 5 in Table 6.1) with a composition of $Mn_{1.20}Fe_{0.68}P_{0.5}Si_{0.66}$ in a hydrostatic pressure cell in a PPMS-14T VSM magnetometer. The study of this effect is of special interest as a concept of multi-stimuli magnetocaloric cooling was previously proposed by many researchers [54, 208, 209, 210, 211, 212], exploiting not only the magnetocaloric effect of a material but also its barocaloric effect. As mentioned before, Fe_2P type alloys exhibit a conventional magnetostructural phase transition since the low-temperature ferromagnetic phase transforms into a high temperature phase with low magnetization (shown in Figure 6.12). Whereas an external magnetic field tends to stabilize the phase with higher magnetization and therefore shifting the transition to higher temperature (see Figure 6.5). The application of a hydrostatic pressure will favor the phase with a smaller volume [26]. Different pressures were subsequently applied to the material and the results are shown in Figure 6.12. The point of inflection for the cooling curve is 270 K for a pressure of 0 GPa and shifts to a temperature of 273 K at 0.54 GPa with an unchanged thermal hysteresis of about 8 K. The shift of transition temperature is nearly negligible if compared to that of other magnetocaloric materials like La-Fe-Si or Heusler alloys where the shift is about $|50\,\mathrm{KGPa}^{-1}|$ [213]. The behavior of such a small barocaloric effect is attributed to the fact that as mentioned previously the overall volume change during the magnetic phase transition is only about 0.2%. In any case, most probably Fe_2P alloys would exhibit a large barocaloric effect under uniaxial pressure as the change in c lattice parameter is about -1.7% and 0.8% in a direction. Large effects will only be measurable in single crystals or well oriented and aligned polycrystalline materials, however, these materials are not part of this thesis.

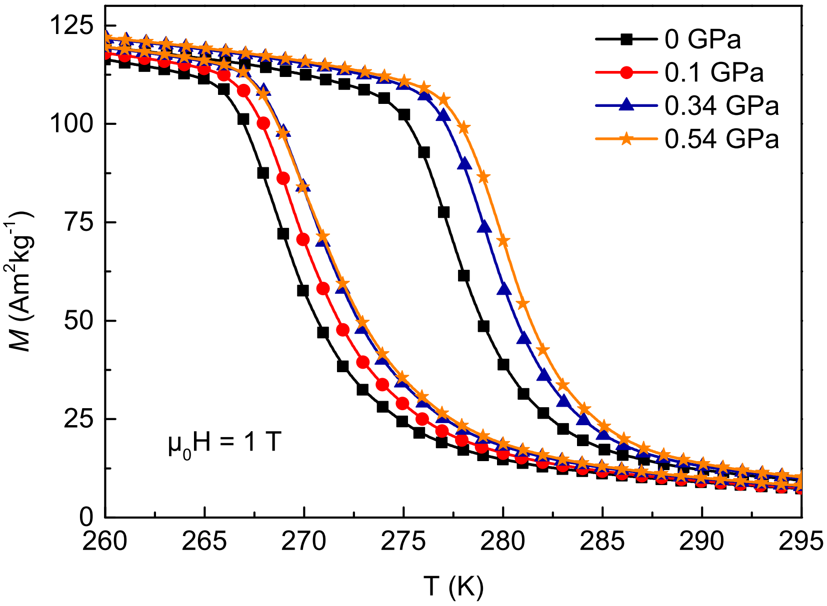

Figure 6.12: Magnetization versus Temperature curves in an applied field of 1 T under various hydrostatic pressures.

6.7 Influence of particle size on the magnetic phase transition

Shaping of magnetocaloric structures is very important for application in order to ensure a proper heat exchange between the material and the working fluid and to minimize pressure drops within the regenerator lowering the overall performance. A magnetocaloric material can be used as a powder bed where the heat exchange medium like water flows through the material with a maximum heat transfer between the fluid and material. A compromise needs to be found between maximum heat transfer due to a smaller particle size and a reasonable pressure drop through the packed bed. On the other hand, the use of bulk like heat exchangers appears to be more favorable for application due the better fluid dynamic properties. Special care needs to be taken when thinking about the heat transfer. Furthermore, the surface finish quality is of importance in order to eliminate friction losses. It was shown that for producing heat exchanger plates for example by polymer binding a plate thickness of $< 300\,\mu$m is necessary in order to achieve a reasonable heat transfer [214] meaning that the used particles need to be considerably smaller than this. The same is true when thinking about producing heat exchangers by additive manufacturing. Here, mostly powders are needed as a base ingredient like for example shown in the La-Fe-Si-family by selective laser melting [215]. Therefore, the influence of particle size of for magnetocaloric materials is not only of pure academic interest but is an important aspect when materials need to be implemented into a regenerator structure.

Measurements of the particle-size dependent magnetic properties of Fe_2P-type alloys were performed together with Tino Gottschall and are also a part of his PhD thesis. Measurements were performed on particles of sample S5 (see Table 6.1) with the composition $Mn_{1.20}Fe_{0.68}P_{0.5}Si_{0.66}$. The results are plotted in Figure 6.13. For all particles two subsequent $M(T)$ curves at 1 T were recorded in order to capture the virgin effect as mentioned before. The largest particle of $300\,\mu$m in size, switches from a paramagnetic

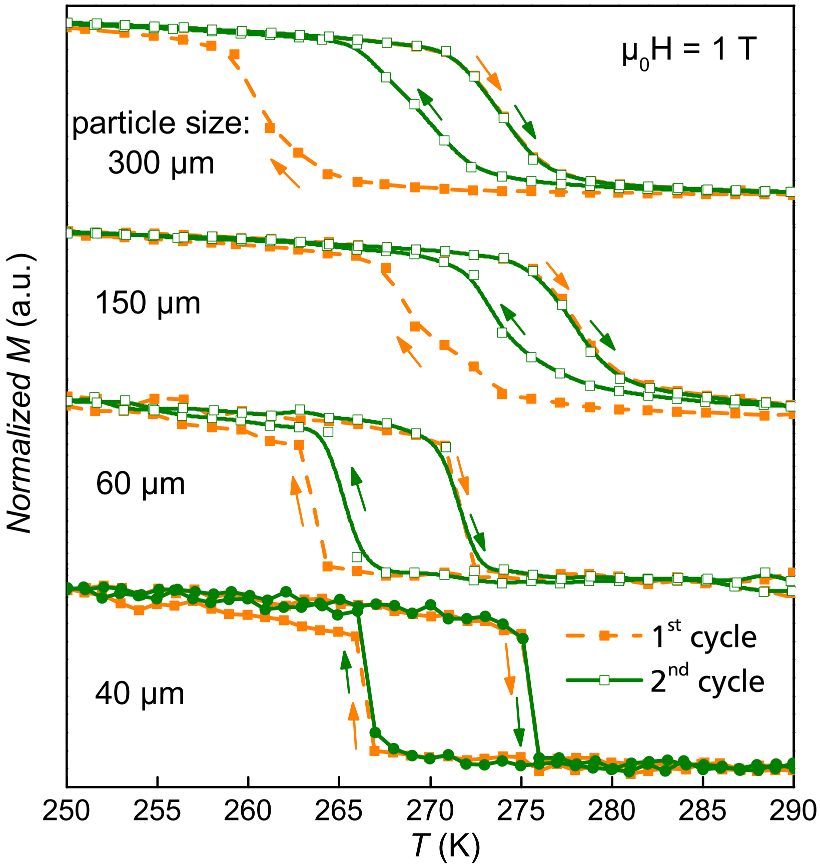

Figure 6.13: Magnetization measurements of single particles of $Mn_{1.2}Fe_{0.68}P_{0.5}Si_{0.66}$ in a field of 1 T. The magnetization data is normalized to ensure a better comparability between the measurements.

to ferromagnetic state, starting from 265 K at the first cooling cycle. On the second cycle the sample transforms at around 275 K around 10 K lower than on the first cycle which is attributed to the virgin effect. Interestingly the temperature difference between first and second cooling cycle decreases with decreasing particle size. No virgin effect can be observed at a particle size of 40 μm. EBSD measurements on this sample have shown that the average particle size in this compound is 38 μm. One can assume that the 40 μm particle is a single crystal like particle with no grain boundaries present. Furthermore, smaller samples seem to transfer in a jump like transition and thermal hysteresis increases with smaller particle size. The differences in transition temperatures T_t are ascribed to compositional fluctuations within the bulk sample. The loss of the virgin effect in small particles is ascribed to the fact, that no stresses can build up in the sample. In a single particle with no grain boundaries, the particle can expand in every direction during transition not allowing for stress to be built up and therefore hindering the phase transition.

Other than in Heusler alloys [213] the properties of small particles make them usable in packed bed heat exchangers or in bonded plates. The properties are very similar to the La-Fe-Si family where high quality bonded plates have been shown [82, 216] which also could be a possible way of implementing the brittle Fe_2P material into applicational heat-exchangers.

6.8 Dynamical effects of ΔT_{ad} under different field application rates

In the first section of this sub-chapter, the magnetic properties of the $Mn_{1.3}Fe_{0.7}P_{0.5}Si_{0.55}$ (sample 7 in table 6.1) are discussed, followed by the characterization of the adiabatic temperature change ΔT_{ad} first in ”slow” field application conditions and second for the ”fast” field application. The section is concluded by comparing the absolute ΔT_{ad} for both measurements procedures.

6.8.1 Magnetic properties

Isofield magnetization measurements versus temperature are plotted in Figure 6.14a) for fields of 0.2, 2, 10 and 14 T. The ferromagnetic to paramagnetic transition starts at 250 K and the material is fully transformed at 270 K in 0.2 T. During the transition, the material undergoes a hexagonal to hexagonal isostructural magneto-elastic phase transformation with only a small volume change of the unit cell [176]. The transition in $Mn_{1.3}Fe_{0.7}P_{0.5}Si_{0.55}$ is accompanied by a thermal hysteresis of about 7 K between the heating and cooling branch in a field of 0.2 T. The 14 T curve shows that the transition is shifted to higher temperatures and broadens drastically with a reduced thermal hysteresis of 4.5 K.

Figure 6.14c) depicts the variation of the transition temperature T_t with the applied field. T_t was determined from the mean of both the minima of the second derivative of the $M(T)$ curves for the heating and cooling curves. A different shift of T_t can be observed for heating (2.63 $\mathrm{KT^{-1}}$) and cooling (2.81 $\mathrm{KT^{-1}}$). Linear extrapolation of both curves yield a critical field and temperature of 36 T and 360 K where both curves intersect and no hysteresis should be observable. At this point the transition should turn into a pure second-order type.

Figure 6.14c) is interpreted as a magnetic phase diagram where the area underneath the cooling curve presents a pure ferromagnetic and the area above the heating line a pure paramagnetic region. The area in between represents a mixed magnetic region where both ferromagnetic and paramagnetic hexagonal phases are present in the material.

Figure 6.14b) illustrates the field-dependence of the magnetization at different temperatures. At 10 K, $Mn_{1.3}Fe_{0.7}P_{0.5}Si_{0.55}$ shows a saturation magnetization of 150 $\mathrm{Am^2kg^{-1}}$ which decreases with increasing temperature. The magnetization loops represent non-hysteretic typical soft-magnetic behavior up to a temperature of 255 K. Loops in the temperature range between 255 and 285 K are typical for materials with a first-order magnetostructural phase transition and can be correlated to the magnetic phase diagram in Figure 6.14c). At a temperature of 265 K, a phase transition is induced in a field lower than 0.5 T. This becomes even more obvious when studying the behavior at 270 and 275 K where a PM to FM phase transition can be induced at approximately 2 and 4.5 T respectively, agreeing very well with the phase diagram.

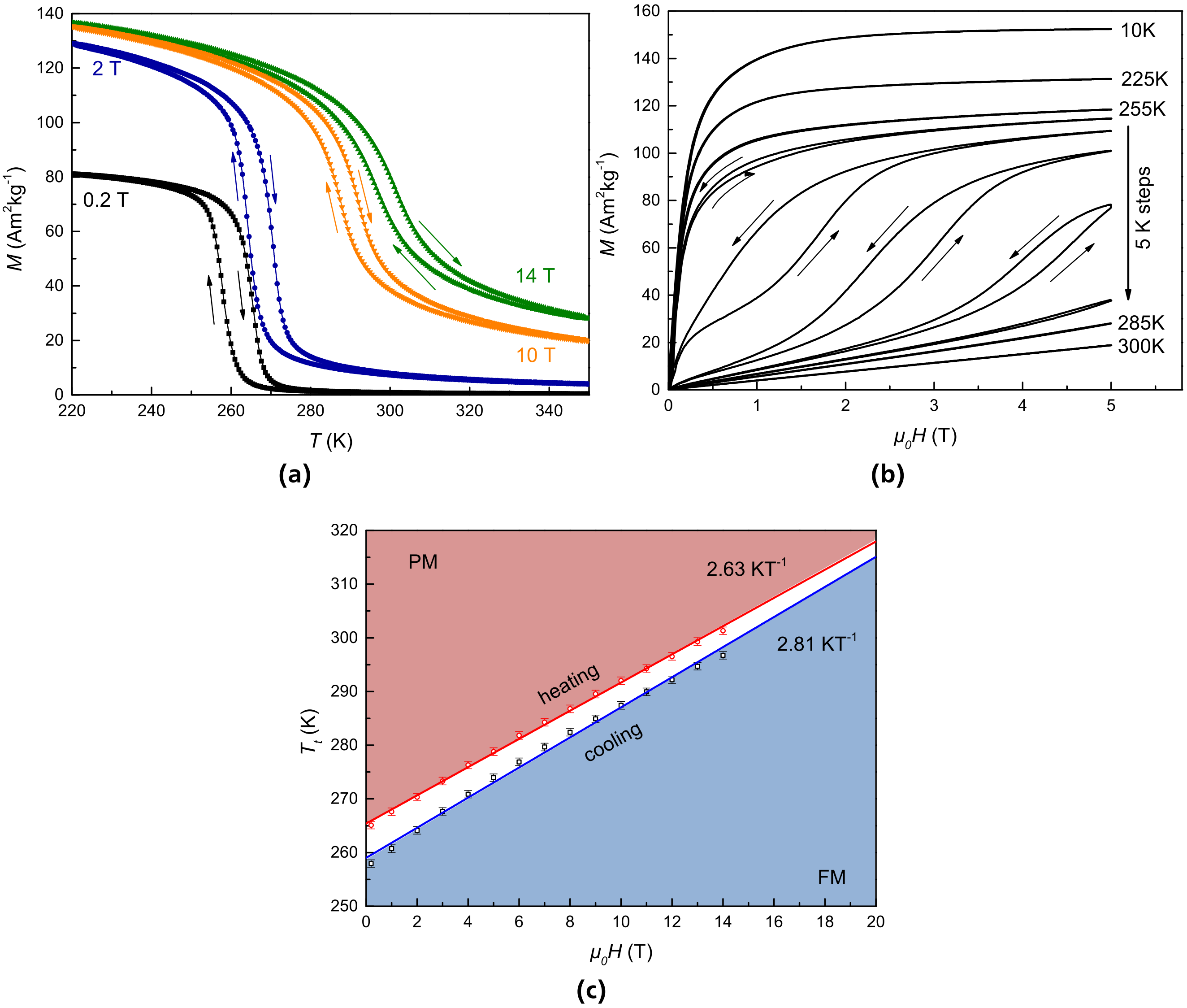

Figure 6.14: a) Magnetization versus temperature for fields of 0.2, 2 10 and $14\,\mathrm{T}$. b) Magnetization versus applied field at different distinct temperatures below, at and above the transition temperatures. c) Illustration of the shift of the transition temperature T_t versus the applied field $\mu_0 H$ for both heating and cooling curves.

6.8.2 Measurements of adiabatic temperature change in a Halbach setup

The adiabatic temperature change measured in the ”slow” field application rate as described in chapter 3.2.5 is shown in Figure 6.15a) for distinct temperatures plotted versus time. The red dotted line indicates the absolute sinusoidal magnetic field profile of the Halbach magnet setup generating a field difference of ± 1.93 T in a time of 12.8 s.

At a temperature of 250 K, an adiabatic temperature change ΔT_{ad} of 1 K can be observed in the first application cycle, matching the value in the second field application cycle to -1.93 T. The temperature change follows the sinusoidal shape of the field profile, with the temperature of the sample rising directly after the field application. An irreversibility in the adiabatic temperature change can be observed, as the material only shows a reversible ΔT_{ad} of 0.75 K due to thermal hysteresis being an indication of a first-order phase transition. The transition follows a minor loop of thermal hysteresis traveling through a mixed magnetic state region (coexistence of ferro- and paramagnetic phases).

As mentioned before, the material is always heated to a temperature of 300 K prior to every field application cycle in order to reach a fully paramagnetic state and is then cooled down to measurement temperature. At 250 K the material has not yet fully transformed to a pure ferromagnetic state, but is locked in a mixed state due to the width of the transition which is not represented in the phase diagram shown in Figure 6.14b). This cannot be observed by the measurements of $M(T)$ and $M(H)$ shown in Figure 6.14a) and c) as a continuous temperature sweep was applied. This behavior is not uncommon for first-order transition materials has been found for example in Heusler alloys [217]. The mixed state can also result from the chemical inhomogeneity of the sample which was already shown for Fe_2P-type alloys [190] or from stress building up in the sample due to the anisotropic lattice expansion through the phase transition in this system [176] hindering the nucleation and growth process of the ferromagnetic phase [213]. This effect is even more pronounced when at 255 K, moving closer to the ferromagnetic phase line with no indication of field induced phase transition in Figure 6.14c).

At a temperature of 260 K the material is exactly at the edge of the mixed phase (see Figure 6.14c)) and the largest adiabatic temperature change of 2.1 K can be observed at this temperature, still following the field profile of the setup. A deviance of this behavior can be observed at a temperature of 265 K and even more at 270 K. The delay of the curve can be easily explained when comparing the $\Delta T_{ad}(s)$ with the isothermal $M(H)$ loops in Figure 6.14b). The field required to induce the phase transition rises with temperature, consequently the temperature change of the material occurs in higher magnetic fields and is delayed in time. At the same time a field of 1.93 T is not high enough to fully transform the material, ΔT_{ad} being lower than that measured at 260 K where the field is also insufficient to fully transform the material.

The field dependence of ΔT_{ad} is plotted in Figure 6.15b) for the same starting temperatures as discussed before. At a temperature of 250 K thermal hysteresis can be observed. The ΔT_{ad} curve opens on the first field application cycle and the temperature change on removing the field is not as high as for the field application branch. Both field application and removal temperature change branches follow a linear

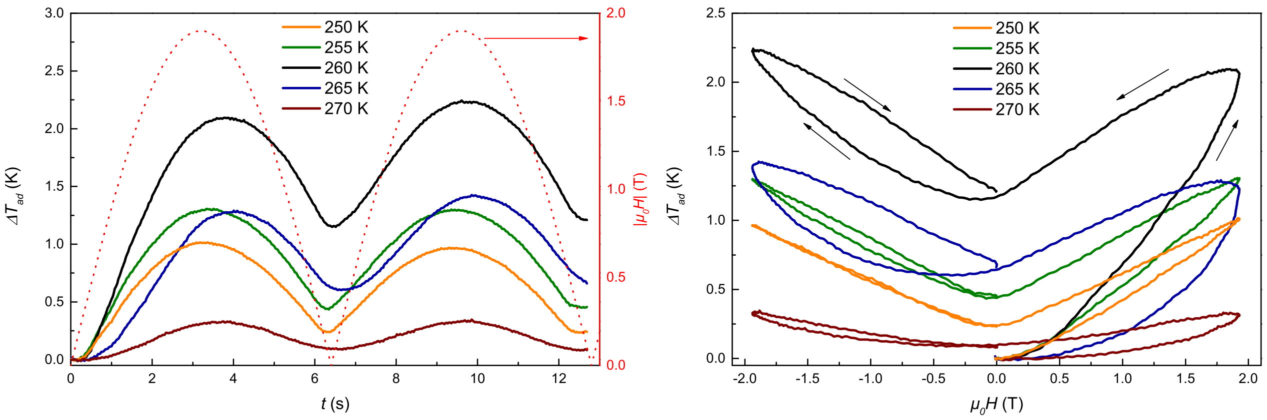

(a)

(b)

Figure 6.15: Adiabatic temperature change measured in a Halbach magnet setup with a field change of 1.93 T plotted versus time in a) and field in b) for two consecutive field application cycles at distinct starting temperatures. The dotted line in a) indicates the time dependent magnetic field profile of the Halbach magnet setup.

field dependence. The second field application cycle is fully reversible. One can assume that due to an application of the magnetic field in the first cycle, all material is transformed and the material is now in a pure ferromagnetic state and a conventional fully reversible second-order magnetocaloric effect is present. Similar features are observed when starting the experiment at 255 K, whereas the temperature loop of the second cycle opens up slightly indicating that the magnetoelastic transformation does not follow the same path at application and removal of the magnetic field.

Similar to Figure 6.15a) for the temperatures of 260, 265 and 270 K, the $\Delta T_{ad}(H)$ curves have a different shape compared to the other two temperatures due to the field induced phase transition. An opening of the $\Delta T_{ad}(H)$ loops can also be observed for the second field application cycle measured at starting temperatures of 260 and 265 K while being most pronounced at 265 K. At this temperature, the material transforms in a minor loop of magnetization in a mixed state region if compared to Figure 6.14c). The back and forth transformation follows two non-linear field dependent paths while undergoing the transition resulting in a distinct field hysteresis. This kind of complex transition behavior has been discussed by Gottschall $et\ al.$ for Heusler alloys and was ascribed in that case to the nucleation and growth process of the martensite and austenite phase [55]. At a starting temperature of 270 K, again close to the phase line depicted in Figure 6.14b), the second loop opens up slightly comparable to the measurement at 255 K yielding a slight first-order behavior.

6.8.3 Measurements of adiabatic temperature change in pulsed magnetic fields

The time dependent adiabatic temperature change ΔT_{ad} curves presented in Figure 6.16a) were recorded in a pulsed field setup as described in chapter 3.2.5 with a field change of 2 T. In contrast to the measurements shown in the previous section, the field application rate in the pulsed field setup is much higher than in the permanent magnet Halbach array setup, yet only one cycle can be performed

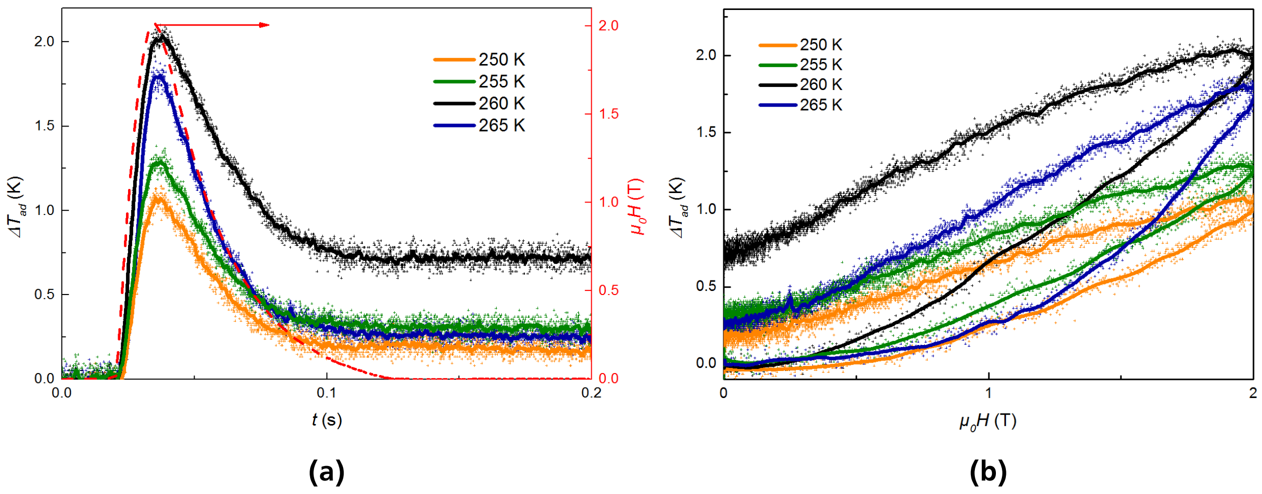

Figure 6.16: ΔT_{ad} versus time in a) and in b) versus applied magnetic field obtained from a pulsed field measurement with a field change of 2 T. The dashed line in a) represents the magnetic field profile of the pulse.

per experiment unlike in the Halbach setup. In the pulse setup, the field of 2 T is reached within 0.13 s with a maximum field change rate of 235 $\mathrm{Ts^{-1}}$ (shown in Figure 6.19a)). From Figure 6.16a) it can be seen that the material can follow the fast field application for all starting temperatures shown when compared to the dashed red line indicating the time dependent field profile. At a temperature of 260 K, the highest temperature change of 2.1 K is reached. As distinct features of the transition are not visible in the time dependent representation, the field dependent adiabatic temperature changes are plotted in Figure 6.16b) for the same starting temperatures as shown in a).

At a starting temperature of 250 and 255 K an adiabatic temperature change of 1 and 0.8 K respectively can be observed. Both curves exhibit an almost linear behavior and a slightly higher irreversibillity is present at 255 K. This behavior is in good agreement to Figure 6.15b) at the same temperatures measured in "slow" field application. At temperatures of 260 K and 265 K the material starts from a mixed phase region and also exhibits the same features as in 6.15b). The effect is therefore independent of the field application rate. Both curves show a large opening between the field application and removal cycle due to the irreversibility of the phase transition induced by the thermal hysteresis of the material. A change in the slope of the curve recorded at 265 K for field application is clearly visible at a field of about 1 T and corresponds well to the ferromagnetic to mixed state phase line shown in Figure 6.14b).

Measurements performed in pulsed fields of 10 T are shown in Figure 6.17. Here the maximum field is also reached in 0.13 s like in the case for 2 T with a maximum field change rate of 1345 $\mathrm{Ts^{-1}}$, being six times higher than in the previous measurements as shown in Figures 6.19a) and b). The time dependent ΔT_{ad} curves are shown in Figure 6.17a) together with the corresponding field profile indicated by a red dashed line. Comparing the curves from Figure 6.17a) to the field profile it seems that the transition follows the "fast" field changes at all starting temperatures. A change in temperature can be observed for all measurements when the magnetic field is applied, implying a good thermal contact between the thermocouple and the sample.

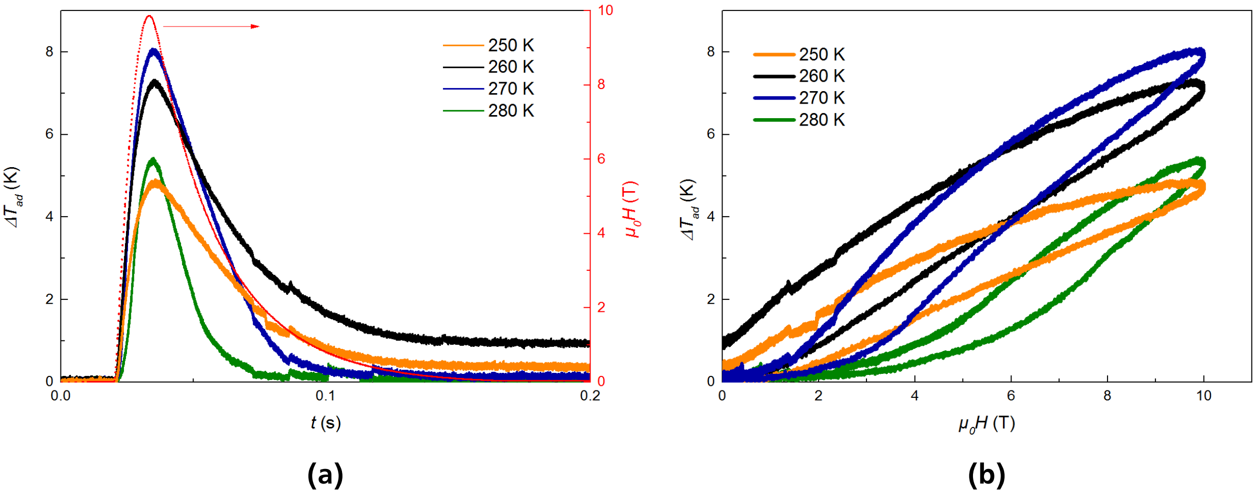

Figure 6.17: a) Time and b) field dependent adiabatic temperature change for distinct starting temperatures measured in a pulsed field of 10 T.

A maximum adiabatic temperature change of 8 K can be observed at a temperature of 270 K. This behavior coincides with the behavior of the adiabatic temperature change of a conventional first-order magnetocaloric material where the maximum ΔT_{ad} value is shifted to higher temperatures due to the shift in transition temperature comparable to the isothermal entropy change [31, 218, 219] (a schematic for the behavior of ΔS_t is shown in Figure 2.5). The slope of the temperature change on field removal is different for temperatures of 250 and 260 K when compared to the higher starting temperatures.

The field-dependent ΔT_{ad} curves are shown in Figure 6.17b). At a starting temperature of 250 K the temperature of the sample changes almost linearly with the applied magnetic field and opens upon field removal due to thermal hysteresis being evidence of a first-order phase transformation occurring similar to measurements shown in both Figures 6.15b) and 6.16b). This behavior is independent of the field application rate. A field of 10 T is not high enough to fully transform the material to a single ferromagnetic state, as can be also seen in the slight irreversibility of the temperature change. The largest thermal hysteresis is present at a starting temperature of 260 K likewise shown for all measurements. At a temperature of 270 K, a change in slope can be observed at around 3 T for field application and 1 T for field removal corresponding well to the magnetic phase diagram in Figure 6.14b) crossing both the ferromagnetic and paramagnetic phase line respectively. The same behavior is true for measurements performed at 280 K. At both measurements the temperatures of the samples return back to the starting temperature, as the starting temperatures are far away from the transition at zero field and therefore the material can transform back to the same ground state. However, the temperature does not follow the same path while transforming from a paramagnetic to a ferromagnetic state and back again.

In order study this behavior in more detail, measurements of ΔT_{ad} were performed at a starting temperature of 270 K at fields of 1, 5, 10 and 20 T. All measurements started from the same thermodynamic state as described in the experimental section. The results are shown in Figure 6.18. In a field of 20 T an adiabatic temperature change of 13 K could be achieved.

Up to a field of about 3 T all curves overlap and a slight temperature increase is present attributed to a field-rate independent second-order type magnetocaloric effect. Whereas, a change in the slope of ΔT_{ad} above 3 T can be observed for all different field application rates. This is consistent with the starting temperature of the transition as indicated with the dashed lines in Figure 6.18 marking the start of the first-order field induced phase transition. Furthermore, the change of sample temperature is nearly linear with the applied field. All temperature change curves show a distinct opening of the curves in dependence of the field. This behavior can neither be ascribed to a bad thermal contact of the sample with the thermocouple nor to a slow reaction time as measurements in this article have shown. The opening of the curves is a distinct feature of the transition as it can also be observed in the measurements of adiabatic temperature change with a Halbach magnet setup in Figure 6.15 and is ascribed to field-hysteresis. As the slope of the curves varies with the different pulses one can conclude that the first-order phase transition cannot follow the fast field changes completely and the nucleation and growth of the FM phase lacks behind the magnetic field change. No estimation can be given by the measurements on the actual speed of the transition. At 1 T all curves collapse on the same curve on field removal, in line with the starting temperature of the phase transition on the heating curve.

Both behaviors can be explained by the profile of the field pulse as shown in Figure **??**b). As all pulses, independent of the magnetic field strength, reach their maximum at the same time the field-change rate varies with the different pulses on the field application branch. Therefore, the slopes of the curves are different for all applied pulses as the heating rate of the material varies. On the contrary, in the field removal branch all curves of the field rate collapse on each other. Accordingly, the slope of the resulting ΔT_{ad} curves collapse on each other as can be seen in the inset of Figure 6.18.

Additionally, there is no saturation behavior of the magnetocaloric effect, even in fields of 20 T as observed in Heusler alloys or antiperovskites in similar measurements [185, 186, 187]. A similar behavior could be observed in Figure 6.6 where the isothermal entropy change was studied in fields to 10 T. In Fe_2P-type materials a continuously growing second-order type magnetocaloric effect overlaps the first-order transition as could be shown also for the measurements in this work, therefore no saturation behavior of ΔT_{ad} is observable.

6.8.4 Comparison of absolute adiabatic temperature change measurements on different time scales

The adiabatic temperature changes ΔT_{ad} versus the starting temperature are shown in Figure 6.20 for both the measurements with a ”slow” magnetic field change rate conducted in a Halbach setup and the ”fast” pulsed field measurements. It needs to be mentioned that the irreversible temperature change measured in a discontinuous measurement protocol is presented. The reversible values are considerably lower as shown in Figures 6.15, 6.16 and 6.17. When comparing the measurements performed in the Halbach array with a field change of 1.93 T and the measurements in pulsed fields of 2 T, one can see that the left, low temperature, shoulder of the curves perfectly overlap. Whereas, the right shoulder of the pulsed measurement is slightly shifted to the right due to the nature of a first-order phase transition as described earlier, as the field in the pulsed setup is just slightly higher. The overlap of both curves proves

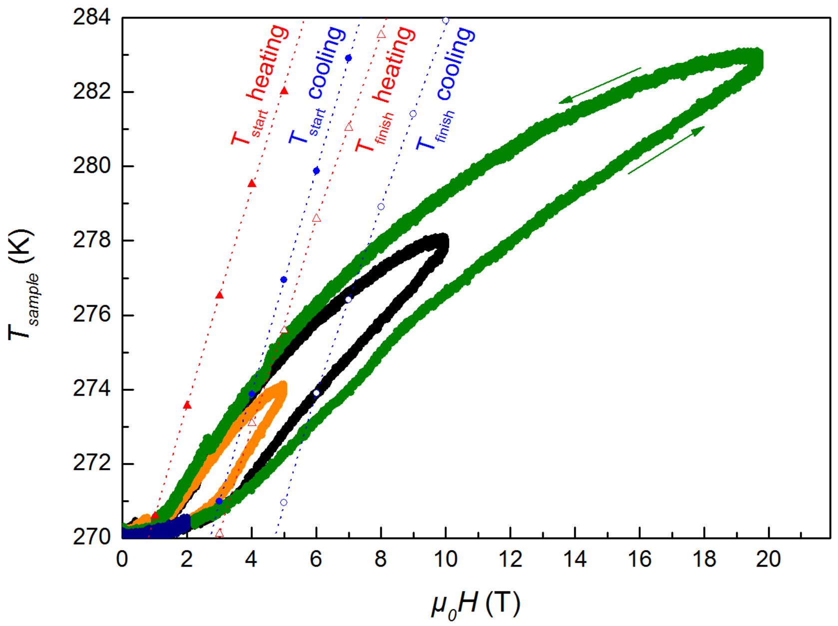

Figure 6.18: Field dependent ΔT_{ad} for pulsed field changes of 2, 5, 10 and $20\,\mathrm{T}$ with the corresponding phase lines for heating and cooling curves for the start and finish temperatures of the phase transition indicated by dotted lines. The inset shows the field dependent behavior of the magnetic field sweep rate for all pulses in this work. All measurements were performed at a sample temperature of $270\,\mathrm{K}$.

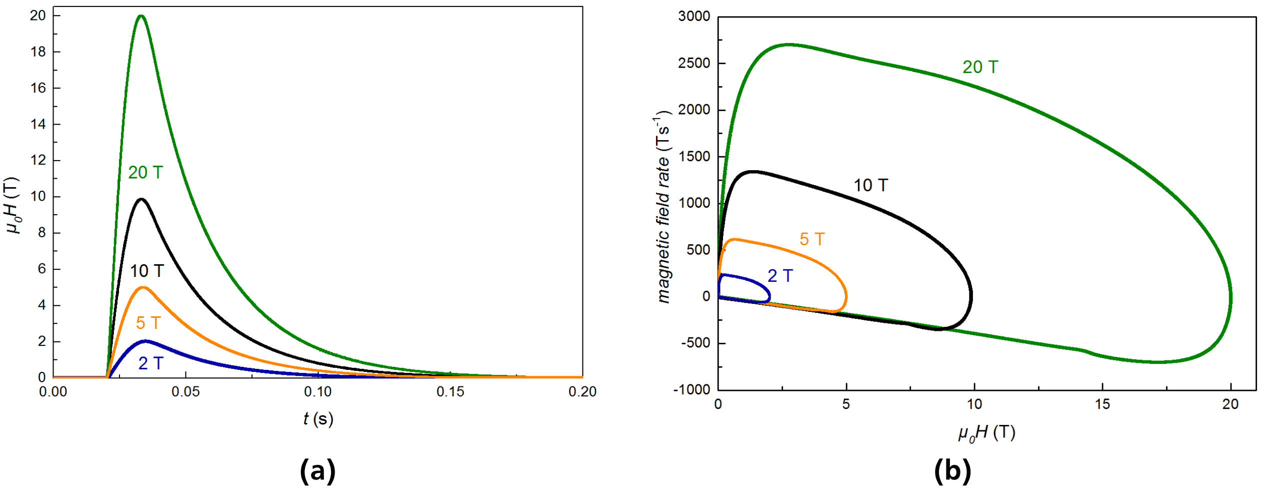

(a) (b)

Figure 6.19: a) Time dependent field pulse profiles and b) field dependent magnetization rates for field pulses of 2, 5, 10 and $20\,\mathrm{T}$.

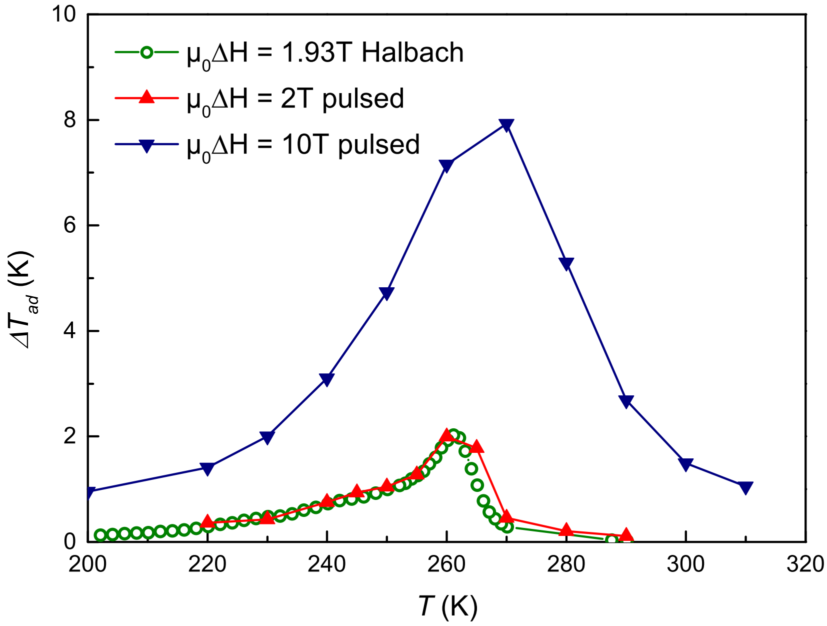

Figure 6.20: The irreversible adiabatic temperature change versus temperature for discontinuous measurements performed in a Halbach magnet array with a field change of 1.93 T and pulsed fields of 2 and 10 T.

not only the field rate independence of the maximum values of ΔT_{ad} in this region as also in [220], but also the quality of both measurements. A not negligible ΔT_{ad} can be observed with both measurement procedures in the ferromagnetic region which can be partly attributed to the second-order MCE as the material is not saturated in low fields as can be seen from Figure 6.14a) and close to the transition to a mixed-state region as described in part 6.8.2. The ΔT_{ad} at 10 T pulsed field is of similar shape as at 2 T with a shift of the maximum adiabatic temperature change to higher temperatures due to the induced phase transition.

In conclusion, the adiabatic temperature change was measured both in ”slow” magnetic field changes and in pulsed fields. The results were compared to the magnetic phase diagram. A saturation of the magnetocaloric effect could not be observed in fields up to 20 T attributed to the fact that a second-order phase transition always overlaps the first-order transition. It could be shown that the first-order phase transition is not field-rate independent as previously reported [220], yet the maximum values of ΔT_{ad} seem to be independent at least up to a field change rate of 235 Ts^{-1}. The second-order phase transition on the other hand can follow all field rates. Overall, the material is still usable in a real magnetic cooling device where frequencies below 100 Hz are expected, yet with a frequency dependent increase of field hysteresis which is lowering the efficiency of the material.

A distinct behavior of the temperature change could be observed in the mixed-state region of the material where the transition follows different paths on field application and removal, independent of the field application rate. This was related to a distinct nucleation and growth process of the magneto-elastic phase transition in Fe_2P-type alloys which should be studied in more detail.

Furthermore, a not negligible magnetocaloric effect of the material is measurable in the ferromagnetic region of the phase diagram which is ascribed partly to a second-order MCE and a mixed state region close to the transition temperature caused by chemical inhomogeneity or stress. Finally, it was demonstrated that pulsed fields are an adequate tool to directly asses the magnetocaloric effect in Fe_2P-type alloys in high fields.

7 Summary and outlook

In chapter 4 of this thesis the class of monoborides are proposed as potential candidate material for magnetic energy conversion. The structural, magnetic and magnetocaloric properties of refractory MnB, FeB with their pseudobinary derivatives $Mn_{1-x}Co_xB$ and $Mn_{1-x}Fe_xB$ were studied. All samples crystallize in the orthorombic base structure at room temperature. It could be shown that MnB has the highest saturation magentization of all ferromagnetic monoborides and could precisely determine its transition temperature. MnB undergoes a sharp ferromagnetic to paramagnetic phase transition at 567 K with an entropy change of 6.8 $\mathrm{Jkg^{-1}K^{-1}}$ with no hysteresis losses present. Whereas, the FeB compound has a much lower saturation magnetization, broader phase transition at nearly the same temperature as MnB resulting in a much lower entropy change. The nature of the phase transition of both compounds was studied using high resolution neutron powder diffraction. The proposed transition from an orthorhombic Pnma to Cmcm crystal structure at the magnetic phase transition as predicted by DFT calculations could not be confirmed. Additionally using Arrot-Belov plots and DSC measurements the nature of the phase transition was determined as second-order. The reason why MnB shows a much sharper phase transition than FeB could not be clarified up to now.

It was shown that the ordering temperature of the ferromagnetic monoboride compounds is tunable by doping: Fe-addition increases whilst Co-addition acts oppositely and lowers T_C. Doping, however, results in broader phase transitions and lower saturation magnetization leading to a reduction of entropy changes in the alloys.

DFT calculations could qualitatively account for the experimental findings as the energy landscape of the density of states (DoS) shares common features for the studied compositions. The high DoS at the Fermi level for MnB in the non-magnetic state ensures the energy gain by ferromagnetic order, according to the Stoner criterion. Adding an electron to MnB by doping of Fe shifts the position of the Fermi energy to higher energies, still satisfying the Stoner criterion. Ferromagnetism collapses in Co based monoborides due to a valley of the DoS at the Fermi energy. Based on the largest difference in the calculated NM and FM volumes, strong magneto-elastic interactions manifested in anomalous thermal lattice expansions are expected in the binary compound as well as in the moderately Fe-doped samples.

The investigated refractory monoborides show tunable MCE with sharp, hysteresis free transitions at elevated temperatures that could be exploited in the future in energy efficient thermomagnetic applications.

The system $Co_{2-x}Mn_xB$ was studied in terms of its structural, magnetic and magnetocaloric properties in chapter 5. On high quality single crystals of Co_2B the spin reorientation in this system and its magnetocrystalline anisotropy could be precisely determined. Co_2B switches from easy axis magnetocrystalline anisotropy to easy-plane anisotropy at the spin reorientation temperature of 72 K, these results could be supported by DFT calculations.

It was shown by measurements of ΔS_t and ΔT_{ad} on a single crystal that magnetocrystalline anisotropy can have large detrimental effects on the MCE especially in low fields below 1 T. This finding is of importance as especially in low fields the magnetocaloric material has to be used as efficiently as possible. Results show that particular care has to be taken when preparing heat exchangers from MCE materials with non-cubic crystal symmetry (materials that can show magnetocrystalline anisotropy). The use of textured non-cubic magnetocaloric materials is proposed with easy axis of magnetization parallel to the applied field in a real magnetocaloric working device to increase overall efficiency.

The magnetic properties of Co_2B are highly tunable by doping of Mn. The transition temperature can be precisely adjusted by adjusting the Co/Mn ratio to the desired temperature range below 420 K. An unusual behavior both in the transition temperature and saturation magnetization could be observed which is related to an increasing non-magnetic or antiferromagnetic interaction when increasing the Mn content in $Co_{2-x}Mn_xB$. It could also be demonstrate that this systems is not suited for magnetocaloric energy conversion due to it's high price and criticality of elements combined with low magnetocaloric performance.

Chapter 6 dealt with Mn-Fe-P-Si, Fe_2P based materials. Samples were produced by a powder metallurgical process followed by an annealing step and analyzed both structurally and magnetically.

XRD and EBSD measurements revealed the presence of a Phosphor depleted cubic Heusler-like secondary phase of $(Mn,Fe)_3Si$. Three distinct orientation areas of $(FeMn)_3Si$ could be observed with EBSD measurements. The distinct orientations give an insight into the formation process of the Fe_2P-type phase. Large zones with spatially separated grains sharing the same crystal orientation indicate the presence of a coarse grained single-phase microstructure at elevated temperatures. In this context it is likely that the hexagonal Fe_2P and the cubic $(FeMn)_3Si$ phase evolve from the decomposition of a single (presumably cubic) high temperature phase.

All studied samples revealed some porosity, leading to brittle samples and therefore hindering a direct bulk-like application of the material in heat exchanger structures. A direct observation of the virgin effect manifests itself in severe cracking of the sample that could be directly visualized by temperature-dependent in-situ optical microscopy. The cracking of the sample was attributed to large stresses originating from the anisotropic lattice expansion through the transition in the sample.

A deviation in thermomagnetic properties especially in the transition temperature, from literature values were observed and attributed to compositional changes occurring in the sintering and annealing step, as Mn and P have proven to be quite volatile, in contrary to the nominal compositions of the samples presented in literature. The differences in first time and cyclic field application were studied by measurements of of ΔS_t and ΔT_{ad}.

The occurrence and the amount of the secondary phases have a strong influence on the magnetic properties of the samples. A significant decrease of transition temperature, saturation magnetization and isothermal entropy change can be observed with increasing content of the secondary phase (SP). The importance of the metal to non-metal ratio (M/NM-ratio) was discussed, which strongly affects the magnetocaloric properties. It is highlighted that a M/NM-ratio of 1.95 is desirable in order to achieve good magnetocaloric performance with only a reasonable amount of secondary phases occurring in the sample.

Additionally, the dynamics of magnetic phase transition under different field application rates were studied using a permanent magnet based and pulsed field setup. ΔT_{ad} does not saturate in fields up to 20 T because a second-order phase transition always overlaps the first-order phase transition in Fe_2P alloys. It also could be shown that the first-order phase transition in this class of alloys is not independent of the field application rate as previously assumed whereas the inherent second-order phase transition is independent of the application rate. The transition follows minor loops of hysteresis when traveling through a mixed-state region which was attributed to a distinct nucleation and growth process of the magneto-elastic phase transition.

Overall, the experiments have shown that Fe_2P-type alloys are good candidates to be used in a magnetocaloric energy conversion process operating also at high frequencies below 100 Hz.

As a Ph.D. thesis only has limited time the before mentioned commercialization of thermomagnetic energy conversion was not achieved within the time-frame of this thesis. On the other hand, 2 different pathways were successfully followed, the search for potentially new and interesting systems and the better understanding of known systems. New building blocks were added to this topic on which future research on thermomagnetic energy conversion can and hopefully will build upon. In my opinion the effort of bringing this technology to the market can only be tackled by a combined effort of theoreticians, experimental materials physicists and engineers. Finding a common basis and language for these groups, coupled with the acceptance of the broad public for "green" energy technologies, will be the largest challenge on the way to a commercial product.

Adding to this I would like to make a few comments on where future work on the discussed compounds in this thesis could aim at, followed by a few more general remarks:

- Finding a more effective way of tuning the transition temperature in MnB other than substituting Mn by Fe or Co one could try substituting Ni on the Mn sites. Adding non-ferromagnetic elements on the Mn sites will only result in a lower overall magnetization. Additionally, the coupling of Mn could be altered by doping of the system on the non-magnetic B site with C, Al or Si. The compound $MnB_{1-x}P_x$ potentially might be of most interest as MnP shows also good MCE properties, but a synthesis was so far unsuccessful by means of conventional powder metallurgy.

- The clarification of the low temperature phase of MnB is of interest to the scientific community as preliminary results have shown interesting magnetic properties as preliminary magnetic characterization on single crystals has shown.

- The usage and synthesis of nano-particles of MnB and FeB could be explored in more detail. Both of them exhibit a high magnetization coupled with soft magnetic properties and experiments have shown that they are chemically very inert. Future studies could involve their applicability in biomedical applications as for example MRI agents or localized cancer treatment via hyperthermia.

- Producing high quality and structurally stable compounds of Mn-Fe-P-Si should be goal for commercialization of Fe_2P type compounds. This involves producing high purity samples with a M/NM-ratio of 1.95. This could be achieved by suppressing the formation of the cubic Heusler secondary-phase forming in the off-stochiometric compound by quenching the sample from the high temperature presumably cubic Fe_2P phase followed by a long time heat treatment in order to ensure and improve chemical homogeneity.

- The influence of microstructure, especially in the Fe_2P-system, on the thermomagnetic properties needs to be studied in more detail. Preliminary results yield that special attention should be paid on the grain size and distribution in order to increase the efficiency of the material. This could be achieved by crushing, sieving and re-sintering the formed compounds in order to be able to control the grain growth of the material. Orienting the particles in a magnetic field prior to re-sintering of the compound could also prove to be useful as shown in this work.

- Material physicists need to precisely measure properties not only like ΔT_{ad} and ΔS_t but also thermal conductivity λ, heat capacity c_p, density ρ and mechanical properties on a single composition. This data should be made available to the public coupled with a detailed description on how the data was obtained. Exact and realistic simulations of the thermomagnetic cycle or a complete device will only be possible by this way. This will ease the way of discovering possibly new and complex heat exchanger structures and magnetic field source arrangements in order to convert energy efficiently.

- Exploring additive manufacturing of thermomagnetic materials needs to be a goal for materials research as it may ease the way of constructing complex and structurally integer heat exchanger structures which would not be possible by conventional methods.

- Last, but maybe of highest importance, thermomagnetic energy conversion devices need to be presented which are quiet, of professional build quality and most importantly energy efficient in order to gain interest and curiosity within the broad mass of people. This will ensure future financial funding of research and collaboration possibilities which will also bring new ideas to this interesting and trendsetting technology.

Bibliography

[1] R. Balmer, *Modern Engineering Thermodynamics* (Elsevier Science, 30 Corporate Drive, Burlington, MA 01803, USA, 2011).

[2] Gleason's Drawing Room Companion, 1852, p.37.

[3] 100 Years of Refrigeration | A Supplement to ASHRAE (The American Society of Refrigerating Engineers) Journal, November 2004.

[4] W.-T. Tsai, Chemosphere **61**, 1539 (2005).

[5] R. McSweeny, Hydrofluorocarbon emissions up 54% with air conditioning on the rise, `https://www.carbonbrief.org/hydrofluorocarbon-emissions-up-54-with-air-conditioning-on-the-rise`, accessed: 2016-04-27.

[6] The Intergovernmental Panel on Climate Change (IPCC) , IPCC Second Assessment Climate Change - The Science of Climate Change: Summary for Policymakers and Technical Summary of the Working Group I Report 22 (1995).

[7] C. P. Janos Mate and S. Latif, Cool Technologies: Working without HFCs, Examples of HFC-free cooling technologies in various industrial sectors, 2012.

[8] Friedrichs Kältemittel, www.friedrichs-kaeltemittel.de.

[9] M. Isaac and D. P. van Vuuren, Energy Policy **37**, 507 (2009).

[10] International Monetary Fund, *World economic outlook (International Monetary Fund)* (International Monetary Fund, Publication Services, P.O. Box 92780, Washington, DC 20090, U.S.A., 2016).

[11] O. Gutfleisch, M. A. Willard, E. Brück, C. H. Chen, S. G. Sankar, and J. P. Liu, Advanced Materials **23**, 821 (2011).

[12] A. Kitanovski, J. Tusek, U. Tomc, U. Plaznik, M. Ozbolt, and A. Poredos, *Magnetocaloric Energy Conversion: From Theory to Applications* (Springer International Publishing, Gewerbestrasse 11, CH-6330 Cham (ZG), Switzerland, 2014), .

[13] H. Stanley, *Introduction to Phase Transitions and Critical Phenomena*, *International series of monographs on physics* (Oxford University Press, Great Clarendon Street, Oxford OX2 6DP, UK, 1971).

[14] P. Atkins and J. de Paula, *Physical Chemistry*, No. Bd. 1 in *Physical chemistry* (Oxford University Press, Great Clarendon Street, Oxford OX2 6DP, UK, 2006).

[15] M. P. Langevin, Annales de chimie et de physique 70 (1905).

[16] P. Weiss and A. Piccard, Journal of Theoretical and Applied Physics **7**, 103 (1917).

[17] A. Smith, The European Physical Journal H **38**, 507 (2013).

[18] W. F. Giauque and D. P. MacDougall, Physical Review **43**, 768 (1933).

[19] G. V. Brown, Journal of Applied Physics **47**, 3673 (1976).

[20] V. Franco, J. S. Blazquez, B. Ingale, and A. Conde, Annual Review of Materials Research **42**, 305 (2012).

[21] S. Chikazumi, *Physics of Ferromagnetism*, *International Series of Monographs on Physics* (OUP Oxford, Great Clarendon Street, Oxford OX2 6DP, UK, 2009).

[22] J. M. D. Coey, *Magnetism and Magnetic Materials*, *Magnetism and Magnetic Materials* (Cambridge University Press, The Edinburgh Building, Cambridge CB2 8RU, UK, 2010).

[23] K. P. Belov and A. N. Goryaga, Fizika Metallov I Metallovedenie **2**, 3 (1956).

[24] A. Arrott, Physical Review **108**, 1394 (1957).

[25] M. D. Kuz'min, Physical Review Letters **94**, 107204 (2005).

[26] T. Gottschall, K. P. Skokov, D. Benke, M. E. Gruner, and O. Gutfleisch, Physical Review B **93**, 184431 (2016).

[27] C. Luana, D. Nguyen Ba, and R. Laurent, Journal of Physics: Condensed Matter **29**, 075401 (2017).

[28] L. Caron, Z. Q. Ou, T. T. Nguyen, D. T. Cam Thanh, O. Tegus, and E. Brück, Journal of Magnetism and Magnetic Materials **321**, 3559 (2009).

[29] J. Lyubina, M. D. Kuz'min, K. Nenkov, O. Gutfleisch, M. Richter, D. L. Schlagel, T. A. Lograsso, and K. A. Gschneidner, Physical Review B **83**, 012403 (2011).

[30] V. Franco, J. S. Blazquez, and A. Conde, Applied Physics Letters **89**, 222512 (2006).

[31] O. Gutfleisch *et* al., Philosophical Transactions of the Royal Society A: Mathematical, Physical and Engineering Sciences **374**, 20150308 (2016).

[32] V. K. Pecharsky and K. A. Gschneidner Jr, Journal of Magnetism and Magnetic Materials **200**, 44 (1999).

[33] S. Taskaev, K. Skokov, D. Karpenkov, V. Khovaylo, V. Buchelnikov, D. Zherebtsov, M. Ulyanov, D. Bataev, M. Drobosyuk, and A. Pellenen, Acta Phys. Pol. A **127**, 641 (2015).

[34] D. Eriksen, K. Engelbrecht, C. R. H. Bahl, R. Bjork, K. K. Nielsen, A. R. Insinga, and N. Pryds, International Journal of Refrigeration **58**, 14 (2015).

[35] V. K. Pecharsky and J. K. A. Gschneidner, Physical Review Letters **78**, 4494 (1997).

[36] X. Moya, S. Kar-Narayan, and N. D. Mathur, Nature Materials **13**, 439 (2014).

[37] E. Commission, Report on Critical Raw Materials for the EU - Critical Raw Materials Profiles, 2014.

[38] F. Scarpa, G. Tagliafico, and L. A. Tagliafico, Renewable and Sustainable Energy Reviews **50**, 497 (2015).

[39] V. K. Pecharsky and K. A. Gschneidner, Advanced Materials **13**, 683 (2001).

[40] J. Liu, J. D. Moore, K. P. Skokov, M. Krautz, K. Löwe, A. Barcza, M. Katter, and O. Gutfleisch, Scripta Materialia **67**, 584 (2012).

[41] A. Barcza, M. Katter, V. Zellmann, S. Russek, S. Jacobs, and C. Zimm, IEEE Transactions on Magnetics **47**, 3391 (2011).

[42] M. Krautz, K. Skokov, T. Gottschall, C. S. Teixeira, A. Waske, J. Liu, L. Schultz, and O. Gutfleisch, Journal of Alloys and Compounds **598**, 27 (2014).

[43] S. Fujieda, A. Fujita, and K. Fukamichi, Applied Physics Letters **81**, 1276 (2002).

[44] A. Fujita, S. Fujieda, Y. Hasegawa, and K. Fukamichi, Physical Review B **67**, 104416 (2003).

[45] E. Lovell, A. M. Pereira, A. D. Caplin, J. Lyubina, and L. F. Cohen, Advanced Energy Materials **5**, 1401639 (2014).

[46] B. G. Shen, J. R. Sun, F. X. Hu, H. W. Zhang, and Z. H. Cheng, Advanced Materials **21**, 4545 (2009).

[47] K. Mandal, O. Gutfleisch, A. Yan, A. Handstein, and K. H. Müller, Journal of Magnetism and Magnetic Materials **290**, 673 (2005).

[48] C. Yuan-fu, W. Fang, S. Bao-gen, H. Feng-xia, S. Ji-rong, W. Guang-jun, and C. Zhao-hua, Journal of Physics: Condensed Matter **15**, L161 (2003).

[49] M. Krautz, J. D. Moore, K. P. Skokov, J. Liu, C. S. Teixeira, R. Schafer, L. Schultz, and O. Gutfleisch, Journal of Applied Physics **112**, 083918 (2012).

[50] O. L. Baumfeld, Z. Gercsi, M. Krautz, O. Gutfleisch, and K. G. Sandeman, Journal of Applied Physics **115**, 203905 (2014).

[51] Vacuumschmelze Magnetocaloric materials, `http://www.vacuumschmelze.com/index.php?id=1304`, accessed: 2017-01-24.

[52] K. P. Skokov, D. Y. Karpenkov, M. D. Kuz'min, I. A. Radulov, T. Gottschall, B. Kaeswurm, M. Fries, and O. Gutfleisch, Journal of Applied Physics **115**, 17A941 (2014).

[53] T. Krenke, E. Duman, M. Acet, E. F. Wassermann, X. Moya, L. Manosa, and A. Planes, Nature Materials **4**, 450 (2005).

[54] J. Liu, T. Gottschall, K. P. Skokov, J. D. Moore, and O. Gutfleisch, Nature Materials **11**, 620 (2012).

[55] T. Gottschall, K. P. Skokov, B. Frincu, and O. Gutfleisch, Applied Physics Letters **106**, 021901 (2015).

[56] O. Tegus, E. Brück, K. H. J. Buschow, and F. R. de Boer, Nature **415**, 150 (2002).

[57] E. Brück, X. F. Miao, H. Yibole, V. T. Nguyen, M. Boeije, and N. van Dijk, Solid State Phenomena **257**, 129 (2017).

[58] N. H. Dung, Z. Q. Ou, L. Caron, L. Zhang, D. T. C. Thanh, G. A. de Wijs, R. A. de Groot, K. H. J. Buschow, and E. Brück, Advanced Energy Materials **1**, 1215 (2011).

[59] F. Guillou, G. Porcari, H. Yibole, N. van Dijk, and E. Brück, Advanced Materials **26**, 2671 (2014).

[60] US DOE, Waste Heat Recovery: Technology and Opportunties in the U.S. Industry, 2008.

[61] US DOE EIA, Annual Energy Review, 2006.

[62] Energetics, Energy Use, Loss and Oppurtunities Analysis: US Manufacturing and Mining, p. 17, 2004.

[63] H. Goldsmid, *Introduction to Thermoelectricity*, *Springer Series in Materials Science* (Springer Berlin Heidelberg, Heidelberger Pl. 3, 14197 Berlin, Germany, 2016).

[64] X. Zhang and L.-D. Zhao, Journal of Materiomics **1**, 92 (2015).

[65] C. B. Vining, Nature Materials **8**, 83 (2009).

[66] B. Poudel *et* al., Science **320**, 634 (2008).

[67] A. Kitanovski, M. Diebold, D. Vuarnoz, C. Gonin, and P. W. Egolf, Applications of magnetic power production and its assessment - A feasability study, 2008.

[68] Fraunhofer ISI, Industrielle Abwärmenutzung, 2013.

[69] D. Vuarnoz, A. Kitanovski, C. Gonin, Y. Borgeaud, M. Delessert, M. Meinen, and P. W. Egolf, Applied Energy **100**, 229 (2012).

[70] V. Srivastava, Y. Song, K. Bhatti, and R. D. James, Advanced Energy Materials **1**, 97 (2011).

[71] N. Tesla, Thermomagnetic Motor, 1989, US Patent 396121 A.

[72] Swiss Blue Energy, `http://www.swiss-blue-energy.ch/index.html`, accesed: 02.01.2017.

[73] L. Brillouin and H. P. Iskenderian, Electrical Communications, Federal Communication Labories, Nutley, NJ 22937 (1948).

[74] J. F. Elliott, Journal of Applied Physics **30**, 1774 (1959).

[75] L. D. Kirol and J. I. Mills, Journal of Applied Physics **56**, 824 (1984).

[76] D. Solomon, Journal of Applied Physics **63**, 915 (1988).

[77] T. Christiaanse and E. Brück, Metallurgical and Materials Transactions E **1**, 36 (2014).

[78] C.-J. Hsu, S. M. Sandoval, K. P. Wetzlar, and G. P. Carman, Journal of Applied Physics **110**, 123923 (2011).

[79] A. Tishin and Y. Spichkin, *The Magnetocaloric Effect and its Applications* (CRC Press, 6000 Broken Sound Parkway, Boca Raton, FL, USA, 2003).

[80] K. G. Sandeman, Scripta Materialia **67**, 566 (2012).

[81] V. Basso, M. Küpferling, C. Curcio, C. Bennati, A. Barzca, M. Katter, M. Bratko, E. Lovell, J. Turcaud, and L. F. Cohen, Journal of Applied Physics **118**, 053907 (2015).

[82] K. P. Skokov, K. H. Müller, J. D. Moore, J. Liu, A. Y. Karpenkov, M. Krautz, and O. Gutfleisch, Journal of Alloys and Compounds **552**, 310 (2013).

[83] I. A. Radulov, K. P. Skokov, D. Y. Karpenkov, T. Gottschall, and O. Gutfleisch, Journal of Magnetism and Magnetic Materials **396**, 228 (2015).

[84] Y. Song, K. P. Bhatti, V. Srivastava, C. Leighton, and R. D. James, Energy & Environmental Science **6**, 1315 (2013).

[85] N. Spaldin, *Magnetic Materials: Fundamentals and Applications* (Cambridge University Press, Cambridge CB2 8RU, UK, 2010).

[86] M. De Graef and M. McHenry, *Structure of Materials: An Introduction to Crystallography, Diffraction and Symmetry*, 1st ed. (Cambridge University Press, Cambridge CB2 8RU, UK, 2007).

[87] J. Rodriguez-Carvajal, Physica B: Condensed Matter **192**, 55 (1993).

[88] A. Schwartz, M. Kumar, B. Adams, and D. Field, *Electron Backscatter Diffraction in Materials Science* (Springer US, 233 Spring St, New York, NY 10013, USA, 2010).

[89] W. Zhou and Z. Wang, *Scanning Microscopy for Nanotechnology: Techniques and Applications*, *Springer ebook collection / Chemistry and Materials Science 2005-2008* (Springer New York, 233

Spring St, New York, NY 10013, USA, 2007).

[90] V. Naish and R. Ozerov, *Neutron Diffraction of Magnetic Materials* (Springer US, 233 Spring Street, New York, 10013 N.Y., USA, 2012).

[91] S. Billinge and M. Thorpe, *Local Structure from Diffraction*, *Fundamental Materials Research* (Kluwer Academic Publishers, P.O. Box 17, 3300 AA Dordrecht, the Netherlands, 2012).

[92] E. Kisi and C. Howard, *Applications of Neutron Powder Diffraction*, *Oxford Series on Neutron Scattering in Condensed Matter* (OUP Oxford, Great Clarendon Street, Oxford OX2 6DP, UK, 2012).

[93] R. Ibberson, Nuclear Instruments and Methods in Physics Research Section A: Accelerators, Spectrometers, Detectors and Associated Equipment **600**, 47 (2009).

[94] L. D. Jennings and C. A. Swenson, Physical Review **112**, 31 (1958).

[95] T. Gottschall, Master's thesis, TU Dresden, Fachbereich Physik, 2012.

[96] R. Kiessling, Journal of the Electrochemical Society **98**, 166 (1951).

[97] M. Cadeville and E. Daniel, Journal De Physique **27**, 449 (1966).

[98] E. Dempsey, Philosophical Magazine **8**, 285 (1963).

[99] P. Mohn and D. G. Pettifor, Journal of Physics C: Solid State Physics **21**, 2829 (1988).

[100] T. Shigematsu, T. Kanaizuka, K. Kosuge, M. Shiga, Y. Nakamura, and S. Kachi, Physics Letters A **53**, 385 (1975).

[101] P. K. Liao and K. E. Spear, Bulletin of Alloy Phase Diagrams **7**, 543 (1986).

[102] N. Lundquist and H. P. Myers, Arkiv for Fysik **5**, 463 (1961).

[103] N. Lundquist, H. P. Myers, and R. Westin, Philosophical Magazine **7**, 1187 (1962).

[104] B. Lemius and R. Kuentzler, Journal of Physics F: Metal Physics **10**, 155 (1980).

[105] T. Kanaizuka, Journal of Solid State Chemistry **41**, 195 (1982).

[106] H. Zhu, C. Ni, F. Zhang, Y. Du, and J. Q. Xiao, Journal of Applied Physics **97**, 10M512 (2005).

[107] D. R. Armstrong, P. G. Perkins, and E. A. Cetina V., Theoretica Chimica Acta **64**, 41 (1983).

[108] P. H. Lee, Z. R. Xiao, K. L. Chen, Y. Chen, S. W. Kao, and T. S. Chin, Physica B: Condensed Matter **404**, 1989 (2009).

[109] S. Kervan, Journal of Superconductivity and Novel Magnetism **24**, 815 (2011).

[110] Y. Bourourou, L. Beldi, B. Bentria, A. Gueddouh, and B. Bouhafs, Journal of Magnetism and Magnetic Materials **365**, 23 (2014).

[111] G. Pradelli and C. Gianoglio, Metallurgia Italiana **67**, 21 (1975).

[112] M. C. Cadeville and A. J. P. Meyer, Comptes rendus hebdomadaires des seances de l'Academie des Sciences **255**, 3391 (1962).

[113] T. Kanaizuka, Materials Research Bulletin **16**, 1601 (1981).

[114] R. S. Perkins and P. J. Brown, Journal of Physics F: Metal Physics **4**, 906 (1974).

[115] M. D. Kuz'min, D. Givord, and V. Skumryev, Journal of Applied Physics **107**, 113924 (2010).

[116] D. I. Gorbunov, M. D. Kuz'min, K. Uhlirova, M. Zacek, M. Richter, Y. Skourski, and A. V. Andreev, Journal of Alloys and Compounds **519**, 47 (2012).

[117] K. H. J. Buschow, in *Boron and Refractory Borides*, edited by V. Matkovich (Springer Berlin Heidelberg, ADDRESS, 1977), book section 26, pp. 494–515.

[118] A. Fujita, H. Yako, and M. Kano, Journal of Applied Physics **113**, 17A924 (2013).

[119] A. Barcza, Z. Gercsi, K. S. Knight, and K. G. Sandeman, Physical Review Letters **104**, 4 (2010).

[120] T. Mazet, H. Ihou-Mouko, and B. Malaman, Applied Physics Letters **89**, 022503 (2006).

[121] H. Niu, X.-Q. Chen, W. Ren, Q. Zhu, A. R. Oganov, D. Li, and Y. Li, Physical Chemistry Chemical Physics **16**, 15866 (2014).

[122] E. Parthe, Acta Crystallographica Section B **32**, 2813 (1976).

[123] R. Fruchart, Annales de chimie - Science des materiaux **4**, 1247 (1959).

[124] V. A. Barinov, G. A. Dorofeev, L. V. Ovechkin, E. P. Elsukov, and A. E. Ermakov, physica status solidi (a) **123**, 527 (1991).

[125] H. Okamoto, Journal of Phase Equilibria **14**, 121 (1993).

[126] P. R. I. Smid and F. Weitzer, Proceedings of the 12th International Plansee Seminar **2**, 277 (1989).

[127] F. Yin, T. Shigematsu, N. Gu, and N. Nakanishi, Nanostructured Materials **7**, 629 (1996).

[128] G. Bednarz, D. J. W. Geldart, and M. A. White, Physical Review B **47**, 14247 (1993).

[129] B. K. Banerjee, Physics Letters **12**, 16 (1964).

[130] M. Parra-Borderias, F. Bartolome, J. Herrero-Albillos, and L. M. Garcia, Journal of Alloys and Compounds **481**, 48 (2009).

[131] M. Bratko, E. Lovell, A. D. Caplin, V. Basso, A. Barcza, M. Katter, and L. F. Cohen, Physical Review B **95**, 064411 (2017).

[132] Z. Gercsi and K. G. Sandeman, Physical Review B **81**, 224426 (2010).

[133] Z. Gercsi, K. Hono, and K. G. Sandeman, Physical Review B **83**, 6 (2011).

[134] H. Wada and M. Shiga, Journal of Magnetism and Magnetic Materials **104-107**, 1925 (1992).

[135] T. Kanomata, Y. Ise, N. Kumagai, A. Haga, K. Kamishima, T. Goto, H. M. Kimura, H. Yoshida, T. Kaneko, and A. Inoue, Journal of Alloys and Compounds **259**, L1 (1997).

[136] H. Kadomatsu, F. Ishii, and H. Fujiwara, Journal of the Physical Society of Japan **47**, 1078 (1979).

[137] H. Kadomatsu, M. Isoda, F. Ishii, and H. Fujiwara, Journal of the Physical Society of Japan **48**, 1385 (1980).

[138] H. Yoshida, T. Kaneko, K. Shirakawa, and T. Masumoto, Science reports of the Research Institutes, Tohoku University. Ser. A, Physics, chemistry and metallurgy **33**, 36 (1986).

[139] M. D. Kuz'min, K. P. Skokov, H. Jian, I. Radulov, and O. Gutfleisch, Journal of Physics: Condensed Matter **26**, 064205 (2014).

[140] H. Jian, K. P. Skokov, M. D. Kuz'min, I. Radulov, and O. Gutfleisch, IEEE Transactions on Magnetics **50**, 1 (2014).

[141] D. Markus, K. Soo Kyung, P. S. Michael, A. Daniel, and X. B. Lorin, Journal of Physics: Condensed Matter **27**, 266002 (2015).

[142] A. Edström *et* al., Physical Review B **92**, 174413 (2015).

[143] A. A. Vernekar, S. Patil, C. Bhat, and S. G. Tilve, RSC Advances **3**, 13243 (2013).

[144] D. Bravo-Barcenas, I. Campos-Silva, H. Cimenoglu, J. Martinez-Trinidad, M. Flores-Jimenez, and H. Martinez-Gutierrez, Surface Engineering **32**, 570 (2016).

[145] R. Fruchart, Comptes Rendus Hebdomadaires Des Seances De L Academie Des Sciences **256**, 3304 (1963).

[146] T. Shinohara and H. Watanabe, Journal of the Physical Society of Japan **20**, 2020 (1965).

[147] A. Iga, Journal of the Physical Society of Japan **21**, 1464 (1966).

[148] M. Kasaya, T. Hihara, and Y. Koi, Journal of the Physical Society of Japan **34**, 63 (1973).

[149] B. Lemius and R. Kuentzler, Solid State Communications **16**, 639 (1975).

[150] C. Bormio-Nunes, C. A. Nunes, A. A. Coelho, M. I. S. T. Faria, P. A. Suzuki, and G. C. Coelho, Journal of Alloys and Compounds **508**, 5 (2010).

[151] J. V. Leitão, M. van der Haar, A. Lefering, and E. Brück, Journal of Magnetism and Magnetic Materials **344**, 49 (2013).

[152] L. Caron, M. Hudl, V. Höglin, N. H. Dung, C. P. Gomez, M. Sahlberg, E. Brück, Y. Andersson, and P. Nordblad, Physical Review B **88**, 094440 (2013).

[153] S. V. Vonsovsky, Sov. Phys. Journal of Experimental and Theoritical Physics **8**, 1104 (1938).

[154] L. W. Kirensky and N. S. Akulov, Journal of Physics **3**, 31 (1940).

[155] A. S. Andreenko, P. B. Konstantin, S. A. Nikitin, and M. T. Aleksandr, Soviet Physics Uspekhi **32**, 649 (1989).

[156] K. P. Skokov, Y. G. Pastushenkov, S. A. Nikitin, M. Fries, and O. Gutfleisch, IEEE Transactions on Magnetics **52**, 1 (2016).

[157] L. H. Bennett, R. D. McMichael, R. D. Shull, L. J. Swartzendruber, and R. E. Watson, Journal of Applied Physics **73**, 6507 (1993).

[158] M. Zou, Y. Mudryk, V. K. Pecharsky, K. A. Gschneidner, D. L. Schlagel, and T. A. Lograsso, Physical Review B **75**, 024418 (2007).

[159] X. X. Zhang, H. L. Wei, Z. Q. Zhang, and L. Zhang, Physical Review Letters **87**, 157203 (2001).

[160] S. A. Nikitin, K. P. Skokov, Y. S. Koshkid'ko, Y. G. Pastushenkov, and T. I. Ivanova, Physical Review Letters **105**, 137205 (2010).

[161] J.-L. Jin, X.-Q. Zhang, G.-K. Li, Z.-H. Cheng, L. Zheng, and Y. Lu, Physical Review B **83**, 184431 (2011).

[162] P. K. Das, A. Bhattacharyya, R. Kulkarni, S. K. Dhar, and A. Thamizhavel, Physical Review B **89**, 134418 (2014).

[163] M. Balli, S. Jandl, P. Fournier, and M. M. Gospodinov, Applied Physics Letters **104**, 232402 (2014).

[164] H. Zhang, Y. Li, E. Liu, Y. Ke, J. Jin, Y. Long, and B. Shen, Scientific Reports **5**, 11929 (2015).

[165] Y. Hu, Q. B. Hu, C. C. Wang, Q. Q. Cao, W. L. Gao, D. H. Wang, and Y. W. Du, Solid State Communications **250**, 45 (2017).

[166] E. R. Callen, Journal of Applied Physics **31**, S149 (1960).

[167] E. R. Callen and H. B. Callen, Journal of Physics and Chemistry of Solids **16**, 310 (1960).

[168] B. Monfared, R. Furberg, and B. Palm, International Journal of Refrigeration **42**, 69 (2014).

[169] K. Shirakawa, T. Kaneko, and T. Masumoto, Journal of Magnetism and Magnetic Materials **44**, 342 (1984).

[170] P. K. Liao and K. E. Spear, Bulletin of Alloy Phase Diagrams **9**, 452 (1988).

[171] H. Tange, T. Tokunaga, and M. Goto, Journal of the Physical Society of Japan **45**, 105 (1978).

[172] J. S. Kouvel, Journal of Physics and Chemistry of Solids **16**, 107 (1960).

[173] M. J. Besnus, A. Herr, K. L. Dang, P. Veillet, A. S. Schaafsma, I. Vincze, F. v. d. Woude, F. Mezei, and G. H. M. Calis, Journal of Physics F: Metal Physics **12**, 2393 (1982).

[174] O. Beckman, L. Lundgren, P. Nordblad, P. Svedlindh, A. Törne, Y. Andersson, and S. Rundqvist, Physica Scripta **25**, 679 (1982).

[175] H. Fujii, T. Hokabe, T. Kamigaichi, and T. Okamoto, Journal of the Physical Society of Japan **43**, 41 (1977).

[176] N. H. Dung, Z. Q. Ou, L. Caron, L. Zhang, D. T. C. Thanh, G. A. de Wijs, R. A. de Groot, K. H. J. Buschow, and E. Brück, Advanced Energy Materials **1**, 1215 (2011).

[177] A. Yan, K. H. Muller, L. Schultz, and O. Gutfleisch, Journal of Applied Physics **99**, 08K903 (2006).

[178] N. H. Dung, L. Zhang, Z. Q. Ou, L. Zhao, L. van Eijck, A. M. Mulders, M. Avdeev, E. Suard, N. H. van Dijk, and E. Brück, Physical Review B **86**, 045134 (2012).

[179] Z. Q. Ou, L. Zhang, N. H. Dung, L. van Eijck, A. M. Mulders, M. Avdeev, N. H. van Dijk, and E. Brück, Journal of Magnetism and Magnetic Materials **340**, 80 (2013).

[180] H. Yibole, F. Guillou, L. Zhang, N. H. v. Dijk, and E. Brück, Journal of Physics D: Applied Physics **47**, 075002 (2014).

[181] F. Guillou, H. Yibole, N. H. van Dijk, L. Zhang, V. Hardy, and E. Brück, Journal of Alloys and Compounds **617**, 569 (2014).

[182] F. Guillou, H. Yibole, G. Porcari, L. Zhang, N. H. van Dijk, and E. Brück, Journal of Applied Physics **116**, 063903 (2014).

[183] N. V. Thang, X. F. Miao, N. H. van Dijk, and E. Brück, Journal of Alloys and Compounds **670**, 123 (2016).

[184] R. Gauß, G. Homm, and O. Gutfleisch, Journal of Industrial Ecology in press (2016).

[185] T. Gottschall, K. P. Skokov, F. Scheibel, M. Acet, M. G. Zavareh, Y. Skourski, J. Wosnitza, M. Farle, and O. Gutfleisch, Physical Review Applied **5**, 024013 (2016).

[186] M. G. Zavareh, C. S. Mejia, A. K. Nayak, Y. Skourski, J. Wosnitza, C. Felser, and M. Nicklas, Applied Physics Letters **106**, 071904 (2015).

[187] F. Scheibel, T. Gottschall, K. Skokov, O. Gutfleisch, M. Ghorbani-Zavareh, Y. Skourski, J. Wosnitza, O. Cakir, M. Farle, and M. Acet, Journal of Applied Physics **117**, 233902 (2015).

[188] N. H. Dung, L. Zhang, Z. Q. Ou, and E. Brück, Scripta Materialia **67**, 975 (2012).

[189] A. Pasko, A. Bartok, K. Zehani, L. Bessais, F. Mazaleyrat, and M. LoBue, AIP Advances **6**, 056204 (2016).

[190] A. Bartok, M. Kustov, L. F. Cohen, A. Pasko, K. Zehani, L. Bessais, F. Mazaleyrat, and M. LoBue, Journal of Magnetism and Magnetic Materials **400**, 333 (2016).

[191] Y. He, J. J. Jonas, S. Godet, and P. J. Jacques, Metallurgical and Materials Transactions A **37**, 2641 (2006).

[192] L. Malet, M. R. Barnett, P. J. Jacques, and S. Godet, Scripta Materialia **61**, 520 (2009).

[193] M. G. Glavicic, B. B. Bartha, S. K. Jha, and C. J. Szczepanski, Materials Science and Engineering: A **513-514**, 325 (2009).

[194] Y. He, S. Godet, P. J. Jacques, and J. J. Jonas, Acta Materialia **54**, 1323 (2006).

[195] A. Waske, L. Giebeler, B. Weise, A. Funk, M. Hinterstein, M. Herklotz, K. Skokov, S. Faehler, O. Gutfleisch, and J. Eckert, physica status solidi (RRL) - Rapid Research Letters **9**, 136 (2015).

[196] W. B. Cui, X. K. Lv, F. Yang, Y. Yu, R. Skomski, X. G. Zhao, W. Liu, and Z. D. Zhang, Journal of Applied Physics **107**, 09A938 (2010).

[197] E. Brück, O. Tegus, D. T. Cam Thanh, N. T. Trung, and K. H. J. Buschow, International Journal of Refrigeration **31**, 763 (2008).

[198] X. B. Liu, Z. Altounian, D. H. Ryan, M. Yue, Z. Li, D. Liu, and J. Zhang, Journal of Applied Physics **105**, 07A920 (2009).

[199] L. Zhang, O. Moze, K. Prokes, O. Tegus, and E. Brück, Journal of Magnetism and Magnetic Materials **290**, 679 (2005).

[200] V. Hoeglin, J. Cedervall, M. S. Andersson, T. Sarkar, P. Nordblad, and M. Sahlberg, Journal of Magnetism and Magnetic Materials **374**, 455 (2015).

[201] X. F. Miao, L. Caron, Z. Gercsi, A. Daoud-Aladine, N. H. van Dijk, and E. Brück, Applied Physics Letters **107**, 042403 (2015).

[202] F. Guillou, H. Yibole, A. Kamantsev, G. Porcari, J. Cwik, V. Koledov, N. H. v. Dijk, and E. Brück, IEEE Transactions on Magnetics **51**, 1 (2015).

[203] N. H. Dung, L. Zhang, Z. Q. Ou, and E. Brück, Applied Physics Letters **99**, 092511 (2011).

[204] E. Brück, N. T. Trung, Z. Q. Ou, and K. H. J. Buschow, Scripta Materialia **67**, 590 (2012).

[205] B. Kaeswurm, V. Franco, K. P. Skokov, and O. Gutfleisch, Journal of Magnetism and Magnetic Materials **406**, 259 (2016).

[206] X. F. Miao, L. Caron, P. Roy, N. H. Dung, L. Zhang, W. A. Kockelmann, R. A. de Groot, N. H. van Dijk, and E. Brück, Physical Review B **89**, 174429 (2014).

[207] J. C. V. Leitao, Ph.D. thesis, TU Delft, 2013.

[208] V. K. Pecharsky, J. Cui, and D. D. Johnson, Philosophical Transactions of the Royal Society A: Mathematical, Physical and Engineering Sciences **374**, 20150305 (2016).

[209] N. M. Bruno, S. Wang, I. Karaman, and Y. I. Chumlyakov, Scientific Reports **7**, 40434 (2017).

[210] S. Fähler, U. K. Rößler, O. Kastner, J. Eckert, G. Eggeler, H. Emmerich, P. Entel, S. Müller, E. Quandt, and K. Albe, Advanced Engineering Materials **14**, 10 (2012).

[211] J. Lyubina, K. Nenkov, L. Schultz, and O. Gutfleisch, Physical Review Letters **101**, 177203 (2008).

[212] L. Manosa, X. Moya, A. Planes, O. Gutfleisch, J. Lyubina, M. Barrio, J.-L. Tamarit, S. Aksoy, T. Krenke, and M. Acet, Applied Physics Letters **92**, 012515 (2008).

[213] T. Gottschall, D. Benke, M. Fries, A. Taubel, I. A. Radulov, K. P. Skokov, and O. Gutfleisch, Advanced Functional Materials in press (2017).

[214] M. D. Kuz'min, Applied Physics Letters **90**, 251916 (2007).

[215] J. D. Moore *et* al., Journal of Applied Physics **114**, 043907 (2013).

[216] I. A. Radulov, D. Y. Karpenkov, K. P. Skokov, A. Y. Karpenkov, T. Braun, V. Brabänder, T. Gottschall, M. Pabst, B. Stoll, and O. Gutfleisch, Acta Materialia **127**, 389 (2017).

[217] T. Gottschall, K. P. Skokov, R. Burriel, and O. Gutfleisch, Acta Materialia **107**, 1 (2016).

[218] A. Smith, C. R. H. Bahl, R. Bjork, K. Engelbrecht, K. K. Nielsen, and N. Pryds, Advanced Energy Materials **2**, 1288 (2012).

[219] J. Lyubina, Journal of Physics D: Applied Physics **50**, 053002 (2017).

[220] F. Cugini *et* al., Applied Physics Letters **108**, 012407 (2016).

Curriculum Vitae

Personal information

Name	Maximilian Fries
Date of birth	16 May, 1987
Place of birth	Aschaffenburg, Germany

Research interests

Synthesis and characterization of functional magnetic materials

Magnetic energy conversion technologies

Magnetic thin films

Pressure-dependent magnetic phenomena

Green energy technologies

Nanoparticles for biomedical applications

Education

2013 - 2017	Ph. D. student in Material Science Functional Materials Supervisor: Prof. O. Gutfleisch Technische Universität Darmstadt, Germany
2012	Research assistant Advanced Thin Film Technology Technische Universität Darmstadt, Germany
2006 - 2012	Study of Material Science Degree: Diplom Ingenieur Thesis: Sputtered $MoSi_2$ thin films Supervisor: Prof. L. Alff Technische Universität Darmstadt, Germany
2006	Abitur Bachgauschule, Babenhausen, Germany

Conference contributions

INTERMAG 2017, Dublin, Ireland, Oral presentation

MMM 2016, New Orleans, USA, Oral presentation

Thermag 2016, Torino, Italy, Poster presentation

JEMS 2016, Glasgow, UK, Poster presentation

Advances in Magnetism 2016, Bormio, Italy, Oral presentation

DPG-Frühjahrstagung 2016, Regensburg, Germany, Oral presentation

Meeting of the Royal Society 2016 - Taking the temperature of phase transitions in cool materials, London, UK, Poster presentation

Delft Days on magnetocalorics 2015, Delft, Netherlands, Poster presentation

INTERMAG 2015, Beijing, China, Oral presentation

DPG-Frühjahrstagung 2015, Berlin, Germany, Oral presentation

Thermag 2014, Victoria, Canada, Oral presentation

INTERMAG 2014, Dresden, Germany, Oral presentation

DPG-Frühjahrstagung 2014, Dresden, Germany, Oral presentation

List of publications

[1] K. P. Skokov, D. Yu. Karpenkov, M. D. Kuz'min, I. A. Radulov, T. Gottschall, B. Kaeswurm, **M. Fries**, O. Gutfleisch, Heat exchangers made of polymer-bonded La(Fe,Si)$_{13}$ Journal of Applied Physics **115** (2014) 17A941.

[2] A. Tkach, M. Baghaie Yazdi, M. Foerster, F. Büttner, M. Vafaee, **M. Fries**, M. Kläui, Magnetoelectric properties of epitaxial Fe_3O_4 thin films on (011) PMN-PT piezosubstrates, Physical Review B **91** (2015) 024405.

[3] A. Edström, M. Werwinski, D. Iusan, J. Rusz, O. Eriksson, K. P. Skokov, I. A. Radulov, S. Ener, M. D. Kuz̀min, J. Hong, **M. Fries**, D. Yu. Karpenkov, O. Gutfleisch, P. Toson and J. Fidler, Magnetic properties of $(Fe_{1-x}Co_x)_2B$ alloys and the effect of doping by 5d elements, Physical Review B **92** (2015) 174413.

[4] **M. Fries**, Z. Gercsi, S. Ener, K. P. Skokov and O. Gutfleisch, Magnetic and magnetocaloric properties of Mn based borides doped with Iron and Cobalt, Acta Materialia **112** (2014) 11256.

[5] K. P. Skokov, Y. G. Pastushenkov, S. A. Nikitin, **M. Fries**, O. Gutfleisch, Rotational Magnetocaloric Effect in the $Er_2Fe_{14}B$ Single Crystal, IEEE Transactions on Magnetics **52** (2016) 2500304.

[6] O. Gutfleisch, T. Gottschall, **M. Fries**, D. Benke, I. Radulov, K. P. Skokov, H. Wende, M. Gruner, M. Acet, P. Entel and M. Farle, Mastering hysteresis in magnetocaloric materials, Philosophical Transactions A **374** (2016) 20150308.

[7] **M. Fries**, K. P. Skokov, D. Yu. Karpenkov, V. Franco, S. Ener, and O. Gutfleisch, The influence of magnetocrystalline anisotropy on the magnetocaloric effect: A case study on Co_2B, Applied Physics Letters **109** (2016) 232406.

[8] **M. Fries**, L. Pfeuffer, E. Bruder, T. Gottschall, S. Ener, L. V. B. Diop, T. Gröb, K. P. Skokov and O. Gutfleisch, Microstructural and magnetic properties of Mn-Fe-P-Si (Fe_2P-type) magnetocaloric compounds, Acta Materialia **132** (2017) 222.

[9] T. Gottschall, D. Benke, **M. Fries**, A. Taubel, I. A. Radulov, K. P. Skokov and O. Gutfleisch, A matter of size and stress: Understanding the first-order transition of materials for solid-state refrigeration, Advanced Functional Materials **27** (2017) 1606735.